

5-2010

## Developmental Changes in the Structure and Composition of the Postsynaptic Density

Matthew T. Swulius

Follow this and additional works at: [https://digitalcommons.library.tmc.edu/utgsbs\\_dissertations](https://digitalcommons.library.tmc.edu/utgsbs_dissertations)



Part of the [Developmental Neuroscience Commons](#), [Molecular and Cellular Neuroscience Commons](#), and the [Structural Biology Commons](#)

---

### Recommended Citation

Swulius, Matthew T., "Developmental Changes in the Structure and Composition of the Postsynaptic Density" (2010). *The University of Texas MD Anderson Cancer Center UTHealth Graduate School of Biomedical Sciences Dissertations and Theses (Open Access)*. 43.  
[https://digitalcommons.library.tmc.edu/utgsbs\\_dissertations/43](https://digitalcommons.library.tmc.edu/utgsbs_dissertations/43)

This Dissertation (PhD) is brought to you for free and open access by the The University of Texas MD Anderson Cancer Center UTHealth Graduate School of Biomedical Sciences at DigitalCommons@TMC. It has been accepted for inclusion in The University of Texas MD Anderson Cancer Center UTHealth Graduate School of Biomedical Sciences Dissertations and Theses (Open Access) by an authorized administrator of DigitalCommons@TMC. For more information, please contact [digitalcommons@library.tmc.edu](mailto:digitalcommons@library.tmc.edu).

**DEVELOPMENTAL CHANGES IN THE STRUCTURE AND COMPOSITION OF  
THE POSTSYNAPTIC DENSITY**

by

Matthew Thomas Swulius, B.S.

Approved:

---

Supervisory Professor  
M. Neal Waxham, Ph.D.

---

Andrew Bean, Ph. D.

---

Jack Waymire, Ph.D.

---

James K. Stoops, Ph.D.

---

Pawel Penczek, Ph.D.

---

Approved:

---

Dean, The University of Texas  
Health Science Center at Houston  
Graduate School of Biomedical Sciences

**DEVELOPMENTAL CHANGES IN THE STRUCTURE AND COMPOSITION OF  
THE POSTSYNAPTIC DENSITY**

**A  
DISSERTATION**

Presented to the Faculty of  
The University of Texas  
Health Science Center at Houston  
and  
The University of Texas  
M. D. Anderson Cancer Center  
Graduate School of Biomedical Sciences

in Partial Fulfillment  
of the Requirements  
for the Degree of  
**DOCTOR OF PHILOSOPHY**

by  
Matthew T. Swulius, B.S.

May, 2010

© Matthew T. Swulius, 2010

ALL RIGHTS RESERVED



*I dedicate this to my Grandmother,*

*Helen Louise Kraska.*

*Every day I feel you in my*

*Thoughts and actions.*

## Acknowledgments

With no surprise this all started with my parents Tom and Kathi Swulius. My father's lifelong interest in the universe and the forces that govern it is stamped deeply on to my earliest memories. I have come to recognize that his drive to stare outward into the darkness of space, with great curiosity, is the same that has driven me to turn inward. While my father's influence on my scientific pursuit is obvious, it is my mother who gave me the patience required to accept science's lack of pity when nothing seems to be going right. I know it pales in comparison to the patience she showed while raising me and my brothers. My parents have provided me with endless support of every imaginable kind, and needless to say, none of this would be possible without them. With no doubt I will continue turning to them when I need assurance, for they have always been my biggest fans.

In addition to my parents, I was fortunate to have two brothers continuously at my side. I am in debt to my older brother Pete for striving never to steer me in the wrong direction, and to my younger brother Mike for letting me feel like a role-model. I cannot imagine life without them, nor can I fathom where I'd be had they not been a constant force through my development.

Beyond family there has been a long line of people who played critical roles in getting me here. First, there are all of the teachers who dedicated their lives to educating me and so many others. While there is no room here to list them all, I would like to acknowledge Brian Edwards specifically. He was and always will be an inspiration to me. Somehow, in a small Texas town where chemistry might as well have been Greek mythology, he never seemed to lose his enthusiasm, and for this I want to thank him. I want to thank Ying Wu, my first mentor out of college, and the person who first taught me to have "a feeling for the molecule". I want to thank all of the friends I have made during my time in graduate school, Wade Kothmann and

Aaron Carmen specifically. I am relying on them for many lucrative collaborations in the future.

I want to thank everyone on my supervisory committee, who have become friends and colleagues over the years. They provided continuous input on my project throughout my time here and undoubtedly made my work infinitely better than it would have been otherwise.

I want to thank my lab members, past and present (Andrea Quintana, Amelie Forest, Hugo Sanabria and Yoshi Kubota), for years of great scientific conversation as well as great friendship. I'd also like to thank Melissa Bryant and Madeline Burgoyne (the two newest members) for giving me the chance to pass on some of what I've learned over the years. It is reassuring to know the things I started will be left in such capable hands.

Lastly, I want to thank my advisor, my colleague and my friend Neal Waxham. I think he knows my feelings about the support he has given me, and words could only act as a barrier at this point. My only hope is that my actions from here on will make him proud. In short, I owe him everything. I know that without him I'd still be wandering aimlessly. I know that there is still much to learn from him, and I'm comforted to know this is not the end of our time spent working together. He has been the ideal advisor, and should I have the chance to run my own lab I will always strive to be for my students what he has been for me.

# **DEVELOPMENTAL CHANGES IN THE STRUCTURE AND COMPOSITION OF THE POSTSYNAPTIC DENSITY**

Publication No. \_\_\_\_\_

Matthew T. Swulius, Ph.D.

Supervisory Professor: M. Neal Waxham, Ph.D.

## **Abstract**

The development of the brain and its underlying circuitry is dependent on the formation of trillions of chemical synapses, which are highly specialized contacts that regulate the flow of information from one neuron to the next. It is through these synaptic connections that neurons wire together into networks capable of performing specific tasks, and activity-dependent changes in their structural and physiological state is one way that the brain is thought to adapt and store information. At the ultrastructural level, developmental and activity-dependent changes in the size and shape of dendritic spines have been well documented, and it is widely believed that structural changes in spines are a hallmark sign of synapse maturation and alteration of synaptic physiology. While changes in spine structure have been studied extensively, changes in one of its most prominent components, the postsynaptic density (PSD), have largely evaded observation. The PSD is a protein-rich organelle on the cytoplasmic side of the postsynaptic membrane, where it sits in direct opposition to the presynaptic terminal. The PSD functions both to cluster neurotransmitter receptors at the cell surface as well as organize the intracellular signaling molecules responsible for transducing extracellular signals to the postsynaptic cell. Much is known about the chemical composition of the PSD, but the structural arrangement of its molecular components is not well documented. Adding to the difficulty of understanding such a complex mass of protein machinery is the fact that its protein composition is known to change in response to synaptic activity, meaning that its structure is plastic and no

two PSDs are identical. Here, immuno-gold labeling and electron tomography of PSDs isolated throughout development was used to track changes in both the structure and molecular composition of the PSD. State-of-the-art cryo-electron tomography was used to study the fine structure of the PSD during development, and provides an unprecedented glimpse into its molecular architecture in an un-fixed, unstained and hydrated state. Through this analysis, large structural and compositional changes are apparent and suggest a model by which the PSD is first assembled as a mesh-like lattice of proteins that function as support for the later recruitment of various PSD components. Spatial analysis of the recruitment of proteins into the PSD demonstrated that its assembly has an underlying order.

## Table of Contents

<b>Abstract .....</b>	<b>vii</b>
<b>Table of Contents .....</b>	<b>ix</b>
<b>List of Figures .....</b>	<b>xii</b>
<b>List of Tables .....</b>	<b>xv</b>
<b>Background and Significance .....</b>	<b>1</b>
<b>A Brief History of the Synapse.....</b>	<b>1</b>
<b>Types of Synapses.....</b>	<b>3</b>
<b>Chemical Transmission.....</b>	<b>5</b>
<b>Synaptic Architecture .....</b>	<b>6</b>
<b>The Postsynaptic Density .....</b>	<b>8</b>
<b>Synapses, Learning and the Development of Neural Circuitry .....</b>	<b>10</b>
<b>Synaptic Plasticity .....</b>	<b>12</b>
<b>Ca<sup>2+</sup> / Calmodulin-Dependent Kinase II (CaMKII).....</b>	<b>14</b>
<b>CaMKII in the PSD.....</b>	<b>15</b>
<b>Assembly of the PSD .....</b>	<b>17</b>
<b>Methods .....</b>	<b>19</b>
<i>Isolation of Postsynaptic Densities .....</i>	<i>19</i>
<i>Antibody Characterization .....</i>	<i>20</i>
<i>Immunolabeling of Postsynaptic Densities and Electron Microscopy.....</i>	<i>20</i>
<i>Electron Tomography and Image processing .....</i>	<i>21</i>
<i>Cryo-Electron Microscopy .....</i>	<i>21</i>
<i>Western Blotting .....</i>	<i>22</i>
<i>Point Pattern Analysis of Gold Particle Distribution .....</i>	<i>23</i>
<b>Results .....</b>	<b>26</b>

<b><u>Chapter 1: Isolation of Adult PSDs and their Morphological/Biochemical Characteristics</u></b>	<b>26</b>
Isolation of PSDs .....	26
General Morphology in EM.....	28
A subset of proteins are enriched during the isolation process .....	33
Enrichment of Proteins in the PSD Fraction .....	35
<b><u>Chapter 2: PSDs Isolated at Different Developmental Time Points.....</u></b>	<b>40</b>
Protein Profiles of PSDs Isolated from Rat Forebrain at P60, P21, P2 and E19.....	41
Structure of PSDs during Development of Rat Brain .....	43
Size Comparison of PSDs Isolated from Forebrain at E19, P2, P21 and P60.....	57
Protein composition of PSDs isolated at E19, P2, P21 and P60.....	60
Spatial Analysis of Immuno-Gold Labeling.....	70
<b><u>Chapter 3: Structure of Cryo-preserved PSDs during development .....</u></b>	<b>78</b>
PSDs isolated from adult rats are characterized by layers of distinct protein. ....	79
The PSD-mesh and dense layer are variable in nature and contain a complex mixture of protein components/morphologies .....	85
Detergent resistant membrane remains attached to isolated PSDs .....	93
PSDs isolated at P21 share the same morphological features of those isolated at P60 .....	96
PSDs isolated at P2 and E19 are composed almost entirely of PSD-mesh .....	102
<b>Discussion .....</b>	<b>109</b>
Why isolate PSDs?.....	109
Tomography of negatively stained PSDs.....	111
Compositional changes during development observed by immuno-gold labeling. ....	113
Spatial distribution of immuno-gold labeling.....	117

<b>Cryo-tomography of isolated PSDs .....</b>	<b>118</b>
<b>PSD Assembly .....</b>	<b>122</b>
<b>Summary and Future Direction.....</b>	<b>123</b>
<b>Appendix: Spatial Analysis of Gold Label Distributions .....</b>	<b>129</b>
<b>Pseudo three-dimensional simulation of random distributions .....</b>	<b>131</b>
<b>Nearest Neighbor Analysis .....</b>	<b>135</b>
<b>Pair Correlation Function Analysis.....</b>	<b>138</b>
<b>Ripley's K Function Analysis .....</b>	<b>144</b>
<b>References .....</b>	<b>150</b>
<b>Vita .....</b>	<b>169</b>



## List of Figures

Fig. 1 <i>Electron micrograph of a typical synapse</i> .....	2
Fig. 2 <i>Diagram of events underlying chemical synaptic transmission</i> .....	7
Fig. 3 <i>Postsynaptic densities in thin sectioned neuronal tissue</i> .....	9
Fig. 4 <i>Structure of CaMKII holoenzyme and diagram of its regulation</i> .....	16
Fig. 1.1 <i>Schematic of PSD Isolation and Characterization of Isolated PSDs</i> .....	27
Fig. 1.2 <i>Low magnification electron micrograph of isolated PSDs</i> .....	30
Fig. 1.3 <i>High magnification views of individual isolated PSDs</i> .....	32
Fig. 1.4 <i>Protein profiles of fractions during PSD isolation and enrichment of Pre- and Postsynaptic proteins</i> .....	34
Fig. 1.5 <i>Enrichment of proteins through PSD isolation process and specificity of antibodies</i> ..	37
Fig. 2.1 <i>Comparison of Protein Profiles of PSDs Isolated at E19, P2, P21 and P60</i> .....	42
Fig. 2.2 <i>Tomographic reconstruction of a PSD isolated at E19</i> .....	46
Fig. 2.3 <i>Tomographic reconstruction of a PSD isolated at E19</i> .....	47
Fig. 2.4 <i>Tomographic reconstruction of a PSD isolated at E19</i> .....	48
Fig. 2.5 <i>Tomographic Reconstruction of PSD isolated at P2</i> .....	50
Fig. 2.6 <i>Tomographic Reconstruction of PSD isolated at P2</i> .....	51
Fig. 2.7 <i>Tomographic Reconstruction of PSD isolated at P2</i> .....	52
Fig. 2.8 <i>Tomographic Reconstruction of PSD isolated at P21</i> .....	53
Fig. 2.9 <i>Tomographic Reconstruction of PSD isolated at P21</i> .....	55
Fig. 2.10 <i>Tomographic Reconstruction of PSD isolated at P21</i> .....	56
Fig. 2.11 <i>Tomographic Reconstructions of PSDs isolated at P60</i> . ....	58
Fig. 2.12 <i>Histograms of PSD surface area at E19, P2, P21 and P60</i> . ....	59
Fig. 2.13 <i>Immunogold labeling of PSD-95 and Actinin at E19, P2, P21 and P60</i> .....	64
Fig. 2.14 <i>Immunogold labeling of NR1, NR2b and GluR1 at E19, P2, P21 and P60</i> .....	67

Fig. 2.15 Immunogold labeling of $\alpha$ CaMKII, $\beta$ CaMKII and CaM at E19, P2, P21 and .....	69
Fig. 2.16 Immunogold labeling controls.....	71
Fig. 2.17 The convex hull as a boundary for spatial analysis .....	73
Fig. 2.18 The convex hull as a boundary for spatial analysis .....	74
Fig. 2.19 RKF plot showing clustering.....	75
Fig. 3.1 Cryo-preserved PSDs isolated at P60.....	81
Fig. 3.2 PSD-mesh observed in cryo-preserved P60 PSD.....	83
Fig. 3.3 Mid-level cross-section observed in cryo-preserved P60 PSD.....	87
Fig. 3.4 Continuous dense layer observed in cryo-preserved P60 PSD.....	88
Fig. 3.5 Non-continuous dense layer observed in cryo-preserved P60 PSD.....	89
Fig. 3.6 Illustration of protein rings in the dense layer of P60 PSDs. ....	91
Fig. 3.7 Montage of protein rings of various size and shape. ....	92
Fig. 3.8 Montage of PSD components with membrane still attached.....	94
Fig. 3.9 Protein ring with membrane attached continuously around the perimeter. ....	95
Fig. 3.10 Cryo-preserved PSDs isolated at P21.....	97
Fig. 3.11 PSD-mesh observed in cryo-preserved P21 PSD.....	98
Fig. 3.12 Dense protein observed in cryo-preserved P21 PSD.....	100
Fig. 3.13 Granular network of isolated PSD.....	101
Fig. 3.14 Cryo-preserved PSDs isolated at P2.....	103
Fig. 3.15 Fine morphology of PSD isolated at P2.....	105
Fig. 3.16 Cryo-preserved PSDs isolated at E19.....	106
Fig. 3.17 Fine morphology of a PSD isolated at E19.....	108
Fig. A.1 Illustration of the pseudo-3D simulation of randomly distributed gold particles.....	133
Fig. A.2 Principles of particle placement in the pseudo-3D simulations.....	134
Fig. A.3 Nearest Neighbor Analysis can be Blind to the Global Distribution of Particles.....	137

Fig. A.4 <i>Principle of PCF Analysis</i> .....	142
Fig. A.5 <i>Test for clustering by pair correlation function.</i> .....	143
Fig. A.6 <i>Illustration of the principles of RKF analysis.</i> .....	147

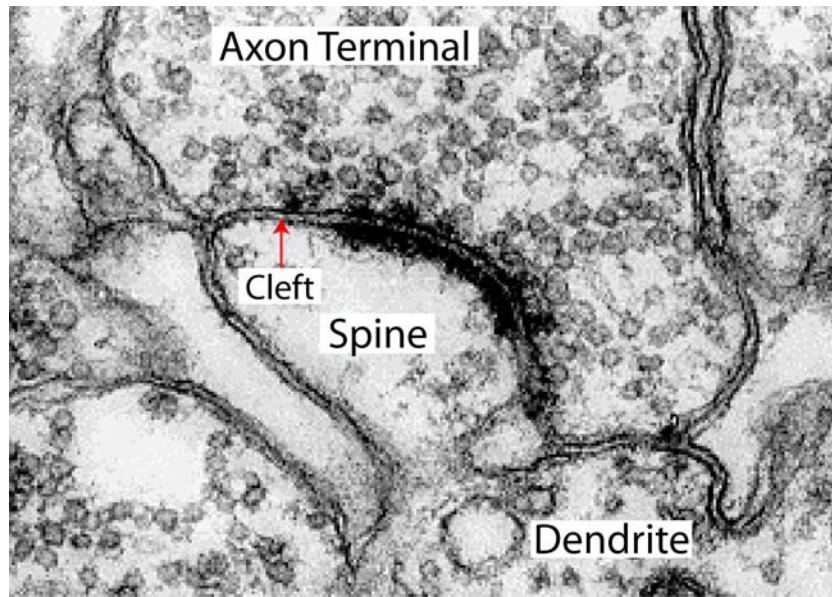
## List of Tables

Table 2.1 <i>Summary of immuno-gold labeling results</i> .....	62
Table 2.2 <i>Number of individual PSDs that showed immuno-gold labeling above background.</i>	63
Table 2.3 <i>Number of individual PSDs that showed clustering by RKF analysis for each antibody and developmental time point.</i> .....	76
Table A.1 <i>Nearest Neighbor test for non-randomness using the Kolomogorov-Smirnov test for significance (<math>P &lt; 0.05</math>)</i> .....	139
Table A.2 <i>Mean Nearest Neighbor distances (nm).</i> .....	140
Table A.3 <i>Peak Nearest Neighbor distances (nm).</i> .....	141
Table A.4 <i>PCF test for non-randomness using the Kolomogorov-Smirnov test for significance (<math>P &lt; 0.05</math>).</i> .....	145
Table A.5 <i>Number of individual PSDs that showed clustering by RKF analysis.</i> .....	148

## **Background and Significance**

### **A Brief History of the Synapse**

The use of the word “Synapse” to describe points of contact between neurons was coined by Charles Sherrington near the turn of the twentieth century (Foster, 1897), but the concept of such a connection dates back another fifty years or so and was at the heart of a great debate, driven by two opposing theories. The neuron theorists believed that neurons were individual cells within the nervous system, while the reticular theorists posited that connections between neurons were points of protoplasmic continuity through which electrical impulses freely passed from one neural entity to the next. Despite the general acceptance of the cellular theory in all other types of tissue, it was surprising to find such polarized opinions about the cellular basis of the nervous system. It wasn’t until the mid-twentieth century and the development of electron microscopy that adequate detail was obtained to directly visualize the points of contact between neurons (Gray, 1959a; b; Palay, 1956; Palay and Palade, 1955). By fixing and embedding samples of neural tissue in resin, thin sections could be cut with a glass knife and the underlying cellular architecture revealed by counterstaining with heavy metal to increase contrast. In electron micrographs of cross sections through synaptic connections a cell membrane was clearly visible on both sides of the contact point, with an obvious space (the synaptic cleft) between the membranes of the two connecting cells. Fig. 1 is an electron micrograph of a thin section cut perpendicular to the synaptic membrane. The presynaptic component, the axon terminal, is seen adjacent to the postsynaptic spine, but there is a clear gap between the two compartments pointed out by the red arrow. With this high-detail electron microscopic data available, the remaining reticular theorists were forced to accept that individual neurons were separate entities, fully enclosed within a lipid bi-layer just as all cells are. After this discovery, electron microscopy became an invaluable tool in visually dissecting the ultrastructural arrangement of the synapse. It was categorized into two main components,



**Fig. 1** *Electron micrograph of a typical synapse.* Adapted with permission from: Synapse Web, Kristen M. Harris, PI. Image contribution by Josef Spacek.

the pre- and postsynaptic compartments, and the structure/function of these compartments has been heavily researched ever since.

### **Types of Synapses**

Synapses are most broadly categorized as chemical and electric. While this thesis focuses only on chemical synapses it is important not to forget that electrical synapses exist and can play a large role in regulating the flow of current through neuronal networks. The retina is a prime example of this organization, as groups of cells can be coupled and decoupled via electrical synapses. Electric synapses are called so because they allow the passive transfer of electrical charge from one neuron to the next through ion channels that span both membranes of neighboring cells. These ion channels are formed by the joining of two connexin complexes—each one spanning the membrane of each cell—and clustered into lateral arrays known as gap junctions (Sosinsky and Nicholson, 2005). One advantage of direct electrical coupling is that the transfer of charge is instantaneous due to cytoplasmic continuity between adjoined cells. In a sense, the concept of cytoplasmic continuity revered by the reticularists is realized at electrical synapses. However, the pores formed by connexin proteins at these gap junctions only allow the free diffusion of ions and small molecules ( $< 1$  kDa), so it is not complete cytoplasmic sharing. At electrical synapses the flow of ion current through the pores is bi-directionally equal, meaning that electrical charge is free to move in either direction through the synapse depending on in which neuron the charge originates.

Unlike electrical synapses, chemical synapses transmit information between neurons via the release of a chemical substance, known as neurotransmitter, from one cell, and the subsequent detection of this chemical by the next cell through neurotransmitter receptors displayed on the cell surface. Chemical synapses make up the majority of synapses in the brain and are generally categorized by the neurotransmitter that they secrete. Glutamatergic synapses release glutamate, glycinergic synapses release glycine and serotonergic synapses release

serotonin. There are of course many more neurotransmitters, and thus many more types of chemical synapses. Depending on the type of neurotransmitter and the location of the synapse in the brain, chemical synapses can further be classified as participating in fast chemical transmission through chemically gated ion channels or slower modulatory transmission via G-coupled protein receptors that elicit longer acting changes in neuronal properties.

Chemical synapses involved in fast chemical transmission are distinguished into two groups known as excitatory or inhibitory. Excitatory synapses typically release glutamate, which opens cation permeable channels in the post synaptic neuron. This influx of cations (typically sodium or calcium) depolarizes the postsynaptic membrane and drives the postsynaptic neuron toward firing an action potential. The term excitatory comes from the fact that activation of these synapses increases the probability of the postsynaptic neuron firing by “exciting” it. Inhibitory synapses in the brain typically release gamma-aminobutyric acid (GABA), which opens receptor channels permeable to the anion chloride. In the opposite fashion of the excitatory synapse, negatively charged chloride ions flow into the postsynaptic neuron and decrease its probability of firing by hyperpolarizing the cell membrane. In a simplified sense, neuronal circuits connected via excitatory synapses can be thought of as the core wiring of the nervous system as they are involved in the flow of electrical information from one cell to another. Inhibitory connections play an equally important role in circuit function by determining whether a given neuron in a circuit will propagate the action potential or not. Globally, the rate of a neuron’s firing is determined by the sum of both its excitatory and inhibitory inputs.

Modulatory synaptic transmission is classically carried out by synapses that release neurotransmitters such as serotonin, dopamine and norepinephrine to name a few. Instead of directly affecting the flow of ions across the postsynaptic membrane, like excitatory and inhibitory transmitters, these modulatory neurotransmitters usually act on G-protein coupled



receptors that induce metabolic changes in the target neuron with much slower, but longer lasting kinetics. Modulatory synapses do play an important role in modifying the flow of current through neuronal circuits by changing the intrinsic excitability of neurons.

One reason for using chemical synapses as the primary synaptic type is that it allows for directionality in the flow of current from one cell to the next. As mentioned above, the flow of current through electrical synapses is passive and can move freely in either direction. Because of the architectural arrangement of the chemical synapse there is an inherent directionality to the flow of information. Generally speaking, the presynaptic side is designed to release chemical messengers and the postsynaptic side is built to recognize and respond to this signal, thus allowing this process to only occur in one direction. It is true that retrograde messengers exist that can diffuse from the postsynaptic side back to the presynaptic side, but they normally function to modulate the presynaptic terminal's ability to release transmitter as opposed to causing the presynaptic cell to fire. It is through the controlled directional flow of information that the brain is capable of building organized networks of cells that function to process information properly.

Another important reason for using chemical synapses is that they provide the ability to control the sign of the signal being sent by the presynaptic neuron. For example, when an inhibitory neuron becomes excited and fires an action potential, the effect of its chemical release is to inhibit its postsynaptic counterpart, thus blocking further propagation of the electrical current. This provides much greater control over the types of circuitry that can be assembled in the nervous system.

### **Chemical Transmission**

As mentioned above, communication between neurons is primarily mediated via fast chemical transmission at synapses. This occurs when an action potential traveling down the axon invades the presynaptic nerve terminal and activates voltage-dependent  $\text{Ca}^{2+}$  channels

embedded in the plasma membrane. The influx of  $\text{Ca}^{2+}$  ions through these channels triggers the exocytosis of transmitter-filled vesicles at active zones located along the presynaptic membrane and the subsequent release of neurotransmitter into the synaptic cleft. Neurotransmitter receptors located in the postsynaptic membrane detect the presence of neurotransmitter via binding, and their activation leads to the opening of ion channels that conduct a depolarizing current (if they are excitatory) into the postsynaptic cell. Fig. 2 diagrams these events.

### **Synaptic Architecture**

The pre- and postsynaptic compartments are both distinguishable by unique morphological characteristics so they are easily identified in electron micrographs. The presynaptic terminal is most easily recognized by the appearance of synaptic vesicles, which contain neurotransmitter. These vesicles are generally clustered near the active zone of the presynaptic terminal, which is the portion of the presynaptic membrane where vesicle exocytosis occurs. The active zone is characterized by the presence of protein clusters that represent the machinery involved in the docking and fusion of neurotransmitter vesicles.

The postsynaptic element of most excitatory synapses in the central nervous system is known as the dendritic spine, a small protrusion from the dendritic shaft of neurons. Dendritic spines are considered to be the fundamental computational units of the neuron as current through thousands of spines on a single cell are integrated to determine if it will fire or not. The dendritic spine is shaped primarily by an extensive actin cytoskeleton, which is highly dynamic (Korobova and Svitkina, 2010; Sekino et al., 2007; Tataavarty et al., 2009). This dynamic cytoskeleton is thought to underlie the spine's ability to undergo activity-dependent changes in size and shape, which are hypothesized to generate changes in synaptic physiology. In tune with the size and shape of the dendritic spine is its most prominent ultrastructural feature, the postsynaptic density (PSD); a large protein complex that sits along the plasmalemmal side of the postsynaptic membrane responsible for organizing neurotransmitter receptors and

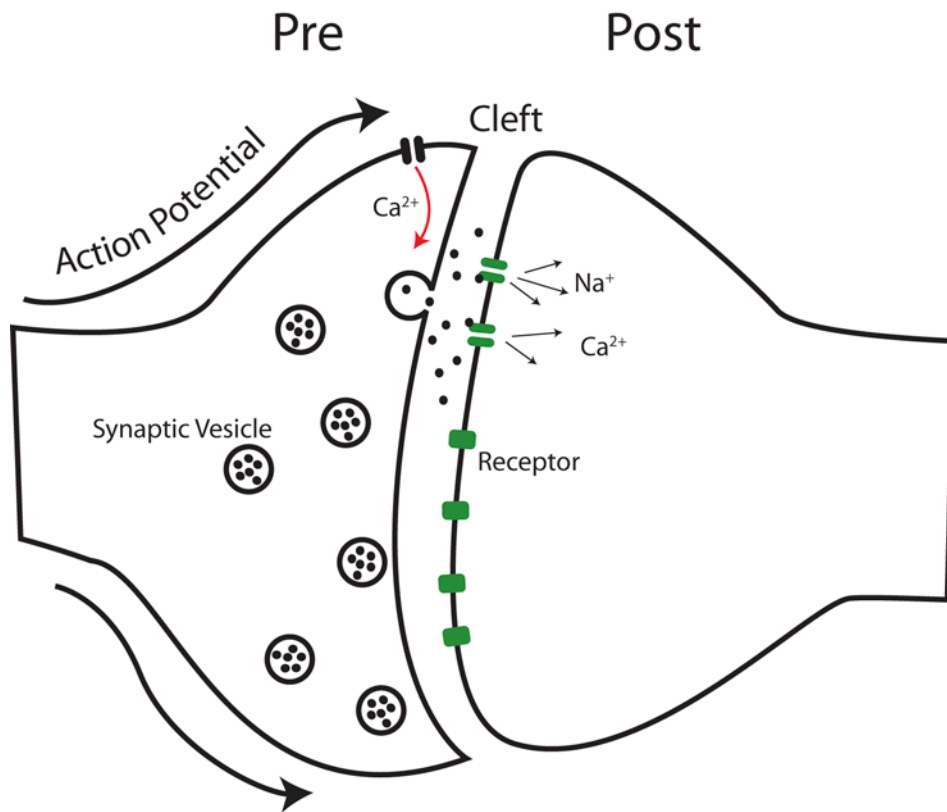


**Fig. 2** *Diagram of events underlying chemical synaptic transmission.*

intracellular signaling molecules. The function of the PSD, which is the central focus of this thesis, is described in more detail below.

### **The Postsynaptic Density**

At the ultrastructural level excitatory synapses in the central nervous system are characterized by an asymmetric appearance in protein density associated with the postsynaptic compartment (Fig. 3). This density was aptly named the postsynaptic density (PSD) by early electron microscopists studying synaptic architecture (Gray, 1959b; Palay, 1958), and due to its location along the cytoplasmic face of the postsynaptic membrane it was thought to be attributable to the clustering of neurotransmitter receptors beneath the presynaptic terminal. This made sense and it is true that neurotransmitter receptors do reside within the PSD, but modern biochemical and proteomic analyses have revealed a protein composition indicative of something much more complex (Dosemeci et al., 2007; Dosemeci et al., 2006; Jordan et al., 2004; Li et al., 2004; Peng et al., 2004; Walikonis et al., 2000; Yoshimura et al., 2004). In addition to receptors there is a variety of scaffolding and cell adhesion molecules as well as many signaling proteins known to be involved in regulating multiple aspects of synaptic function such as plasticity. Knowing this speaks volumes about the PSD's functionality within the spine and allows for a more comprehensive awareness of its role as an organized protein-machine capable of receiving signals and processing information.

Due of their small size (~500 nm in diameter and ~40 nm thick) PSDs are very difficult to study in a cellular context, so one of the most important accomplishments in PSD research has been the development of protocols for obtaining sub-cellular fractions highly enriched in these organelles. Two labs pioneered this task in the 1970's and demonstrated the ability to isolate PSDs from synaptosomal preps using a series of detergent extraction and differential centrifugation steps (Cohen et al., 1977; Cotman et al., 1974). Although these original methods

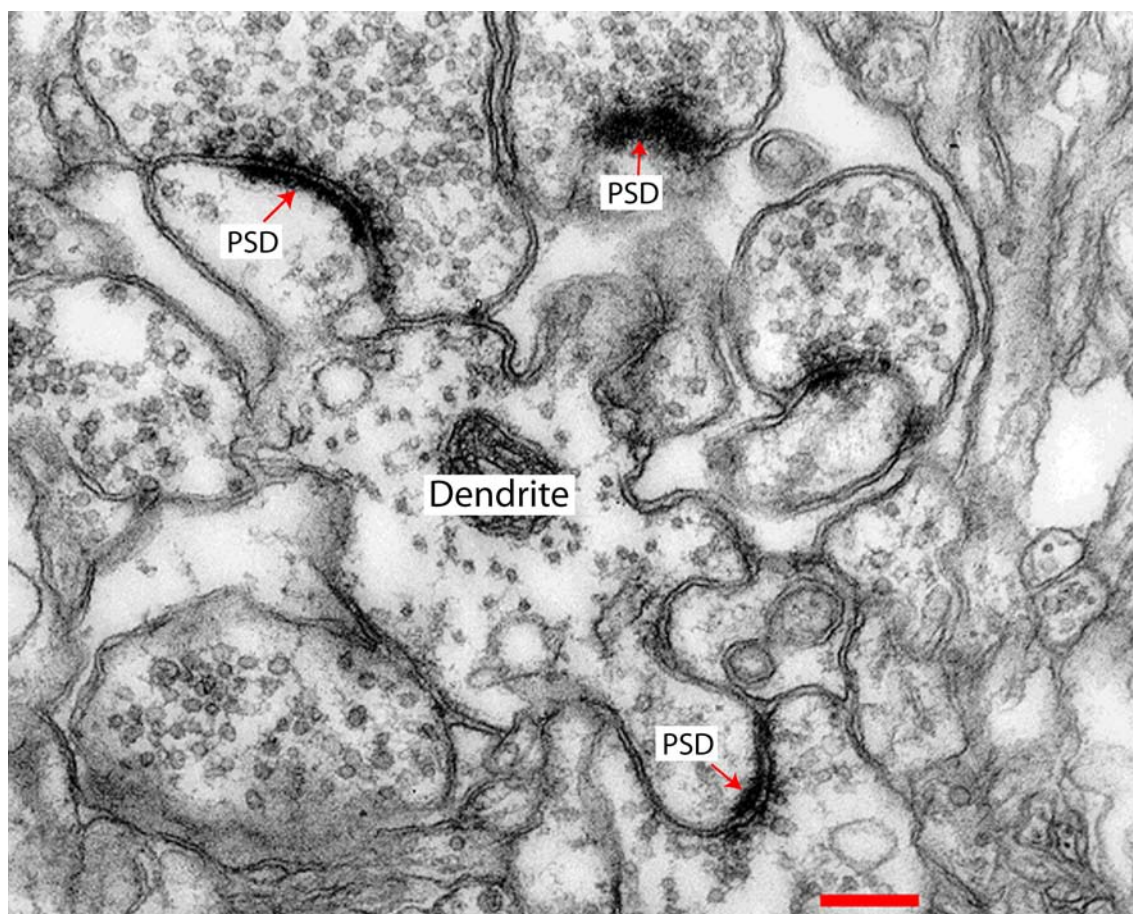


**Fig. 3** *Postsynaptic densities in thin sectioned neuronal tissue.* Adapted with permission from: Synapse Web, Kristen M. Harris, PI. Image contribution by Josef Spacek. Scale bar represents 500 nm.

have been slightly modified over the last few decades they still act as a foundation for almost all PSD studies including those presented in this thesis.

As testament to the PSD's complexity, mass spectrometry has revealed hundreds of proteins within PSD fractions along with variations in the protein composition of PSDs from different brain regions (Cheng et al., 2006; Peng et al., 2004). Using PSDs isolated from cultured hippocampal neurons Michael Ehlers provided a glimpse into the organelle's dynamic nature by showing activity dependent alterations in protein composition that were not only reversible but of a modular nature. That is to say signaling molecules common to known pathways were seen to undergo concerted compositional changes when subjected to different experimentally controlled activity levels (Ehlers, 2003). Techniques for examining protein-protein interactions (yeast two-hybrid and immuno-precipitation methods) have verified binding between resident PSD proteins such as the scaffolding molecule PSD-95 and NMDARs (Kornau et al., 1995) as well as NMDARs and the signaling molecule CaMKII (Gardoni et al., 1998). In light of what is now known about the PSD's molecular composition and mounting evidence that protein-complexes play a key role in generating both signaling efficiency and specificity, it is clear that a sound understanding of the structural and functional logic employed by PSDs will be essential in the study of chemical-signal processing at excitatory synapses.

### **Synapses, Learning and the Development of Neural Circuitry**

Development of the nervous system is entirely dependent on the proper formation of synaptic contacts. It is through the networking of cells via synaptic connections that neuronal circuitry is established, and it is through these networks that areas of the brain become specialized for processing specific types of information. New synapses are constantly being formed and old synapses removed in response to individual experiences with external stimuli. It is also well documented that the properties of existing synapses are plastic, and can be altered in an activity-dependent manner. The mechanisms underlying synaptic plasticity have been

under investigation for decades, and many different mechanisms have been discovered. In general, synapses must undergo some chemical change that alters the existing synaptic machinery or the machinery itself can be altered structurally through the addition or removal of molecular components. Regardless of the mechanism, it is without question that the formation of synaptic contacts and their proper function is essential to brain development and the brain's ability to store information in the form of learning and memory. It will be discussed in more detail later, but studies with mutant mice (deficient in CaMKII or with point mutations that alter its regulation) have clearly demonstrated the molecules role in synaptic plasticity and shown that disturbances in spatial learning accompany the loss of plasticity (Giese et al., 1998; Silva et al., 1992a; Silva et al., 1992b).

The number of synapses that exist in the brain through out development has long been a question of interest. Studies in humans, monkeys and rats have all yielded similar results, showing that shortly after birth there is an explosion in the number of synapses that exist (Bhatt et al., 2009; Huttenlocher, 1979; Markus and Petit, 1987; Rakic et al., 1986). In rats it was shown that synaptic density in specific brain regions was correlated with the development of behavioral traits reliant on those brain regions (i.e. motor skills and motor cortex, (Markus and Petit, 1987)). In all studies the massive formation of synapses shortly after birth was later followed by a steady decline in the number of synapses. Although the rate of decline slowed dramatically by adulthood, the number did continue to drop into old age. From these studies a picture has emerged where the brain initially generates an over abundance of synaptic connections in an attempt to maximize its potential (in a sense, not knowing what will be demanded of it by its environment). Later, the connections that are not used are pruned away and the ones that are used frequently are strengthened and honed to better perform specific tasks. Because of this, the phrase “use it or lose it” has been used by some to describe our brains potential. However, due to genetic and environmental influences, it is likely not so

straightforward. While the notion of synaptic pruning was introduced by Ramon Y Cajal more than 100 years ago (Cajal, 1899), it has since been confirmed in a variety of preparations, spanning from neuronal cultures to fixed tissue, brain slices and most recently in living animals (Grutzendler et al., 2002; Majewska et al., 2006; Zuo et al., 2005a).

There is now a host of evidence supporting the idea that synapse formation/elimination during development is regulated by experience and patterns of electrical activity (Dunaevsky et al., 1999; Engert and Bonhoeffer, 1999; Maletic-Savatic et al., 1999; Zuo et al., 2005b). For example, Zuo et al. (2005) showed, using two-photon microscopy of neurons in the somatosensory cortex of living rats, that sensory deprivation preferentially slowed the loss of synapses during development. Perhaps the strongest evidence for experience-dependent shaping of neural circuitry has been observed in the visual cortex, mainly through the work of Hubel and Wiesel (Wiesel, 1982). Their work with sensory deprivation and ocular dominance columns of the visual cortex has provided some of our deepest insight to effects of sensory input on the development of brain circuitry. Although there is still a lot to learn about the precise roles that synapse formation/elimination and synaptic plasticity play in brain development, it is becoming increasingly clear that events occurring at the microscopic level in our brains are playing a huge role in determining its output, and in turn, our behavior.

### **Synaptic Plasticity**

Activity-dependent changes in the strength of synaptic transmission have been known to occur for more than fifty years, but characterizing the different forms and the molecular mechanisms underlying these physiological changes in transmission has been very difficult. By no means do we fully understand synaptic plasticity, but it is now widely accepted that changes in synaptic physiology are one of the major mechanisms for memory storage in the brain. Several different forms, spanning several different temporal ranges, have been studied extensively. The location of their expression depends on the type of plasticity observed and



how it is elicited. Generally, shorter forms of plasticity such as short-term potentiation and depression (STP and STD) occur mainly on the presynaptic side through short lived changes in the release probability of synaptic vesicles or the depletion of vesicles available for release (Fisher et al., 1997). Long-term potentiation and depression (LTP and LTD), on the other hand, are believed to impart long lasting changes through the structural rearrangement of synaptic components or stable chemical changes in existing components. The site of action for most of these changes has been located to the post-synaptic side and they typically involve changes in the protein composition of the PSD.

Over the past 20 years or so the mechanisms underlying LTP have been extensively studied, and there was a great debate over whether it occurs pre- or postsynaptically. Today it is generally accepted that LTP is expressed postsynaptically as an increase in the number of AMPA receptors available to detect neurotransmitter release which inherently increases the number of ion channels available to conduct ions across the plasma membrane (Bredt and Nicoll, 2003). Another contributing factor is the phosphorylation of the AMPA receptor subunit GluR1 at Ser831 by CaMKII and PKC (Maletic-Savatic et al., 1999; Roche et al., 1996). Phosphorylation at this site increases the unitary conductance of AMPARs which leads to an increased postsynaptic current in response to transmitter release (Benke et al., 1998; Derkach et al., 1999). Seeing that AMPA receptors are anchored at the synapse via scaffolding in the PSD, it makes sense that synaptic plasticity would entail structural changes in the PSD. Presumably these activity-dependent changes will be reflected in any changes seen during development.

The late phase of LTP, which can persist for days or weeks, requires protein synthesis and gene transcription. CaMKII, PKA and MAPK are all thought to link LTP inducing stimuli to gene transcription through the activation of CREB. Multiple studies with mutant mice deficient in CaMKII or expressing a non-phosphorylating mutant of the kinase have solidified the critical role of CaMKII function in both synaptic plasticity and learning (Frankland et al., 2001;

Glazewski et al., 1996; Glazewski et al., 2000; Kimura et al., 2008; Silva et al., 1992a; Silva et al., 1992b; Taha et al., 2002). It is known that potentiated synapses undergo morphological alterations that lock in changes in synaptic strength. Indeed growth of new dendritic spines, enlargement of pre-existing spines and their postsynaptic densities (PSDs) has been observed in response to LTP (Harris et al., 1992; Lamprecht and LeDoux, 2004). Based on the available evidence a model for LTP has emerged where LTP initially involves the insertion of AMPARs and other molecules into the PSD which leads to structural changes in the PSD and spine. Simultaneously, or soon after, an increase in the presynaptic active zone occurs (the size of the active zone always closely corresponds to the size of the PSD). In this model LTP involves the increase in strength plus the physical growth of the synapse (Malenka and Bear, 2004).

### **Ca<sup>2+</sup> / Calmodulin-Dependent Kinase II (CaMKII)**

CaMKII is a multifunctional kinase whose activity is regulated by the ubiquitous calcium-sensing protein calmodulin (CaM). In the dendritic spine, Ca<sup>2+</sup>-influx through NMDA receptors leads to the activation of CaMKII and subsequent induction of LTP (Ito et al., 1991; Malenka et al., 1992). Therefore, exactly how CaMKII activation is regulated is a subject of great interest among scientists studying synaptic plasticity. One of the most intriguing aspects of CaMKII regulation is that after activation by CaM, autophosphorylation at Thr286 leads to a CaM-independent active state (Lou and Schulman, 1989; Miller et al., 1988; Schworer et al., 1988). This activated state can then persist even after intracellular [Ca<sup>2+</sup>] returns to basal levels, which allows the kinase to encode information about a synapse's activation history (steps involved in activation and regulation of CaMKII are outlined in Fig. 4). Because of this CaMKII is sometimes called a “memory” molecule, and indeed phosphorylation of Thr286 has been shown to play a crucial role in the expression of LTP and spatial memory (Frankland et al., 2001; Giese et al., 1998; Kimura et al., 2008; Silva et al., 1992a; Silva et al., 1992b).

There are four genes in mammals that encode four isoforms of the kinase (alpha, beta, gamma, delta). All contain an N-terminal catalytic domain and a C-terminal association domain that organizes the subunits into a dodecameric structure (Kolb et al., 1998). Although holoenzymes can be constructed using a variety of isoform combinations, the alpha form is found predominantly in neurons. The Waxham lab has determined the structure of all four of the mammalian isoforms using single particle reconstruction. All are dodecameric complexes with six-fold rotational symmetry in which the association domains of each subunit combine to form a double-layered core complex with six catalytic domains extending radially from both ends of the core (Gaertner et al., 2004; Kolodziej et al., 2000). Fig. 4 shows the EM reconstruction of the alpha isoform, and this unique structure has lead to the proposal of a scaffolding role for CaMKII in addition to its enzymatic capabilities. This is indeed possible as our lab has shown that the enzyme can undergo a regulated process of self-association (Hudmon et al., 2005) as well as interact with PSD proteins such as NMDARs,  $\alpha$ -actinin, and Densin-180 (Gardoni et al., 1998; Walikonis et al., 2001). The six-fold symmetry could allow binding of multiple partners to the same CaMKII holoenzyme and lead to the clustering of NMDARs or assembly of larger signaling modules composed of a variety of proteins. In either case there are profound implications with respect to the regulation of CaMKII, and understanding the nature of these interactions is critically important in delineating the complexities of the PSDs protein machinery.

### **CaMKII in the PSD**

CaMKII is the major signaling protein of the postsynaptic density, making up 2-3% of protein from isolated PSD preparations (Suzuki et al., 1994). Using quantitative western blotting it has been estimated that there are 80 CaMKII holoenzymes per PSD, but immunogold staining has revealed high variability in the number of holoenzymes found from PSD to PSD (Chen et al., 2005; Petersen et al., 2003). This variability is likely explained by the fact

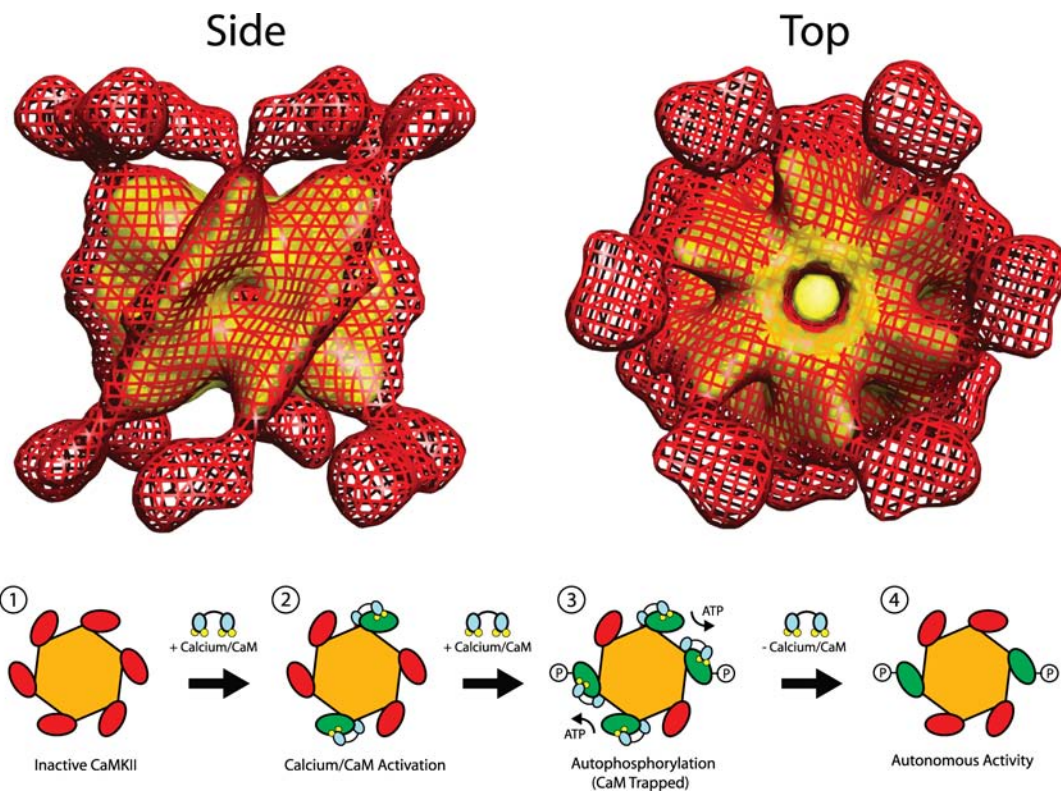


**Fig. 4** Structure of CaMKII holoenzyme and diagram of its regulation.

that PSDs isolated during cellular fractionation come from synapses with widely varying activation histories, and CaMKII composition is known to change in an activity-dependent manner (Ehlers, 2003). Intriguingly, immuno-gold staining showed that regardless of CaMKII density within individual PSDs there is an average distance of 30nm between holoenzymes, suggesting CaMKII incorporates into PSDs with a characteristic local density (Petersen et al., 2003). The factors underlying this spatial regularity are not known, but interactions with the cytoplasmic tail of NMDARs are an attractive candidate due to their established CaMKII binding properties (Gardoni et al., 1998; Strack et al., 2000). Stimulation of neurons drives the translocation of CaMKII into the dendritic spine where it is incorporated into the PSD (Dosemeci et al., 2001) via interactions with NMDARs (Shen and Meyer, 1999). The physiological implication of CaMKII's interaction with the NMDAR is of particular interest as it regulates a synapses ability to undergo LTP (Barria and Malinow, 2005). The kinase's binding to  $\alpha$ -actinin (Walikonis et al., 2001) is also of interest as it could link the PSD to the actin cytoskeleton which is known to undergo dynamic rearrangement in response to synaptic activity (Lippman and Dunaevsky, 2005).

It is clear that CaMKII is an important PSD component owing to its high concentration within the volume of the organelle (100-200uM; (Lisman and Zhabotinsky, 2001)), but the precise nature of its role (enzymatic, scaffolding or both) and its structural arrangement within the PSD are not well characterized. Knowledge of CaMKII's orientation within the PSD and its proximity with respect to enzymatic targets, binding partners and regulatory phosphatases would go a long way toward uncovering the structural logic implemented by the PSD in calcium signal transduction as well as reveal the kinase's role in organizing the structure of the postsynaptic density.

### **Assembly of the PSD**

The mechanisms of assembly of the PSD are still largely unknown. In cultured neurons there is strong evidence that the presynaptic release machinery is trafficked to the developing synapse in pre-assembled complexes via transport vesicles (Ahmari et al., 2000; Shapira et al., 2003). These vesicles presumably fuse with the presynaptic membrane, embedding the vesicle release machinery, and forming a competent synapse capable of evoked vesicle release. Whether this type of assembly is used to construct PSDs is not clear. Some studies have reported movement of protein clusters labeled positively for postsynaptic components (Prange and Murphy, 2001; Washbourne et al., 2002), while other data suggests that postsynaptic components are recruited gradually over time in a sequential manner, with different components displaying different temporal kinetics in their recruitment (Bresler et al., 2001; Bresler et al., 2004; Friedman et al., 2000; Rao et al., 1998). These conflicting results have left the process of PSD development somewhat ambiguous and are a major motivation for the present study. While electron microscopy of PSD isolated at different stages of development cannot speak directly to the assembly process of individual PSDs, I believe the observations made in this thesis provide unprecedented insight to the potential stages of PSD assembly.

## Methods

### *Isolation of Postsynaptic Densities*

Subcellular fractions enriched in postsynaptic densities were obtained from rat brains by using a slightly modified version of the protocol developed by Cohen *et al.* (Cohen et al., 1977). Forebrains from female Sprague-Dawley rats at ~P60 (160-180 g) were harvested within 30 sec of decapitation and placed in ice cold isotonic sucrose solution (0.5 mM Hepes, pH 7.4, 0.32 M sucrose, 1 mM MgCl<sub>2</sub>, 0.5 mM CaCl<sub>2</sub>, and 1 µg/ml leupeptin) followed by disruption in a motor driven glass/Teflon homogenizer. After crudely clarifying the homogenate by centrifugation at 1,400 x g for 10 min the supernatant was centrifuged again at 13,800 x g for 10 min and the pellet was resuspended in isotonic solution (0.5 mM Hepes, pH 7.4, 0.32 M sucrose, and 1 µg/ml leupeptin). A synaptosomal preparation was obtained by centrifugation of the resuspended pellet through a discontinuous sucrose density gradient (1.0 M-->1.4 M) at 110,000 x g for 2 hr. The synaptosomal fraction was recovered from the interface between the 1.0 M and 1.4 M sucrose. Synaptosomes were then solubilized using 0.5% Triton X-100, followed by another centrifugation step on a second sucrose gradient (1.0 M-->1.5 M-->2.1 M) and synaptic junctions were recovered from the interface between the 1.5 M and 2.1 M sucrose. A second detergent extraction with 0.5% Triton X-100 plus 75 mM KCl strips away residual pre- and postsynaptic membranes, and centrifugation across a final sucrose gradient (1.0 M-->1.5 M-->2.1 M) resulted in a final fraction highly enriched in PSDs at the interface between the 1.5 M and 2.1 M sucrose. The PSDs were collected from the interface, diluted in 5 mM Hepes, pH 7.4, pelleted and then resuspended in 5 mM HEPES, pH 7.4. Samples were either used immediately or made into aliquots containing 20% glycerol and frozen for storage at -80°C. To isolate PSD from rats at E19 and P2 the same protocol was followed, but volumes and sucrose gradients were scaled down in size to compensate for the smaller amount of starting

tissue. For P60 PSD preparations, 9 rat forebrains were routinely used. At P21, one litter was used which generally consists of 10-13 pups. Three litters (~36 pups) were used for a P2 preparation and embryos (~60) from five pregnant females were used as starting material for E19 preparations.

### ***Antibody Characterization***

All primary antibodies used in this paper exhibit high specificity by Western blot of brain homogenate and PSD fractions as shown in Fig. 1.4 and 1.5. All antibodies labeled a single band at the expected molecular weight for the target protein ( $\alpha$ CaMKII: 54 kDa,  $\beta$ CaMKII: 60 kDa,  $\alpha$ -Actinin: 100 kDa, CaM: 17 kDa, NR1: 120 kDa, NR2b: 170 kDa, GluR1: 106 kDa, PSD-95: 95 kDa).

### ***Immunolabeling of Postsynaptic Densities and Electron Microscopy***

Four microliters of isolated PSD sample (~1  $\mu$ g/ $\mu$ l) was placed on a formvar/carbon coated copper EM grid (freshly glow-discharged) and allowed to sit for one min. Excess sample was blotted away with filter paper and the grid was floated sample-side-down on top of 40  $\mu$ l of blocking buffer (5% BSA in PBS, pH 7.4) for 10 min. The grid was then moved to 30  $\mu$ l of blocking buffer containing a dilution of the primary antibody for 30 min. In these experiments, primary antibodies included monoclonal antibodies targeted to PSD-95 (ABR, MA1-046, 1:20),  $\alpha$ -actinin (Sigma, 1:20),  $\alpha$ CaMKII (homemade, 1:20),  $\beta$ CaMKII (CB- $\beta$ 1, 1:100), NR1 (Millipore, 1:10), NR2b (Chemicon, MAB5778, 1:20), GluR1 (UpState, 1:10) and CaM (Upstate, 05-173, 1:5). After incubation with the primary antibody, grids were washed three times (twice for 2 min and once for 10 min) on drops of blocking buffer before a 30 min incubation on 30  $\mu$ l of blocking buffer containing a 1:5 dilution of 12 nm gold-conjugated secondary antibodies (Jackson ImmunoResearch). After incubation with the gold-conjugated secondary, grids were washed three times as before but with water to remove residual salt, and negatively stained with Nanovan (Nanoprobes). Control PSDs were treated in the exact same



way however no primary antibodies were applied. Prior to all immuno-labeling for quantification a titration with each primary antibody was performed to insure a concentration with maximal labeling density. The same titration was also performed using the 12 nm gold-conjugated secondary antibody.

After immuno-labeling and negative staining, PSDs were imaged in the electron microscope (either with a JOEL CX100 or a FEI Polara F30) and digital micrographs were collected using a CCD. Micrographs of approximately 20 randomly selected PSDs were collected for each antibody at each developmental time point for subsequent quantitative analyses.

### ***Electron Tomography and Image processing***

For tomography, four microliters of PSD fraction were placed on a formvar/carbon coated copper EM grid (200 mesh) and allowed to sit for one min. At which point, excess sample was blotted away and the grid was washed twice with 5  $\mu$ l of milli-Q water, before negative staining with Nanovan. The staining solution contained 1  $\mu$ g/ml bacitracin for even wetting on the grid surface and a 1:20 dilution of 10 nm colloidal gold balls (Sigma) for use as fiducial markers during alignment. PSDs that met morphological criteria were used to generate tomographic tilt-series on a 300kV FEI Polara F30 electron microscope at 63,000x magnification. Images were collected at two degree tilt increments from -60 to 60° with 2X binning on a 4K x 4K Tietz CCD, which generated a final pixel size of 1.154 nm/pixel. Using the 10 nm gold fiducial markers included in the sample the images in the tilt series were aligned and tomographic reconstructions were generated using the IMOD software package (<http://bio3d.colorado.edu/imod/>).

### ***Cryo-Electron Microscopy***

All cryo-preserved samples were prepared on 200 mesh copper EM grids with a Quantifoil carbon support. The carbon support had 2  $\mu\text{m}$  holes with a 2  $\mu\text{m}$  periodicity. Before freezing grids were always glow discharged to produce a hydrophilic surface. Samples were prepared for freezing by spinning PSDs out of the 20% glycerol solution used for storage (20 min at 14,000 rpm in 4° desktop microfuge) and then resuspending them in 5 mM HEPES, pH 7.4 containing 10 nm colloidal gold (Sigma). To prepare the colloidal gold solution 100  $\mu\text{l}$  of colloidal gold was pelleted for 20 min at 14,000 rpm in a desktop microfuge and then resuspended in four times the volume (400  $\mu\text{l}$ ) of 5 mM HEPES, pH 7.4. The solution was then put in a sonicating water bath for 5 min to try and minimize clustering of gold.

Three  $\mu\text{l}$  of PSD were then applied to the Quantifoil grid and cryo-preserved using a Vitrobot (FEI) at the following settings: Temp (22°C), Humidity (80%), Blot Offset (0), Blot Time (5 sec). Samples were then kept under liquid nitrogen until they were loaded into the microscope. Tilt-series were collected on an FEI Tecnai F30 Polara, with a computer controlled cryo-stage. Tilt-series were collected from +60 to -60 degrees with a 2 degree tilt increment. All tilt-series were collected in low dose mode with the sample being exposed to less than 200 electrons/ $\text{\AA}^2$  total dose. Images were collected at a magnification and camera setting that produced a pixel size of 1.2 nm/pixel. Tomographic reconstructions were then calculated using IMOD (<http://bio3d.colorado.edu/imod/>).

### ***Western Blotting***

First, 12  $\mu\text{g}$  of total protein from forebrain homogenate, the synaptosomal and PSD fractions were separated by SDS-PAGE using a 10% polyacrylamide gel. Separated bands of protein were then transferred to a nitrocellulose membrane and incubated overnight in blocking buffer (5% dry milk in wash buffer) at 4°C. After blocking, membranes were incubated in a dilution of primary antibody (typically 1:1000) in blocking buffer for 1 hr at room temperature

on an orbital shaker. Membranes were washed 3 x for 5 min in wash buffer (10 mM Tris, pH 8.0, 150 mM NaCl and 0.05% NP40) before application of the secondary antibody (Alexa 488-conjugated goat anti-mouse or goat anti-rabbit antibodies) at a dilution of 1:5000 in blocking buffer for 1 hr at room temperature on an orbital shaker. Incubation in the secondary antibody was followed by three more 5 min washes prior to imaging on a Typhoon laser scanner (GE Healthcare Life Sciences).

For Western blots of CaM it was necessary to add 10 mM EDTA to the SDS sample buffer and 1 mM EDTA to the 15% acrylamide gel and running buffer. Without the addition of EDTA the band detected by the CaM antibody does not migrate at the expected molecular weight as it is likely still in complex with other protein components or bound to calcium.

### ***Point Pattern Analysis of Gold Particle Distribution***

We employed Ripley's K-function analysis to assess the distribution of gold particles (Ripley, 1977). The K-function,  $K(r)$ , expresses the expected number of neighboring gold balls within a given distance  $r$ .  $K(r)$  represents an analysis of inter-gold particle distribution patterns in a given region at all distance scales.

For this point pattern analysis, the X-Y coordinates corresponding to the center of each gold ball are needed. To do this a binarized image of the gold balls associated with each PSD was generated and the coordinates for the centroid of each gold particle was extracted using ImageJ (NIH). Using these coordinates for each set of points on a PSD, a convex hull encompassing all of the internal points was generated.

We used Ripley's K-function to compare experimentally determined patterns to the null hypothesis of complete spatial randomness (CSR). In order to do so, we need to know the K-function for a random particle distribution for each PSD. Except for a regular shaped boundary (e.g., a square or circle), such a function is usually not known, and taking into account the edge effect of a complicated boundary, like the edge of the PSD, is not an easy task. One way to

overcome this problem is to simulate the inter-particle distance distribution and evaluate the K-function numerically via Monte Carlo simulation (Yamada and Rogerson, 2003) and we employed this approach. One hundred sets of randomly distributed gold particles were simulated and then the mean, upper, and lower envelopes of the K-function for each set of simulations for a given convex hull were calculated. We then compared these simulation results (i.e., the inter-particle distribution) with the experimental data.

Simulated gold particles were generated as follows. As mentioned earlier, we calculated a convex hull for each particle set. We then used the boundary of this convex hull to generate a PSD of 60 nm thickness. Simulated gold particles were then randomly distributed within this 3D volume at the same labeling density (of internal points) as those in the given PSD particle set. We impose the volume exclusion principle, i.e., the distance between two simulated gold particles must be larger than the diameter of the actual gold particle (12 nm). In addition, the minimum distance of 6 nm was imposed on the inter-particle distance projected on to the 2D plane, as this is the minimal distance (the radius of the gold ball) at which two gold balls are easily distinguished in the raw 2D image data.

Finally, we compared the distribution of gold balls for each PSD to the upper or lower envelopes of the K-function defined by the 100 simulations of complete spatial randomness. The null hypothesis was rejected when the experimental data do not lie entirely between the upper and lower envelope of the simulated data (the envelope test, see Chapter 7 in (Illian et al., 2008)). All of the analysis and the simulations were done using MATLAB (The MathWorks, Natick, MA).

When deciding how to analyze the spatial distribution of the gold balls we also evaluated the Pair Correlation function as well as nearest neighbor analysis. Illian et al. (2008, Chapter 3) suggests that RKF was the most appropriate method to use when the data is confined within limited boundaries such as in the PSD. Our final decision to use Ripley's K function was based

on the fact that the small size of some of our data sets caused both of the other techniques to produce plots with substantial fluctuations that were difficult to interpret.

## **Results**

### **Chapter 1: Isolation of Adult PSDs and their Morphological/Biochemical Characteristics**

#### **Isolation of PSDs**

As mentioned earlier, one of the largest breakthroughs in our ability to study PSDs directly was the development of an isolation protocol during the 1970's (Cohen et al., 1977; Cotman et al., 1974). Two groups pioneered this effort and showed that by first generating a subcellular fraction rich in synaptosomes (pinched-off nerve terminals with the postsynaptic membrane and PSD still attached), they could then take advantage of the PSDs insolubility in various detergents to strip it away from the cell membrane (Fig. 1.1). The procedure begins by homogenizing rat forebrain and partially clarifying the homogenate with a low-speed spin in a centrifuge. A subsequent medium-speed spin pellets a fraction of the homogenate containing the synaptosomes. A fraction highly enriched in synaptosomes is next obtained by separation through a discontinuous sucrose gradient. With a synaptosomal prep in-hand, synaptic junctions can be isolated through the solubilization of the presynaptic terminal membrane with the non-ionic detergent Triton X-100. Synaptic junctions are a fraction of the synaptosome that consists of the PSD, the trans-synaptic junctional proteins and the portions of the pre- and postsynaptic membrane sandwiching the synaptic cleft. Centrifugation through a second sucrose gradient separates the synaptic junctions from the components solubilized by the Triton X-100. A second detergent extraction with Triton X-100 and KCl helps to strip away the remaining plasma membrane as well as peripheral membrane proteins, and a final spin through a sucrose gradient is used to isolate a fraction highly enriched in postsynaptic densities. In order to test whether our protocol is properly enriching our sample in postsynaptic densities, samples are taken at each major step during the isolation process. Equal amounts of protein (12 ug total) from each fraction is then loaded on a polyacrylamide gel and separated by electrophoresis. Separated proteins are transferred to a membrane for Western blot analysis. Fig. 1.1 B shows

## PSD Isolation Process

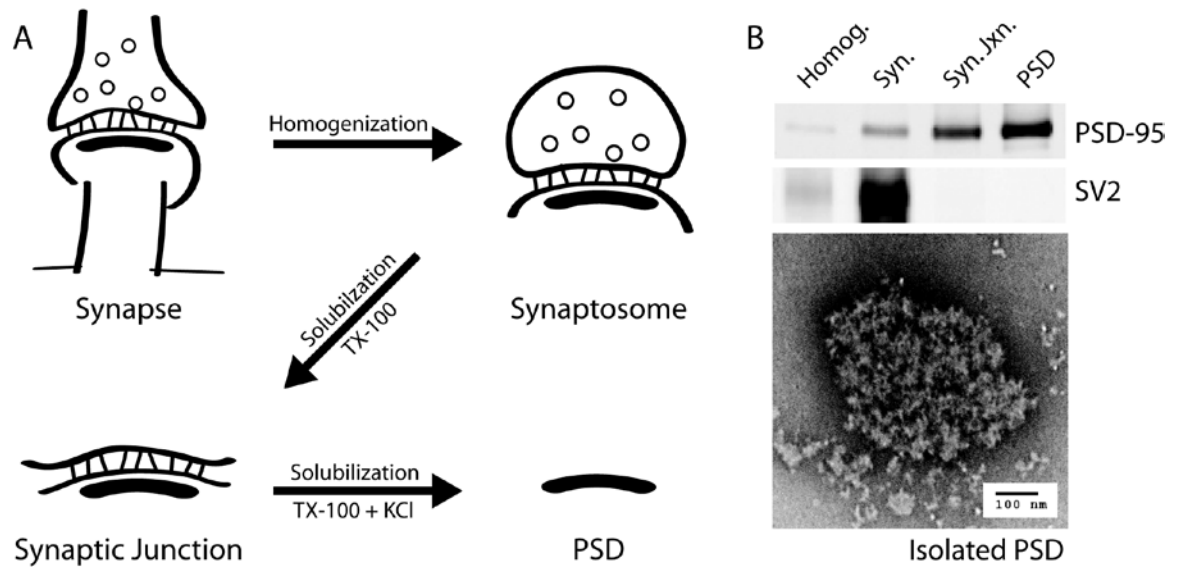


**Fig. 1.1** *Schematic of PSD Isolation and Characterization of Isolated PSDs.*

(A) The first stage of the PSD isolation process is to homogenize forebrain material. During the homogenization intact synapses are disrupted and presynaptic terminals are pinched-off and reseal to form synaptosomes. Solubilization of the terminal portion of the synaptosome with Triton X-100 (TX-100) and separation by centrifugation leaves behind synaptic junctions. A final solubilization step with the addition of KCl strips away the remaining synaptic membrane and peripheral membrane proteins to produce a fraction highly enriched in postsynaptic densities. The top panel of (B) shows Western blot analysis of the fractions shown in (A) reveal a sequential increase the postsynaptic scaffolding protein PSD-95. The presynaptic vesicle protein SV2 enriches from homogenate to synaptosomes, but then falls out almost entirely after solubilization with TX-100. The lower panel is an electron micrograph of a negatively stained PSD isolated with the described protocol.

Western blot analysis of the fractions using antibodies against the PSD scaffolding protein PSD-95 and the synaptic vesicle protein SV2. PSD-95 is a scaffolding molecule that is abundant in mature PSDs (Chen et al., 2005; Petersen et al., 2003) and it is often used as a PSD marker for studying synapses. As one would expect, if the protocol is enriching in PSDs, the Western blot for PSD-95 shows an obvious sequential increase in each of the fractions collected during the isolation process. The presynaptic vesicle protein SV2 enriches greatly from the homogenate to the synaptosomal fraction, but as expected it drops out almost entirely after solubilization of the presynaptic components with Triton X-100. This further supports that the protocol is specifically enriching in postsynaptic and not presynaptic components.

The bottom panel of Fig. 1.1 B shows an electron micrograph of a PSD from the final step of the isolation process. The PSD is negatively stained and reveals both the amorphous nature of the complex as well as the obvious complexity of its protein architecture. PSDs appear as roughly disc shaped complexes, because they bind to the carbon on the EM grid in a preferred orientation that represents one of the two enface views. They range in size from 200 nm to 1.2 microns in diameter across their widest point. These measurements are within the range of those described in previous publications (Cohen et al., 1977; Cotman et al., 1974; Matus and Taff-Jones, 1978; Petersen et al., 2003). According to biochemical and electron microscopic analysis, the PSD isolation protocol efficiently fractionates rat forebrain and provides a subcellular fraction highly enriched in postsynaptic densities. On average nine adult rat forebrains weighing approximately 1.5 g each will provide 500-800 ug of total PSD protein.

### **General Morphology in EM**

The overall morphology of PSDs has been well described through electron microscopy preparation techniques. They were first seen in thin sections of resin embedded, negatively stained nervous tissue where Gray (Gray, 1959a; b) noticed that excitatory synapses had an asymmetric distribution of protein density. He referred to these as Type 2 synapses and typical



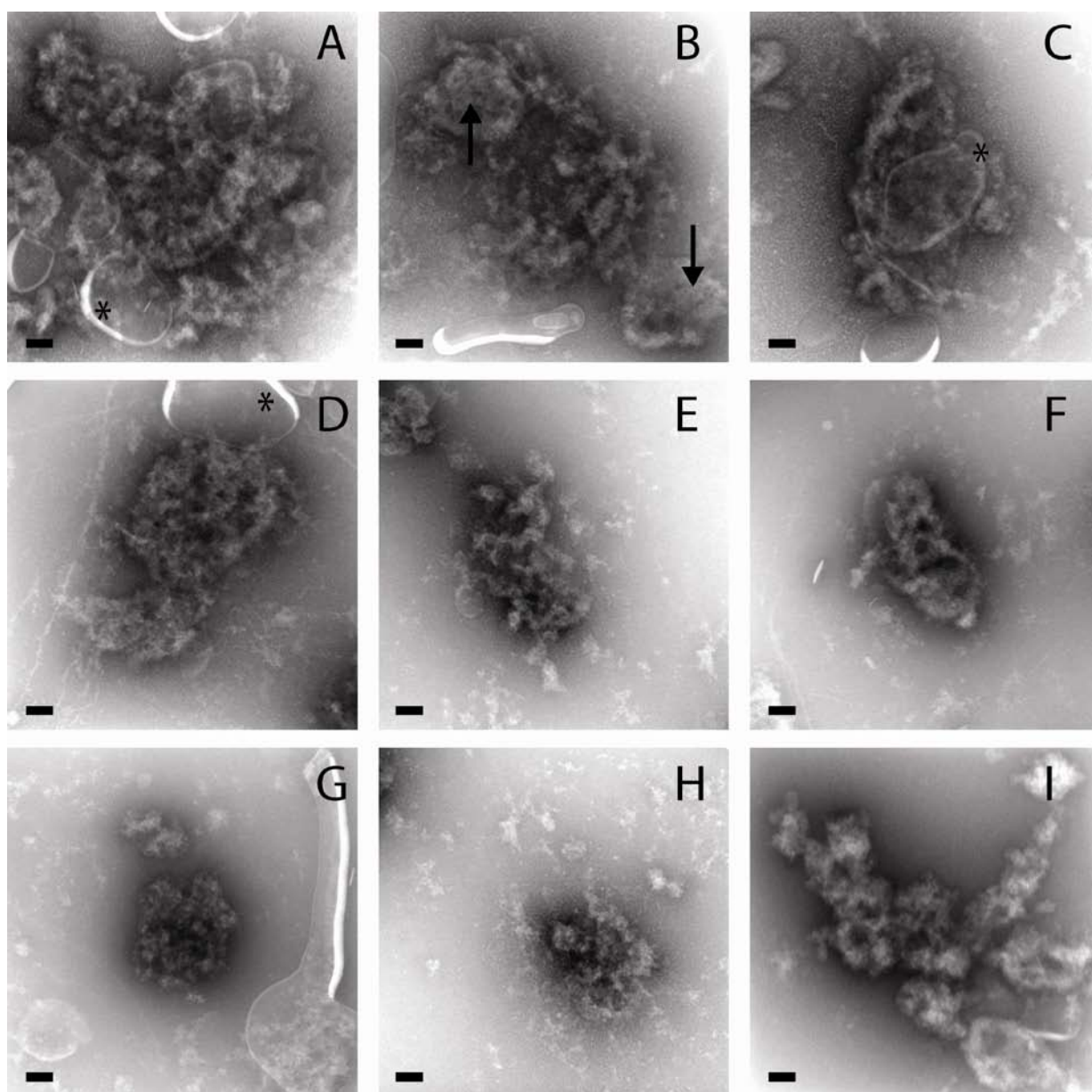
examples are shown in Figs. 1 and 3 in the Introduction. When they were first isolated from brain tissue they were characterized in thin sections of pelleted PSD fractions following subcellular fractionation (Cotman et al., 1974). More recently they have been described through the application of isolated PSDs directly to surfaces such as carbon coated EM grids. Using this method they have been visualized in both negative stain such as uranyl acetate or platinum shadowed to increase contrast in the microscope. Depending on the study the dimensions vary, but they range in size from 200-1200 nm in diameter and 40-80 nm thick.

Fig. 1.2 shows a low magnification electron micrograph (~6000x) of isolated PSDs negatively stained on a formvar/carbon EM grid. This field of view is selected to illustrate the variety of objects that can be found in the PSD fraction including contaminants. Six obvious PSDs are spread out across the carbon support in this micrograph, and they have been circled to make them easy to locate. Notice that they are of various size and shape. Even though the PSDs are subjected to detergent (0.5% Triton X-100) during the isolation process not all of the membrane is removed, and can be seen as a smooth white mass with a bright white edge where the membrane folds over. This membrane is typically associated with a PSD, and is labeled in this micrograph by the asterisk. While most membrane is in contact with a PSD there is sometimes free membrane attached to the grid. However, no free membrane is visible in this field of view. There are two major types of protein contaminants visible in this image. One of them is the bundle of filamentous protein indicated by the large arrow, and the other is the small globular protein complexes indicated by the small arrows. It is not clear what the bundled filaments are, but a likely candidate are intermediate filaments that could arise from astrocytes containing the glial acidic fibrillary protein (GFAP), or intermediate filaments composed of various neurofilament proteins. These intermediate filament proteins are one of the most notorious contaminants in isolated PSD fraction and are identified in almost many proteomic studies of PSD fractions (Cheng et al., 2006; Dosemeci et al., 2006; Peng et al., 2004). It is not



clear what the smaller globular complexes are. It is likely that some of them represent pieces of PSDs that have broken off during the isolation process, and sometimes they do immuno-gold label for PSD components. They do not always label though, so some of them probably represent non-PSD contaminants. It is also possible that some of them are clusters of CaMKII that have been documented to form under the ischemic conditions that follow decapitation during the isolation process (Dosemeci et al., 2000; Tao-Cheng et al., 2002; Tao-Cheng et al., 2005). CaMKII clusters have been described in PSD fractions that label heavily for CaMKII with immuno-gold staining (Dosemeci et al., 2000).

PSDs are often described as being disc shaped, but the variety of shapes is actually quite diverse. Fig. 1.3 shows a gallery of PSDs illustrating the range in shape and size. These PSDs were isolated from adult rats using the standard Triton X-100 isolation protocol, negatively stained on a formvar/carbon EM grid and imaged at approximately 35,000 times magnification. Panels A-H depict isolated PSDs spanning the size range from largest (just over a micron across) to smallest (~200 nm across). The scale bars represent 100 nm. The shape of the PSDs ranges from nearly circular (panel G) to elliptical (panel F) to entirely irregular (panel I). PSD dimensions have most often been reported in terms of diameter, but it is clear from the PSDs shown in panel I that sometimes it is impossible to accurately define a diameter. In fact, even when a PSD is roughly circular it is difficult to accurately define which axis is an appropriate representation of diameter. Because of this, the surface area was chosen as the most accurate measurement of size that allows PSDs of different shapes to be objectively compared. As in Fig. 1.2 asterisks are used to denote membrane that is in association with a PSD. There is some free membrane in panels B and G that are not labeled. Arrows in panel B denote subregions of the PSD that are roughly circular and have a smoother appearance. These structures are present in a subpopulation of PSDs, but are only seen in panel B of Fig. 1.3.



**Fig. 1.3** *High magnification views of individual isolated PSDs.*

Electron micrographs of individual PSDs in an *en face* view. PSDs are arranged from largest (panel A) to smallest (panel H) to illustrate the range of sizes seen in a single PSD preparation. Panel I illustrates a largely irregular PSD. Clearly, there is a wide range of shapes and sizes that PSDs can assume. Scale bars represent 100 nm.

### **A subset of proteins are enriched during the isolation process**

Because PSDs are only one of many organelles found in the brain, their protein components presumably represent only a subset of the proteins found in the brain. Therefore, during the isolation protocol one would expect to see a smaller and smaller subset of proteins being enriched at each step of the process. As expected, SDS-PAGE of protein samples taken through the isolation process reveals that, in fact, a subset of proteins is enriched for in the PSD fraction when compared to the preceding fractions. Fig. 1.4 shows the results of a Coomassie stained polyacrylamide gel used to separate proteins from brain homogenate, synaptosomes and the final PSD fraction. Twelve micrograms of total protein were loaded in each lane. Interestingly, the overall protein profile of the synaptosomes is very similar to that of the homogenate. A few bands do disappear from homogenate to the synaptosomal fraction and these proteins are labeled by the arrowheads in the homogenate lane. Because the nerve terminal is in cytosolic continuity with the axon and therefore the neuronal cytosol, it is likely that most of the general cytosolic proteins are present in both fractions. Since these molecules make up the majority of the protein in each fraction this could explain why the profiles are so similar. Because there are likely many minor bands which are not within the detectable range of the Coomassie staining method it is possible that there are additional proteins in the homogenate that are not present in the synaptosomal fraction, but their signal is simply too low to detect them. The protein profile of the PSD fraction shows an obvious enrichment in a subset of protein when compared to the synaptosomal fraction. Not only is there a significant number of major bands that drop out from synaptosomes to PSDs (indicated by the arrowheads next to the synaptosome lane), but there are also some major protein bands in the PSD fraction that are barely visible in the synaptosomal fraction. These bands are indicated by the arrows next to bands in the PSD lane. The appearance of new bands indicates that proteins that were minor components of the total synaptosome protein are enriched components of the PSD, and become

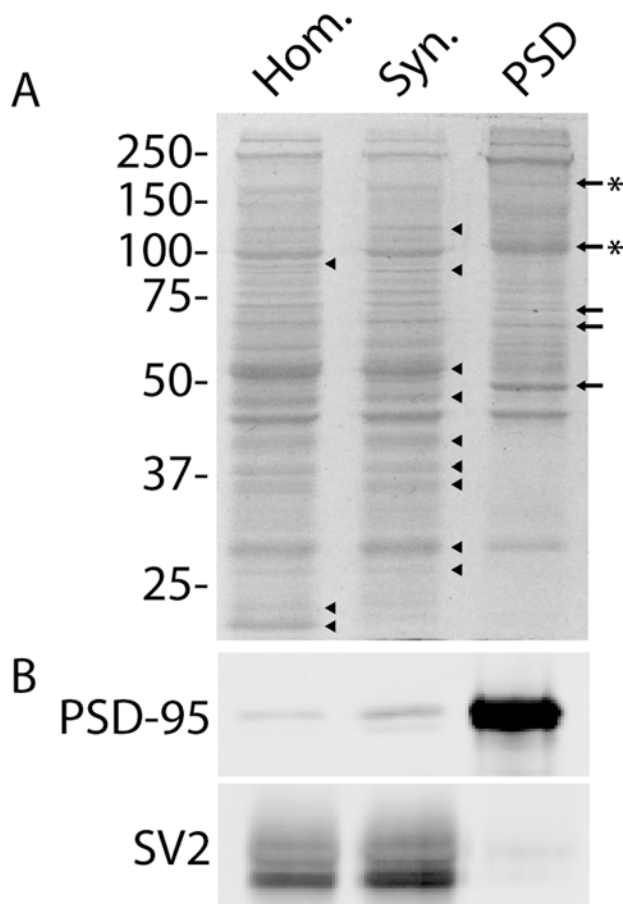


**Fig. 1.4** *Protein profiles of fractions during PSD isolation and enrichment of Pre- and Postsynaptic proteins.*

(A) Coomassie stain of individual fractions separated by SDS-PAGE. Equal protein (12 ug) was loaded of homogenate (Hom.), synaptosomes (Syn.) and PSDs. Number on the left indicate the relative position of molecular weight standards. Arrowheads indicate bands that drop out in the subsequent fraction. Arrows next to the PSD lane indicate bands that are enriched in the PSD fraction. Asterisks (\*) indicate bands that appear similar to those in other lanes, but upon closer inspection are a different molecular weight. (B) Western blots of protein from each of the three fractions collected during the isolation process. The postsynaptic protein PSD-95 clearly enriches through the process, while the presynaptic vesicle protein SV2 drops out after solubilization by Triton X-100, indicating that postsynaptic elements are being enriched.

more abundant after solubilization of synaptosomes with Triton X-100. There are some bands in the PSD lane that appear to be the same as one in the synaptosomes, but upon closer inspection are actually a different molecular weight than those in the previous fraction (these bands are indicated by the arrows with asterisks). Again, because the Coomassie dye stains total protein it is not possible to tell if they are the entirely different proteins or perhaps phosphorylated or post-translationally modified forms of the same protein species. It is also possible that they represent different isoforms of the same protein family

### **Enrichment of Proteins in the PSD Fraction**

As mentioned above, the PSD is composed of approximately 300 different proteins making it a complex organelle. This complexity makes it difficult to study, but this also means the PSD is rich with questions to answer concerning its structural organization and function. To begin to dissect the underlying structure of the PSD, a subset of eight different proteins were chosen that represent three important functional types of proteins in the organelle. These molecules include two scaffolding proteins (PSD-95 and  $\alpha$ -actinin), three glutamate receptor subunits (NR1, NR2b and GluR1) and three signaling molecules ( $\alpha$ CaMKII,  $\beta$ CaMKII and CaM). These three types of proteins can be thought of as the core of the PSD machinery, as the receptors receive incoming chemical signals from the synaptic cleft and their activation is complimented by the stimulation of its corresponding signaling pathways. These signaling pathways are presumably organized in the PSD via interactions between signaling molecules and the receptors and/or through scaffolding molecules that crosslink signaling pathways appropriately. Because of this basic organizational plan it seemed logical to start by studying a few key molecules from each protein class. In order to assess the enrichment of the eight proteins mentioned above in our PSD fraction 12 ug of total protein from forebrain homogenate, the synaptosomal fraction and the final PSD fraction were loaded next to each other on a 10% poly-acrylamide gel and separated by electrophoresis. Protein was then

transferred to a nitrocellulose membrane and the relative amounts of specific proteins across all three fractions were probed via Western blot. Results from Western blots for each of these proteins can be found in Fig. 1.5, and the detailed results are described in the sections below.

### *Scaffolding Molecules*

PSD-95, a 95 kDa scaffolding protein, is probably the most well studied scaffold molecule within the PSD. It is often used as a PSD marker in immuno-fluorescent microscopy studies, so it was an obvious choice as an initial protein component to probe for in our PSD fractions. As expected, there is enrichment in PSD-95 from the homogenate to the synaptosomal fraction as the majority of cellular material is removed and the fraction is enriched in synaptic material. Another large increase in PSD-95 is seen from the synaptosomal fraction to the final PSD fraction (Fig. 1.1B shows the Western blot for PSD-95 enrichment). As the presynaptic membrane of the synaptosomes is solubilized by the Triton X-100 the fraction becomes highly enriched in postsynaptic material and this is obvious in the enrichment of PSD-95.

$\alpha$ -Actinin is an actin cross-linking protein that is not traditionally thought of as a PSD protein, but seeing that the PSD is a cytoskeletal specialization at the postsynaptic membrane it is not surprising that it enriches from brain homogenate to the final PSD fraction. Surprisingly, there is not enrichment from homogenate to the synaptosomal fraction. Because this result was unexpected, this blot was repeated multiple times with multiple PSD preparations with similar results (data not shown). It is not entirely clear why the level of  $\alpha$ -actinin drops off so drastically in the synaptosomal fraction, but it must be related to the subcellular distribution of  $\alpha$ -actinin throughout the neuron. Perhaps it is not an abundant molecule in the presynaptic terminal and since synaptosomes are primarily composed of presynaptic material (and postsynaptic material),  $\alpha$ -actinin does not appear to enrich. Even though it is not visible in the blot shown in Fig. 1.5,  $\alpha$ -actinin is detectable in the synaptosomal fraction by adjusting the image



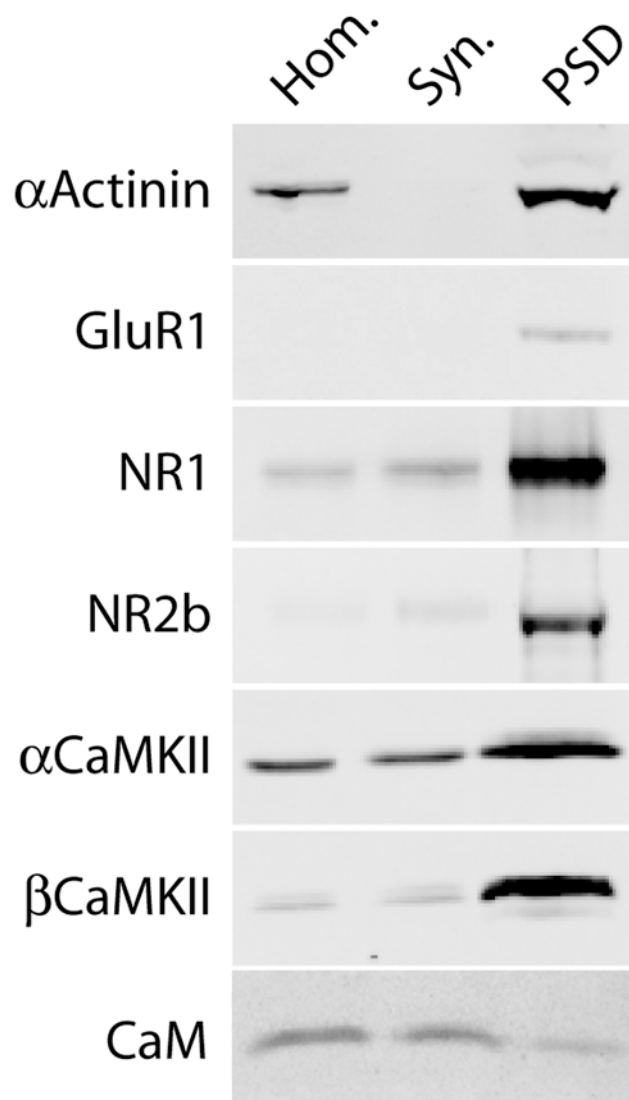


**Fig. 1.5** *Enrichment of proteins through PSD isolation process and specificity of antibodies.*

Western blots illustrating the enrichment of proteins through the PSD isolation process from brain homogenate (Hom.) to synaptosomes (Syn.) to the PSD fraction. All antibodies showed a single band at the expected molecular weight for the target protein. CaM is the only protein that did not show enrichment into the PSD fraction. 12 ug of total protein was loaded in each lane except in the case of CaM, which required 60 ug of total protein to produce detection.

contrast. This has to be the case, since the PSD fraction is derived directly from the synaptosomes.

### *Glutamate Receptors*

Because the majority of excitatory synapses in the CNS are glutamatergic synapses, three different glutamate receptor subunits were probed in PSD fractions by Western blot. NR1 and NR2b were chosen because they both are known to interact with CaMKII through their C-terminal tails (Gardoni et al., 1998; Leonard et al., 1999), making them prime targets for recruitment of CaMKII into the PSD. On top of this, NR1 is the critical pore-forming subunit present in all functional NMDA receptors so it acts as a marker for functional receptors (Cull-Candy et al., 2001). It is well documented that the NR2b subunit has high affinity for CaMKII (Gardoni et al., 1998; Leonard et al., 1999), and is likely the primary interaction that drives NMDA-dependent translocation of CaMKII from the cytosol to the PSD. Because NMDA receptors play such a critical role in synaptic signaling and plasticity it is not surprising that both NR1 and NR2b showed sequential enrichment throughout the PSD isolation process. The glutamate receptor subunit GluR1 also showed enrichment in the PSD fraction, despite the fast recycling kinetics (Bredt and Nicoll, 2003; Ehlers, 2000; Malinow and Malenka, 2002) associated with the receptor. At the protein concentration loaded on these gels, it was not possible to detect GluR1 in the homogenate or the synaptosomal fraction.

### *Signaling Molecules*

CaMKII is a well known component of the PSD (Kennedy et al., 1983; Walikonis et al., 2000). Historically, the  $\alpha$  isoform of CaMKII is the most well studied as a PSD component, but it is clear from the blots that  $\beta$ CaMKII is just as, if not more, enriched in the PSD, relative to the homogenate and synaptosomal fraction. There is very little in the literature to support a major role for  $\beta$ CaMKII within the PSD, however, it is not completely unexpected since CaMKII holoenzymes in the brain are largely a combination of  $\alpha$ - and  $\beta$  subunits (Bennett et

al., 1983; Miller and Kennedy, 1985; Vallano, 1989). The large enrichment of  $\beta$ CaMKII is interesting when thinking about the differences between the two isoforms and what their individual roles might be within the PSD and this is discussed in detail in the Discussion section.

CaM, the calcium sensing molecule responsible for the activation of CaMKII, was the only molecule among those studied that did not enrich in the PSD fraction with respect to the homogenate and synaptosomal fraction. This was not entirely unexpected as CaM is a ubiquitous protein that shows a diffuse staining pattern in immunocytochemical studies. In fact, with the antibody used, in order to increase the signal strength enough to see a band in the PSD fraction, the lanes were loaded with 60  $\mu$ g of total protein. Also, in order for CaM to run at the expected molecular weight (~17 kDa), 10 mM EDTA was needed in the sample running buffer as well as the SDS gel.

## **Chapter 2: PSDs Isolated at Different Developmental Time Points**

While previous work has confirmed that PSDs are present at synapses early in development (as early as E19), all of the available data is in the form of thin sections of brain tissue (Itarat and Jones, 1992). This limits evaluation of the PSD structure and the distribution of its components as it provides only cross-sections of the organelle. Presumably morphological differences exist between PSDs at different points through development, because their composition is known to change in a developmental and activity dependent fashion (Bresler et al., 2004; Ehlers, 2003; Petralia et al., 2005). However, no study has yet addressed this issue directly. Here, isolated PSDs were used to study the protein composition and structure of whole organelles.

The four developmental time points were chosen to highlight specific milestones in development. E19 is the earliest time point and it was chosen because this is the earliest time point that could be found in the literature documenting the presence of PSDs in cortex (Itarat and Jones, 1992). It is also interesting because the rats are prenatal and their PSDs should represent a structure that has been altered by external stimuli as little as possible. P2 was chosen as an early postnatal time point in order to investigate changes initiated early after birth. They are also the only early developmental PSDs isolated and studied previously (Petralia et al., 2005), although they were not examined under the microscope. P21 is an early adolescent time point and by this time the rat's ear canals and eyes have opened (~P14) and the cortex has been exposed to various external stimuli. Motor skills are well developed and the number of synaptic connections in the cortex is at a developmental high point (Markus and Petit, 1987). By P60 the sharp decline in the number of synapses that begins around P30 has slowed considerably, and the majority of synaptic pruning has presumably taken place. P60 PSDs have been isolated and are well described in previous literature. It represents an early adult time point that marks a logical final point for this study.

I chose to study changes in PSDs during development for two main reasons. One, development provides a glimpse into the natural progression of biological events. Other than time, no specific factor is systematically controlled and changes observed should be the product of natural consequence. Two, development is plasticity. I am interested in structural plasticity of synapses and how it relates to memory, but tracking activity induced changes at the ultrastructural level is not a simple task. Therefore studying developmental plasticity (which includes activity-dependent changes) seemed like a natural choice as a first step.

### **Protein Profiles of PSDs Isolated from Rat Forebrain at P60, P21, P2 and E19**

Because of the low protein yield of the PSD preparations from early developmental time points (P2 and E19) silver staining was used to compare the protein profiles of PSDs from the four time points (Fig. 2.1). Silver staining is 20-30 times more sensitive than Coomassie staining so only one microgram of total protein was needed for each lane. At first inspection, the gel can be split into two groups based on the profiles of the separated PSD proteins, and that these groups are related to the developmental age of the animals. One group is made up of the two latest time points (P60 and P21) and the other is made up of the two earliest time points (P2 and E19). As mentioned, at first glance the profile of PSDs within each group looks very similar, but there are obvious differences in some of the major bands that are present. Boxes in Fig. 1.6 represent major bands that are shared within the late and early groups of PSDs, but are absent or only minor bands in the other group. Although there are some major differences in the profiles of the late and early groups they also share many similar bands that appear in similar abundance. These bands are indicated by arrowheads along the right side of the gel shown.

Protein bands in SDS-PAGE separated PSD fractions have provided some of the earliest insight to the composition of the PSD. While the protein profiles vary slightly from lab to lab there are a handful of proteins bands that are consistently present, and these can be seen in the

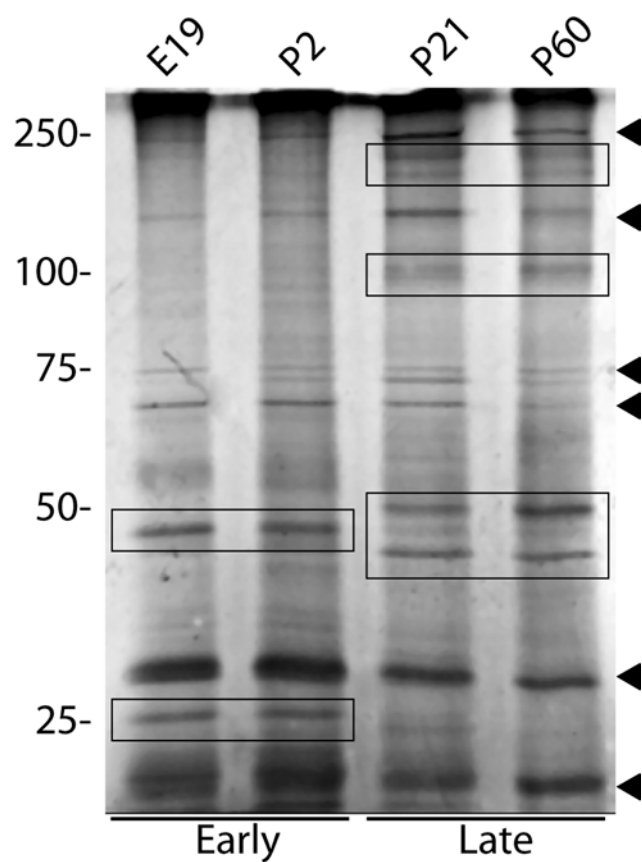


**Fig. 2.1** Comparison of Protein Profiles of PSDs Isolated at E19, P2, P21 and P60.

silver staining of P60 PSDs in Fig. 2.1. These bands can be seen at approximately 180 (spectrin), 150 (NR2b), 100 (PSD-95 and  $\alpha$ -actinin), 75 (synapsin 1A/1B), 73, 70 (Neurofilament L), 51 (CaMKII), 40 ( $\beta$ -actin and homer), 30 and 17 kDa (Walikonis et al., 2000). The band at 51 kDa is certainly the most well studied and it is well documented to be composed mostly of the  $\alpha$  isoform of CamKII (Carlin et al., 1981; Kennedy et al., 1983). There is also evidence that this band is composed partially of the protein neurofilament, which could be a component of the core structure of the PSD. However, the 51 kDa band is not apparent in the early time points suggesting it is not a major component early in development. There is a band at ~100 kDa that is visible at P21 and P60, which has been proposed to be  $\alpha$ -actinin. This is certainly possible considering the presence of immuno-gold labeling for  $\alpha$ -actinin (seen in Fig. 2.13). Like the 51 kDa band, this one is also not apparent in the early time points. This does not mean that it is not a component, but it would be a minor component compared to the other bands seen early in development. There are two bands (~45 and 25 kDa) that are major bands in early time points and not visible or faintly visible by the late time points. Without biochemical evidence for what these bands are composed of it is difficult to speculate about what these may be, but the molecular weight of the cytoskeletal protein actin is 43 kDa and it would make sense if it was involved in the early stages of PSD formation. Despite not knowing the identity of these proteins, it is still interesting because this is the first time protein profiles of PSDs from different aged animals have been compared. The fact that there are major differences suggests that different components are important to the PSD at different stages of development, and the presence of shared components suggests that specific molecules are preserved in similar proportions throughout the animal's life.

### **Structure of PSDs during Development of Rat Brain**

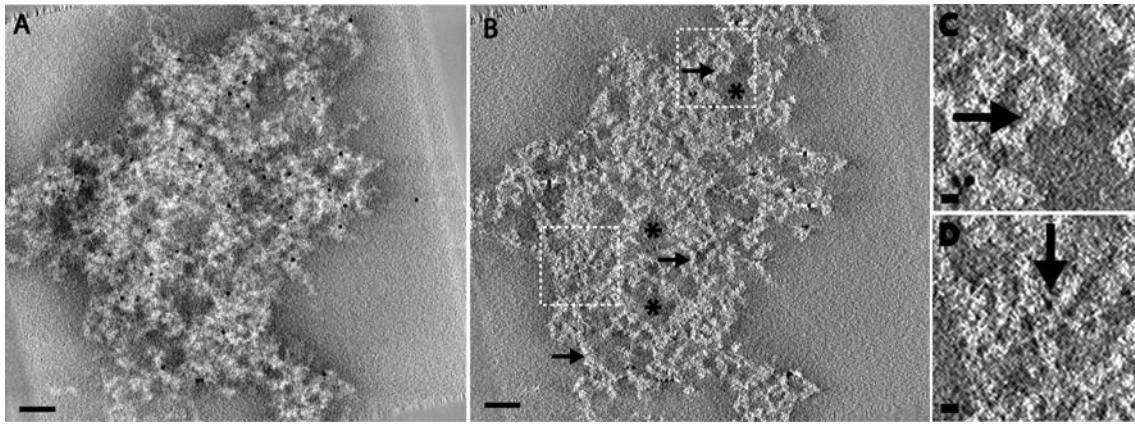
*Electron Tomography of PSDs Isolated from Forebrain at E19, P2, P21 and P60 in Negative Stain*

To study the three-dimensional structure of PSDs isolated at each developmental time point electron tomography was implemented. Tomography is especially well suited for studying PSD structure, because it allows for the three-dimensional reconstruction of unique biological samples (unique, meaning that no PSD is exactly the same as another). Because of this lack of apparent regularity one cannot use image processing methodology that relies on the alignment and averaging of many images in order to render high-resolution structural information. To perform electron tomography, PSDs were first located in the EM. Once, the stage of the microscope was tilted  $\pm 60^\circ$  while a projection image was collected every  $2^\circ$  under low electron dose conditions. Image tilt-series were collected for multiple PSDs from each developmental time point, and tomographic reconstructions were calculated for each tilt-series using the IMOD software package developed at the University of Colorado in Boulder (<http://bio3d.colorado.edu/imod/>). The process is described in detail in the methods section, but briefly, each of the images is first aligned and then spatial relationships across the images due to the tilting of the stage are tracked by the software using high-contrast gold fiducial markers deposited on the sample during the negative staining process. With these spatial relationships accounted for and the angular parameters for each image known, a three-dimensional reconstruction is calculated via a weighted back-projection algorithm. With tomographic reconstructions of PSDs isolated from all four developmental time points a three-dimensional representation of the protein disposition within the PSDs was available for thorough observation. The results of these experiments are described below.

There have been numerous studies examining the morphology of PSDs isolated from forebrain of young adult rat and other species (Blomberg et al., 1977; Cohen et al., 1977; Cotman et al., 1974; DeGiorgis et al., 2006; Petersen et al., 2003). Based on their differential protein profiles it was expected that PSDs from different times during development would

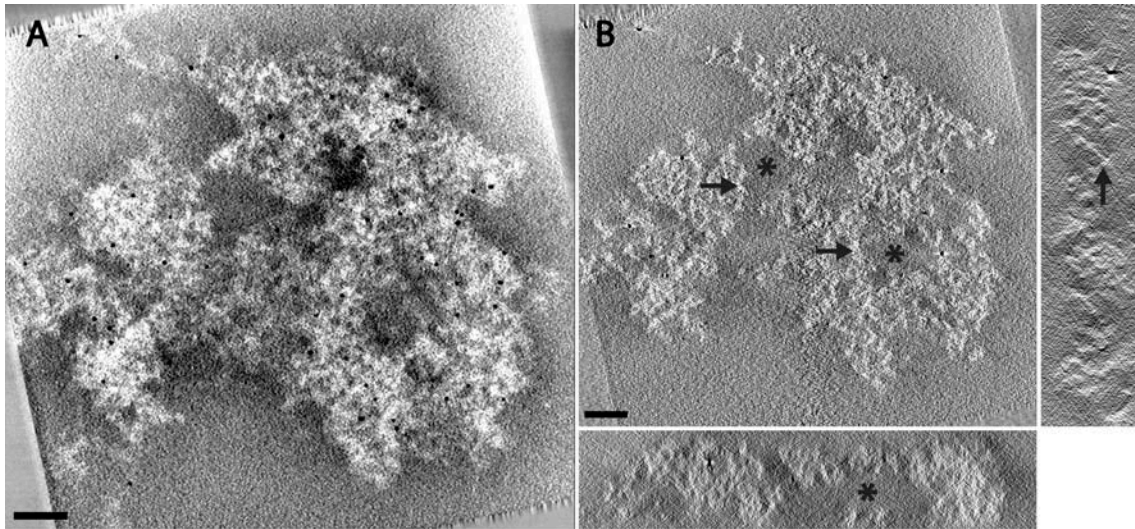


exhibit distinct morphologies. In order to compare the morphology of isolated PSDs from each time point tomographic reconstructions were produced from negative stained samples. Tomographic reconstructions of PSDs isolated at E19 can be seen in Figs. 2.2-2.4. Fig. 2.2A is a display of the entire tomographic reconstruction as seen viewed parallel to the Z-axis. This means that all of the data available in the reconstructed volume is displayed as a normal 2D projection image typical for how a PSD would appear in the microscope. In Fig. 2.2B, a 10 nm cross-section of the same PSD is shown. These two views have been contrasted to clearly illustrate the structural information gained via tomographic reconstruction, as well as to correlate the internal structure with its appearance in a full projection image. PSDs isolated at E19 displayed a relatively lacey appearance compared to those at the other three time points. There appears to be a significant amount of “empty” space (asterisks) distributed through the E19 structure, which was made primarily of rope-like strands of protein (horizontal arrows in Fig. 2.2B) intertwined to form a lattice structure. The lattice structure is evident in both the full projection image (panel A) and the 10 nm cross-section (panel B), but the individual strands are most easily distinguished in the cross-section. Panel C is a blow-up of the region bounded by the dashed box in the upper portion of panel B. It shows a closer view of the protein strand indicated by the arrow. At this higher zoom it is possible to see that the strands appear to be made up of smaller protein components. Panel D is a blow-up of the region bounded by the dashed box in the lower portion of panel B. It illustrates a region of the E19 PSD that is made of a mesh of small protein filaments. One of the filaments is indicated by the arrow. Fig. 2.3 and 2.4 show two more tomographic reconstructions of PSDs isolated at E19. As with Fig. 2.2, panel A shows full projections of the entire reconstruction and panel B shows 10 nm cross-sections through the PSD perpendicular to the Z-axis. In both cases, the general morphology of the PSD is the same as in Fig. 2.2, with a lacey structure made of rope-like strands of protein. In panel B of Figs. 2.3 and 2.4, there are two smaller panels along the bottom and right side that



**Fig. 2.2** *Tomographic reconstruction of a PSD isolated at E19.*

(A) Full projection image of the entire tomographic reconstruction at E19. (B) 10 nm cross-section through the center of the tomographic reconstruction shown in (A). Horizontal arrows indicate rope-like strands of protein that comprise the majority of the PSD structure. Asterisks indicate areas of empty space within the structure. Smaller portions of empty space are distributed through the majority of the structure between the strands of the lattice. (C) Blow-up of the region bounded by the dashed box in the upper portion of (B). The arrow indicates one of the strands of protein seen making up the PSD lattice. In this panel it is possible to see the smaller protein components that make up the larger strands of protein. (D) Blow-up of the region bounded by the dashed box in the lower portion of (B). The arrow points to a smaller filament that can be seen in the meshwork of protein. Gold balls in the images are fiducial markers used to align images during the tomographic reconstruction. Scale bars represent 100 nm in (A) and (B) and 20 nm in (C) and (D).



**Fig. 2.3** *Tomographic reconstruction of a PSD isolated at E19.*

(A) Full projection image of the entire tomographic reconstruction at E19. (B) 10 nm cross-section through the center of the tomographic reconstruction shown in (A). Horizontal arrows indicate rope-like strands of protein that comprise the majority of the PSD structure. Asterisks indicate large areas of empty space within the structure. Smaller portions of empty space are distributed through the majority of the structure between the strands of the lattice. Smaller panels below and to the right of panel B are 10 nm cross-sections cut parallel to the Z-axis along the X- and Y-axis, respectively. The arrow points to a protein strand seen traveling through the Z dimension of the PSD and the asterisk denotes a pocket of empty space as in panel B. Scale bars represent 100 nm.

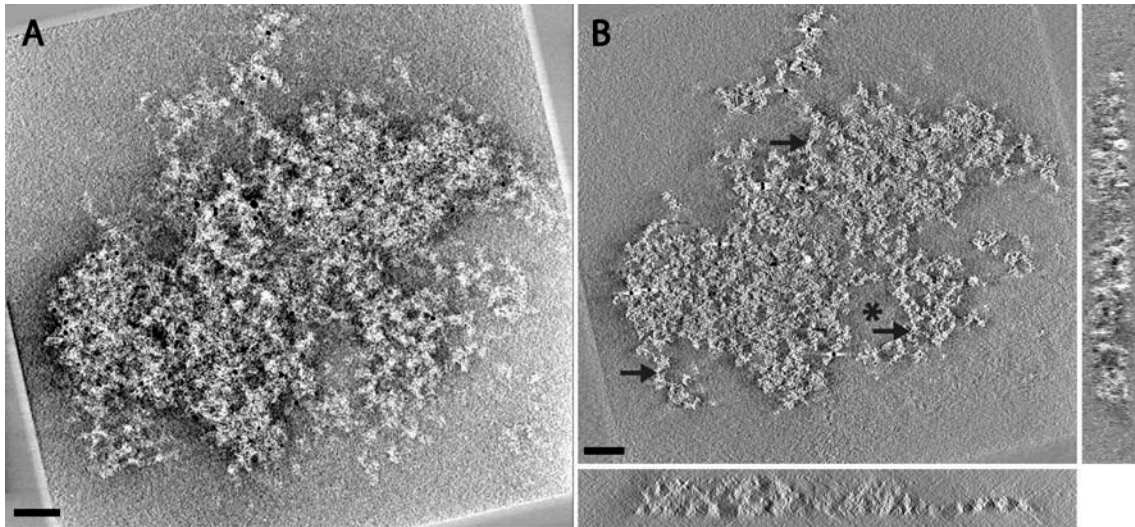


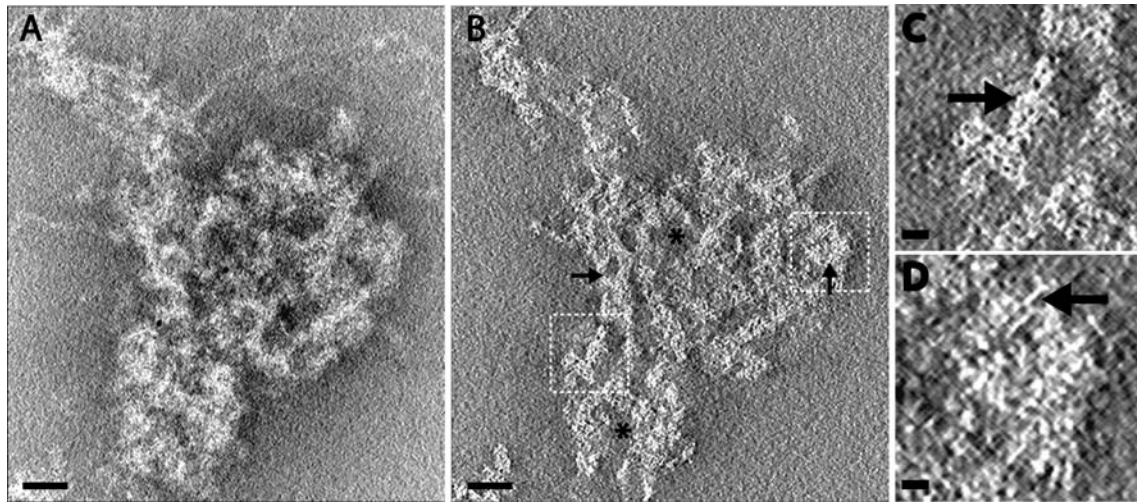
**Fig. 2.4** *Tomographic reconstruction of a PSD isolated at E19.*

(A) Full projection image of the entire tomographic reconstruction at E19. (B) 10 nm cross-section through the center of the tomographic reconstruction shown in (A). Horizontal arrows indicate rope-like strands of protein that comprise the majority of the PSD structure. Asterisks indicate large areas of empty space within the structure. Smaller portions of empty space are distributed through the majority of the structure between the strands of the lattice. Smaller panels below and to the right of panel B are 10 nm cross-sections cut parallel to the Z-axis along the X- and Y-axis, respectively. Scale bars represent 100 nm.

show 10 nm cross-sections cut parallel to the Z-axis along the X- and Y-axis, respectively. The asterisks indicate large empty space within the PSD and the vertical arrow points to a portion of the protein lattice that can be seen running parallel to the Z-axis.

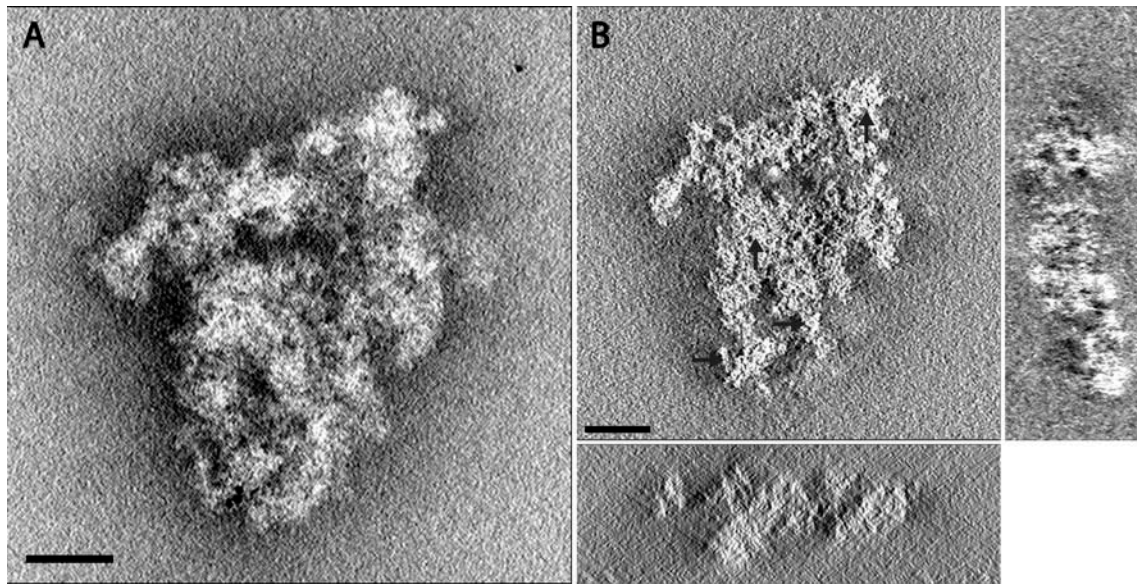
Fig. 2.5 shows a typical PSD isolated at P2. The overall appearance was different from the E19 PSD in that the strands of protein were not such a prominent feature (especially in the full projection image). However, they are still visible in the 10 nm cross-section (horizontal arrow in panel B). Panel C is a blow-up of the region bound by the dashed box on the left of panel B. The arrow points to one of the rope-like strands of protein similar to the ones seen prominently in the E19 PSD. The lattice structure was less apparent at P2 as the PSD appeared more densely packed with protein, and there was less “empty” space visible in both the full projection and the 10 nm cross-section (asterisks). Despite the denser protein packing the P2 PSD was still mostly mesh-like compared to PSDs from P21 and P60. The lattice was visible, but studded with more regions of higher protein density (vertical arrows in panel B). Panel D is a blow-up of the dense region of protein in panel B. Filaments like those seen in the E19 PSD are visible in the patch of protein, indicated by the arrow. Fig. 2.6 and 2.7 show two more tomographic reconstructions of PSDs isolated at P2. As with Fig. 2.5, panel A shows full projections of the entire reconstruction and panels B shows 10 nm cross-sections through the PSD perpendicular to the Z-axis. In both cases, the general morphology of the PSD is the same as in Fig. 2.5; a mesh of protein with protein strands resembling those at E19. The denser regions of protein packing are indicated by the vertical arrows. In panel B of Figs. 2.6 and 2.7, there are two smaller panels along the bottom and right side that show 10 nm cross-sections cut parallel to the Z-axis along the X- and Y-axis, respectively.

Fig. 2.8 shows a typical PSD isolated at P21. PSDs isolated at P21 generally exhibited a denser protein packing although there are often perforations or pockets of low density (asterisks in panel B). The PSD in Fig. 2.8 displays a variety of morphological features that were



**Fig. 2.5** *Tomographic Reconstruction of PSD isolated at P2.*

(A) Full projection image of the entire tomographic reconstruction at P2. (B) 10 nm cross-section through the center of the tomographic reconstruction shown in (A). The protein is more densely packed than at E19, but similar strands of protein can still be seen (horizontal arrow). The PSD lattice is studded with more regions of densely packed protein as indicated by the vertical arrow. Large empty spaces are less abundant than at E19, but can still be seen (marked by the asterisk). (C) Blow-up of the region bounded by the dashed box on the left in (B). The arrow indicates one of the strands of protein seen making up the PSD lattice, and again, smaller protein components that make up the larger strands can be seen. (D) Blow-up of the region bounded by the dashed box on the right in (B). A dense region of protein packing can be seen, and the arrow points to a smaller filament like the ones seen in Fig. 3D. Gold balls in the images are fiducial markers used to align images during the tomographic reconstruction. Scale bars represent 100 nm in (A) and (B) and 20 nm in (C) and (D).



**Fig. 2.6** *Tomographic Reconstruction of PSD isolated at P2.*

(A) Full projection image of the entire tomographic reconstruction at P2. (B) 10 nm cross-section through the center of the tomographic reconstruction shown in (A). The protein is more densely packed than at E19, but similar strands of protein can still be seen (horizontal arrows). The PSD lattice is studded with more regions of densely packed protein as indicated by the vertical arrow. Large empty spaces are less abundant than at E19, but can still be seen (marked by the asterisk). Smaller portions of empty space are distributed through the majority of the structure between the strands of the lattice. Smaller panels below and to the right of panel B are 10nm cross-sections cut parallel to the Z-axis along the X- and Y-axis, respectively. Scale bars represent 100 nm.

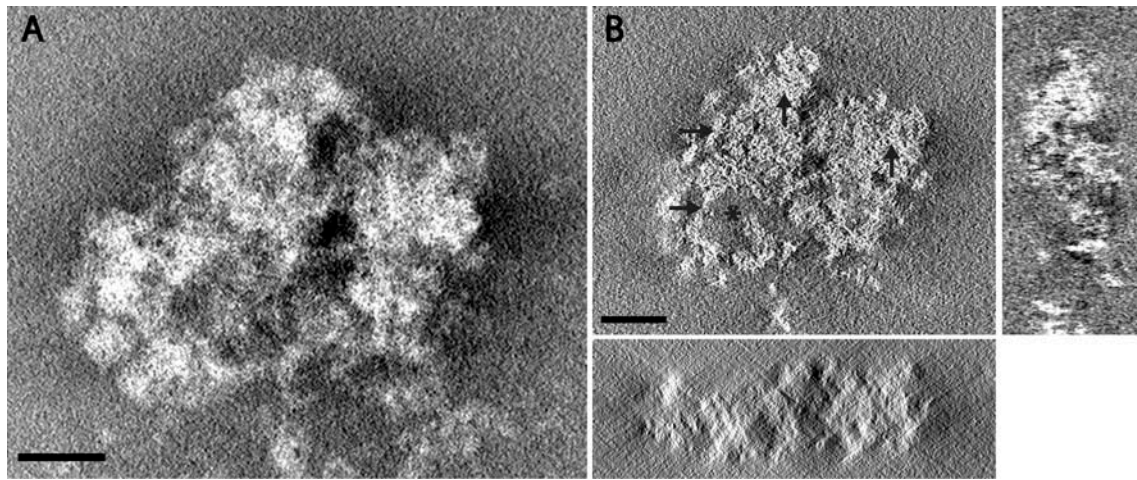


**Fig. 2.7** *Tomographic Reconstruction of PSD isolated at P2.*

(A) Full projection image of the entire tomographic reconstruction at P2. (B) 10 nm cross-section through the center of the tomographic reconstruction shown in (A). The protein is more densely packed than at E19, but similar strands of protein can still be seen (horizontal arrows). The PSD lattice is studded with more regions of densely packed protein as indicated by the vertical arrow. Large empty spaces are less abundant than at E19, but can still be seen (marked by the asterisk). Smaller portions of empty space are distributed through the majority of the structure between the strands of the lattice. Smaller panels below and to the right of panel B are 10nm cross-sections cut parallel to the Z-axis along the X- and Y-axis, respectively. Scale bars represent 100 nm.



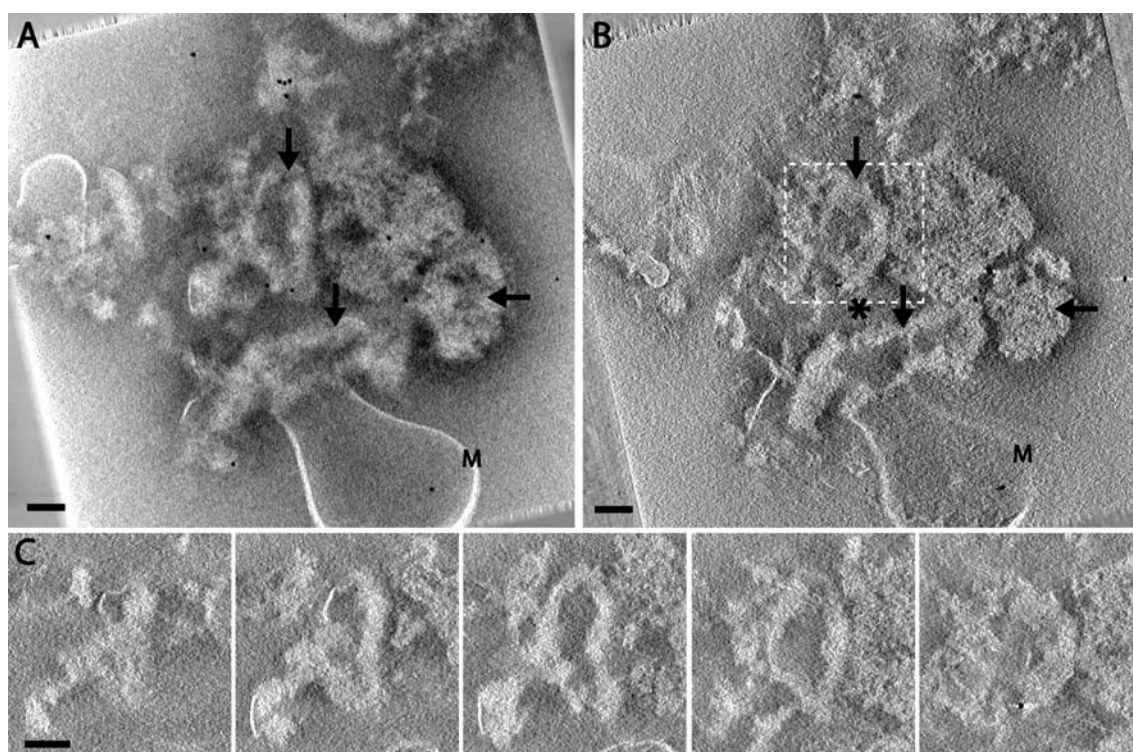


**Fig. 2.8** *Tomographic Reconstruction of PSD isolated at P21.*

(A) Full projection image of the entire tomographic reconstruction at P21. (B) 10 nm cross-section through the center of the tomographic reconstruction shown in (A). The vertical arrows in (A) point to protein ring structures that are commonly seen by P21 and the vertical arrows in (B) point to the same structures in the cross-section. The horizontal arrows indicate a large dense protein structure that is common by P21. The asterisk in (B) indicates an empty space that perforates the PSD and the “M” indicates a piece of membrane that is still attached. (C) A montage of slices moving down through the Z-axis of the region bounded by the dashed box in (B). Moving from left to right the panels show that the protein rings seen by P21 are actually fully enclosed. Gold balls in the images are fiducial markers used to align images during the tomographic reconstruction. Scale bars represent 100 nm.

common to PSDs isolated at this developmental time point, including protein rings (vertical arrows pointing downward in panels A and B) and large solid regions of densely packed protein (horizontal arrows). The protein rings can be seen in the full projection, but their hollow center is more evident in the tomographic cross-section. This is due to the fact that, while they look like rings in cross-section, they are actually fully enclosed by protein in all three dimensions and the edges appear densest from this angle. Fig. 2.8 C shows a series of cross-sections through the protein ring bound by the dashed box in panel B. Moving from left to right through the panels in Fig. 2.8C the cross-sections move down through the Z-axis of the tomogram, showing that the protein ring is enclosed on the top and bottom and hollow in the middle. Hence, while they look like rings in projection they are actually roughly elliptical. Large areas of densely packed protein were more common by P21 suggesting that large areas of the lattice seen routinely at E19 and P2 have been filled in by protein components recruited later in development. The letter “M” in Fig. 2.8 denotes pieces of membrane that were apparently not solubilized during the isolation process. These were common at P21 and P60, but were not seen at E19 and P2. It is not clear whether this is due to changes in the PSD that alter its interaction with the membrane or if it is a change in membrane composition later in development. Figs. 2.9 and 2.10 are two more examples of PSDs isolated at P21. Fig. 2.9 shows a similar morphology to that in Fig. 2.8, with densely packed regions of protein (horizontal arrow pointing left) along with rings of proteins (vertical arrows). The horizontal arrow pointing right indicates a patch of lattice-like strands of protein like those seen at E19 and P2. Fig. 2.10 shows a third PSD that appears to be made mostly of densely packed protein (vertical arrows) similar to the smaller regions of dense protein seen in the other PSDs. While it does appear to be made of discreet islands of dense proteins they are all connected at one region or another. While PSDs like the one seen in Fig. 2.10 do exist, they are less common than the ones seen in Figs. 2.8 and 2.9, which display the various types of protein arrangement.

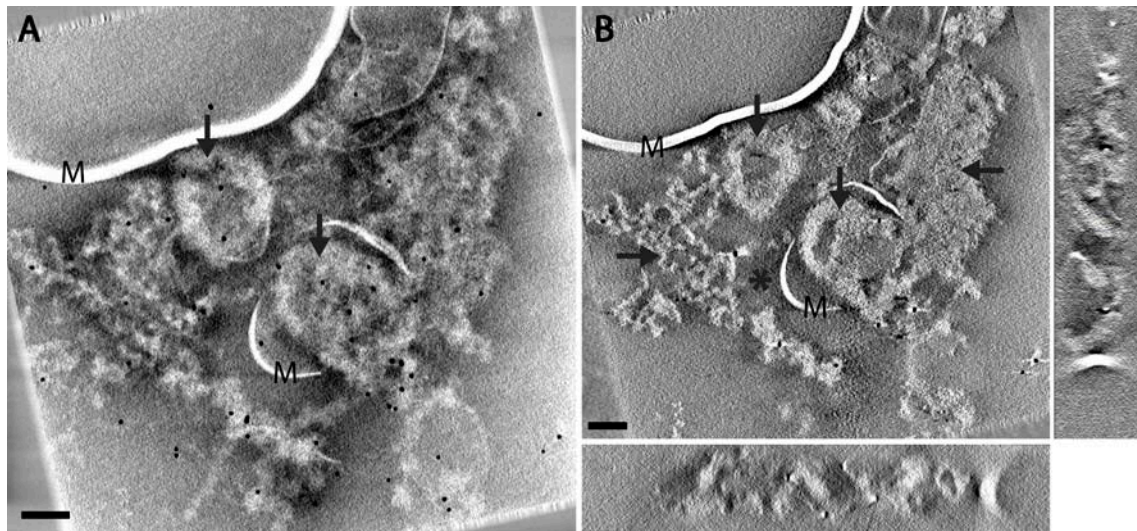


**Fig. 2.9** *Tomographic Reconstruction of PSD isolated at P21.*

(A) Full projection image of the entire tomographic reconstruction at P21. (B) 10 nm cross-section through the center of the tomographic reconstruction shown in (A). The vertical arrows in (A) point to protein ring structures that are commonly seen by P21 and the vertical arrows in (B) point to the same structures in the cross-section. The horizontal arrows indicate a large dense protein structure that is common by P21. The asterisk in (B) indicates an empty space that perforates the PSD and the “M” indicates a piece of membrane that is still attached. Smaller panels below and to the right of panel B are 10nm cross-sections cut parallel to the Z-axis along the X- and Y-axis, respectively. Scale bars represent 100 nm.

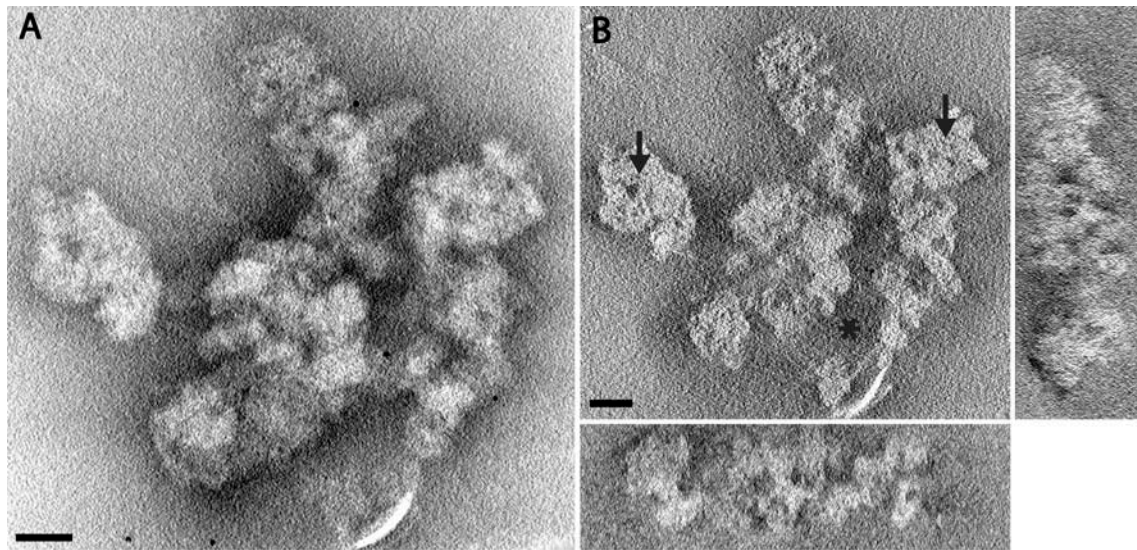


**Fig. 2.10** *Tomographic Reconstruction of PSD isolated at P21.*

(A) Full projection image of the entire tomographic reconstruction at P21. (B) 10 nm cross-section through the center of the tomographic reconstruction shown in (A). The vertical arrows in (A) point to large dense regions of protein that is common by P21. The asterisk in (B) indicates an empty space that perforates the PSD. Smaller panels below and to the right of panel B are 10nm cross-sections cut parallel to the Z-axis along the X- and Y-axis, respectively. Scale bars represent 100 nm.

In panel B of Figs. 2.9 and 2.10, there are two smaller panels along the bottom and right side that show 10 nm cross-sections cut parallel to the Z-axis along the X- and Y-axis, respectively. Fig. 2.11 shows a PSD isolated at P60. PSDs from this developmental time point were not visually distinguishable from those isolated at P21. They exhibit the same variety of protein structures such as protein rings (downward facing vertical arrow) and densely packed regions of protein (horizontal arrow). Vertical arrows pointing upward in panel B point to strands of protein that resemble those seen more routinely in PSDs isolated at E19 and P2, suggesting that the lattice structure seen at these early developmental time points remains at P21 and P60, but is obscured by additional protein packing. In panel B there are two smaller panels along the bottom and right side that show 10 nm cross-sections cut parallel to the Z-axis along the X- and Y-axis, respectively.

### **Size Comparison of PSDs Isolated from Forebrain at E19, P2, P21 and P60**

The dimensions of the PSDs in our preparations ranged from 0.2 to 1.2  $\mu\text{m}$  when measured across their widest points, which is typical of that reported previously (Blomberg et al., 1977; Cohen et al., 1977; Cotman et al., 1974; DeGiorgis et al., 2006; Petersen et al., 2003). Due to their highly variable shape, measuring their area ended up being a more useful assessment on which to quantify and compare their relative sizes over the four developmental time points. Fig. 2.12 shows histograms of PSD surface area for each of the four developmental time points. Mean surface areas were  $0.195 \pm 0.009 \mu\text{m}^2$  at E19,  $0.313 \pm 0.017 \mu\text{m}^2$  at P2,  $0.259 \pm 0.017 \mu\text{m}^2$  at P21 and  $0.251 \pm 0.012 \mu\text{m}^2$  (surface area  $\pm$  SEM) at P60. All four time points show a peak around  $0.15 \mu\text{m}^2$ . The distribution of PSD sizes for all time points can be loosely described as a long-tailed marginal distribution. Despite some small differences seen in the histograms they all share a peak PSD surface area of about  $1.5 \mu\text{m}^2$ , meaning that the PSDs do not drastically change sizes through development. This suggests that PSDs do not start out

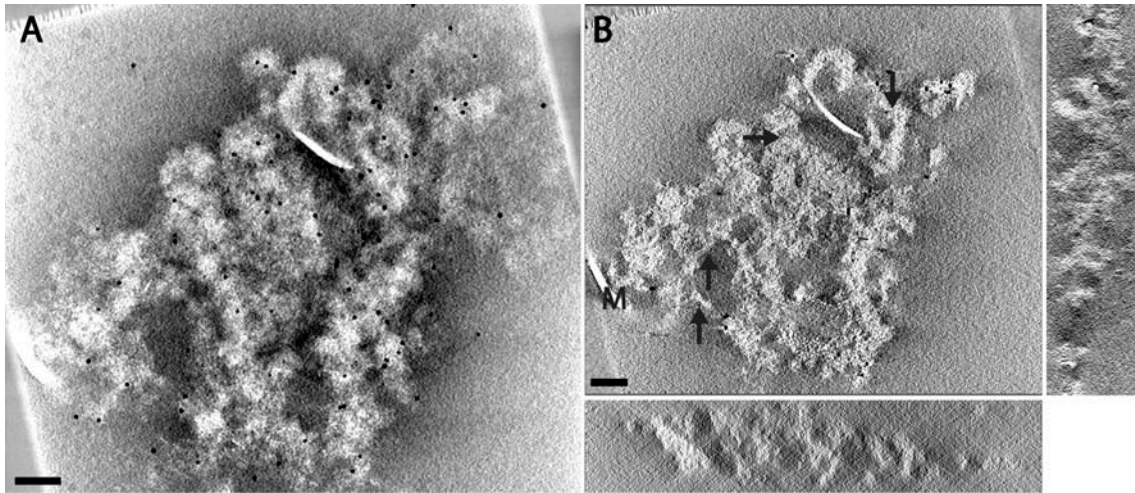


**Fig. 2.11** *Tomographic Reconstructions of PSDs isolated at P60.*

(A) Full projection image of the entire tomographic reconstruction at P60. (B) 10 nm cross-section through the center of the tomographic reconstruction shown in (A). The horizontal arrows point to a large dense protein structure similar to the one seen at P21. The downward-facing vertical arrows point to a protein ring structure. The upward-facing arrows in (D) point to protein strands that are similar to those seen at E19 and P2. Smaller panels below and to the right of panel B are 10nm cross-sections cut parallel to the Z-axis along the X- and Y-axis, respectively. Scale bars represent 100 nm.

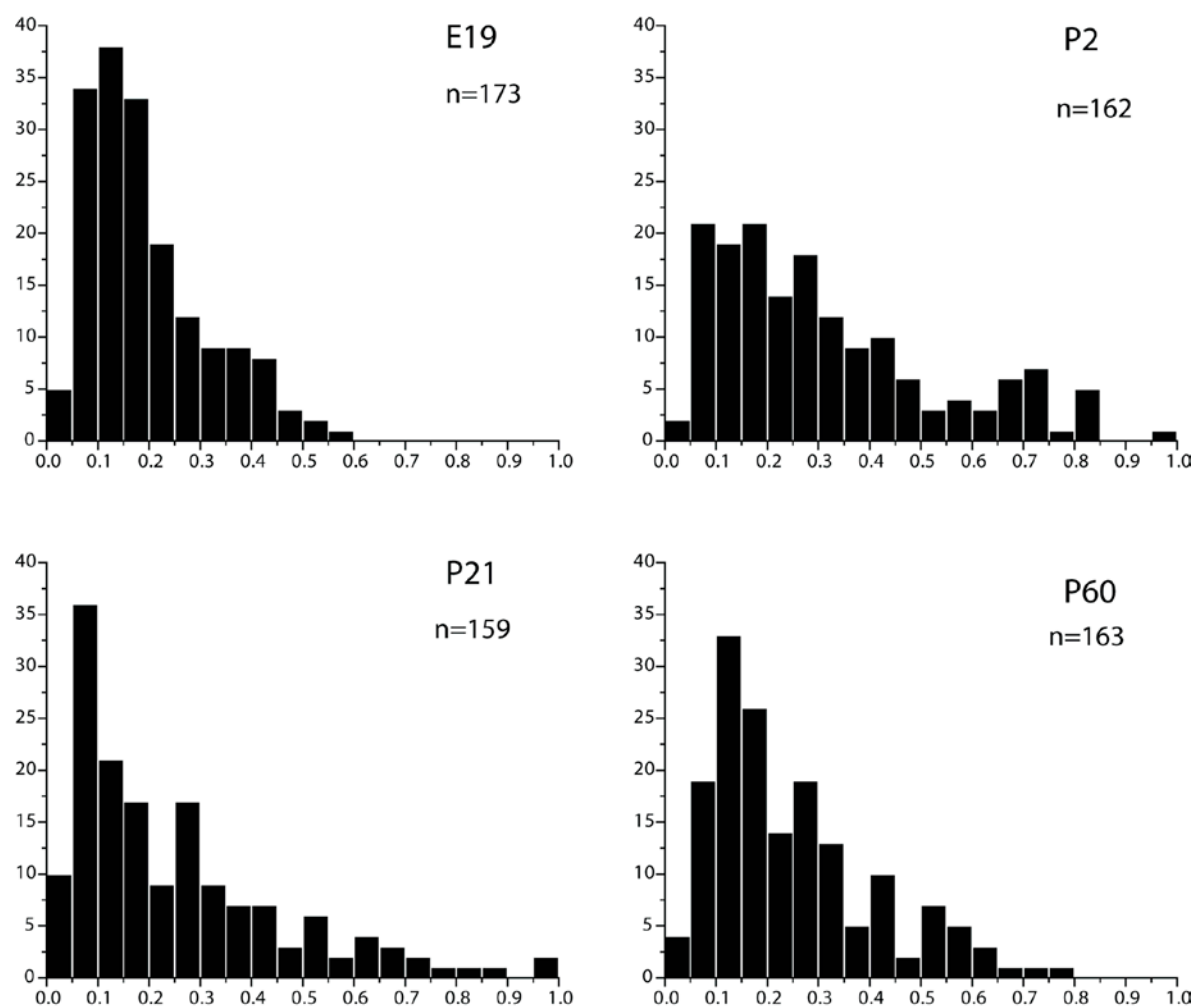


**Fig. 2.12** Histograms of PSD surface area at E19, P2, P21 and P60.

Histograms depicting the distribution of surface areas of PSDs isolated at E19, P2, P21 and P60. Comparison of the four histograms shows that all four developmental time points share a peak around 0.15  $\mu\text{m}^2$  and similar size ranges.



small and grow laterally, but more likely begin with a more typical size and then fill out in a laminar fashion over time.

### **Protein composition of PSDs isolated at E19, P2, P21 and P60**

Because of the obvious differentiation in the silver stained profiles of PSDs isolated at early and late development (Fig. 2.1) and the changes in morphology at the ultrastructural level, it is logical to think there must be variations in protein composition to account for these differences. While the protein composition of adult PSDs has been studied extensively by western blot, immuno-fluorescence, immuno-gold labeling and mass spectroscopy (Bresler et al., 2001; Bresler et al., 2004; Chen et al., 2008; DeGiorgis et al., 2006; Petersen et al., 2003; Petralia et al., 2005; Walikonis et al., 2000), there is only a limited amount of data investigating PSDs at other stages of development. To study the differences in protein composition through development, immuno-gold labeling and analysis via electron microscopy was used. This strategy was chosen because it offers two major advantages over other methodologies. First, the high resolving power of electron microscopy allows for the identification of individual organelles within the PSD fraction, which means that labeling directly associated with PSD complexes can be studied while protein that is associated with contaminants (see Fig. 1.2) is ignored. This is important since isolated PSD preparations are merely enriched in PSDs, and methods that quantify total protein levels in the PSD fraction reflect that from all sources within the fraction. This also means that comparison of individual PSDs is possible so that variability at the single PSD level can be assessed. Second, the high electron density of the conjugated gold particles that allows for localization in the electron microscope not only provides information about the abundance of molecules within individual PSDs, but also about the spatial location of the molecules within the complex. This way the distribution of molecules through the complex can be studied (this is explored in the appendix), and knowledge about the structural arrangement of molecules within the PSD can be gained.



Because of their roles in regulating various aspects of synaptic signaling and structure, a subset of proteins in PSDs were chosen to study their abundance in PSDs isolated from E19, P2, P21 and P60. As noted before, the proteins were chosen to represent different functional categories of molecules (i.e., scaffolding molecules, neurotransmitter receptors and signaling molecules) within the PSD. Labeling for each class of proteins is discussed below, but the general conclusion is that there was a trend toward increased labeling densities through development for all of the molecules examined with the exception of CaM. However, the time course for the increase in labeling is varied for each molecule suggesting that not all molecules are recruited to the PSD with the same developmental kinetics. Also, some showed a peak in labeling density at intermediate time points and then decreased by P60. A summary of all the quantified data is presented in Table 2.1, and a detailed description of the results broken down by protein category is given in the following sections.

### *Scaffolding Molecules*

Of immediate interest is that not all components are present in PSDs isolated during the earliest stages of development in this study. For example, there is a near absence of the scaffolding molecule PSD-95 in PSDs isolated at E19 and P2 (Fig. 2.13). PSD-95 is, however, an abundant molecule in PSDs isolated from adult brains (Fig. 2.13), and has long served as a marker for the presence of PSDs in neuronal tissue and cultures. Because of its history with respect to the PSD, we chose PSD-95 as a starting point for our study and as a way to compare its abundance in our PSD preparations to what has been published previously (Petersen et al., 2003). In our preparations, PSD-95 labeling is very low (almost non-existent) in PSDs isolated early in development (0.2 gold/ $0.1\mu\text{m}^2$  at E19 and 1.1 gold/ $0.1\mu\text{m}^2$  at P2). In both cases roughly half of the PSDs did not show labeling above background indicating that many of the PSDs isolated at E19 and P2 do not contain significant amounts of PSD-95. For the actual number of PSDs labeled for each antibody see table 2.2. In this instance, each PSD that showed

	<b>Gold/0.1um<sup>2</sup> ± SEM</b>			
	<b>E19</b>	<b>P2</b>	<b>P21</b>	<b>P60</b>
<b>α-Actinin</b>	12 ± 1	32 ± 3	18 ± 2	46 ± 2
<b>αCaMKII</b>	3 ± 1	8 ± 1	28 ± 3	31 ± 3
<b>βCaMKII</b>	2 ± 0.5	9 ± 2	35 ± 5	27 ± 3
<b>CaM</b>	28 ± 4	15 ± 2	8 ± 2	6 ± 1
<b>GluR1</b>	1 ± 0.2	2 ± 0.3	3 ± 1	3 ± 1
<b>NR1</b>	5 ± 1	4 ± 1	22 ± 3	9 ± 1
<b>NR2b</b>	7 ± 1	9 ± 1	24 ± 2	12 ± 2
<b>PSD95</b>	0.2 ± 0.06	1 ± 0.5	38 ± 4	27 ± 3
	<b>Gold/PSD ± SEM</b>			
	<b>E19</b>	<b>P2</b>	<b>P21</b>	<b>P60</b>
<b>α-Actinin</b>	17 ± 2	50 ± 10	21 ± 3	119 ± 13
<b>αCaMKII</b>	10 ± 2	39 ± 8	49 ± 8	105 ± 16
<b>βCaMKII</b>	7 ± 1	56 ± 13	35 ± 6	76 ± 10
<b>CaM</b>	31 ± 6	32 ± 6	6 ± 1	14 ± 2
<b>GluR1</b>	3 ± 0.5	9 ± 2	6 ± 1	14 ± 3
<b>NR1</b>	12 ± 2	28 ± 3	21 ± 3	63 ± 10
<b>NR2b</b>	19 ± 3	33 ± 7	22 ± 3	46 ± 7
<b>PSD95</b>	2 ± 0.5	8 ± 3	56 ± 9	96 ± 16

**Table 2.1** *Summary of immuno-gold labeling results*

	PSDs Showing Labeling			
	<b>E19</b>	<b>P2</b>	<b>P21</b>	<b>P60</b>
<b><math>\alpha</math>-actinin</b>	22 of 22	16 of 16	17 of 18	17 of 17
<b><math>\alpha</math>CaMKII</b>	15 of 18	20 of 20	19 of 19	19 of 19
<b><math>\beta</math>CaMKII</b>	17 of 20	19 of 20	19 of 20	20 of 20
<b>CaM</b>	19 of 19	18 of 18	19 of 22	18 of 19
<b>GluR1</b>	17 of 20	14 of 17	12 of 18	15 of 18
<b>NR1</b>	17 of 18	16 of 17	17 of 18	21 of 21
<b>NR2b</b>	16 of 16	22 of 23	19 of 19	23 of 23
<b>PSD95</b>	7 of 19	10 of 18	14 of 14	17 of 18

**Table 2.2** *Number of individual PSDs that showed immuno-gold labeling above background.*

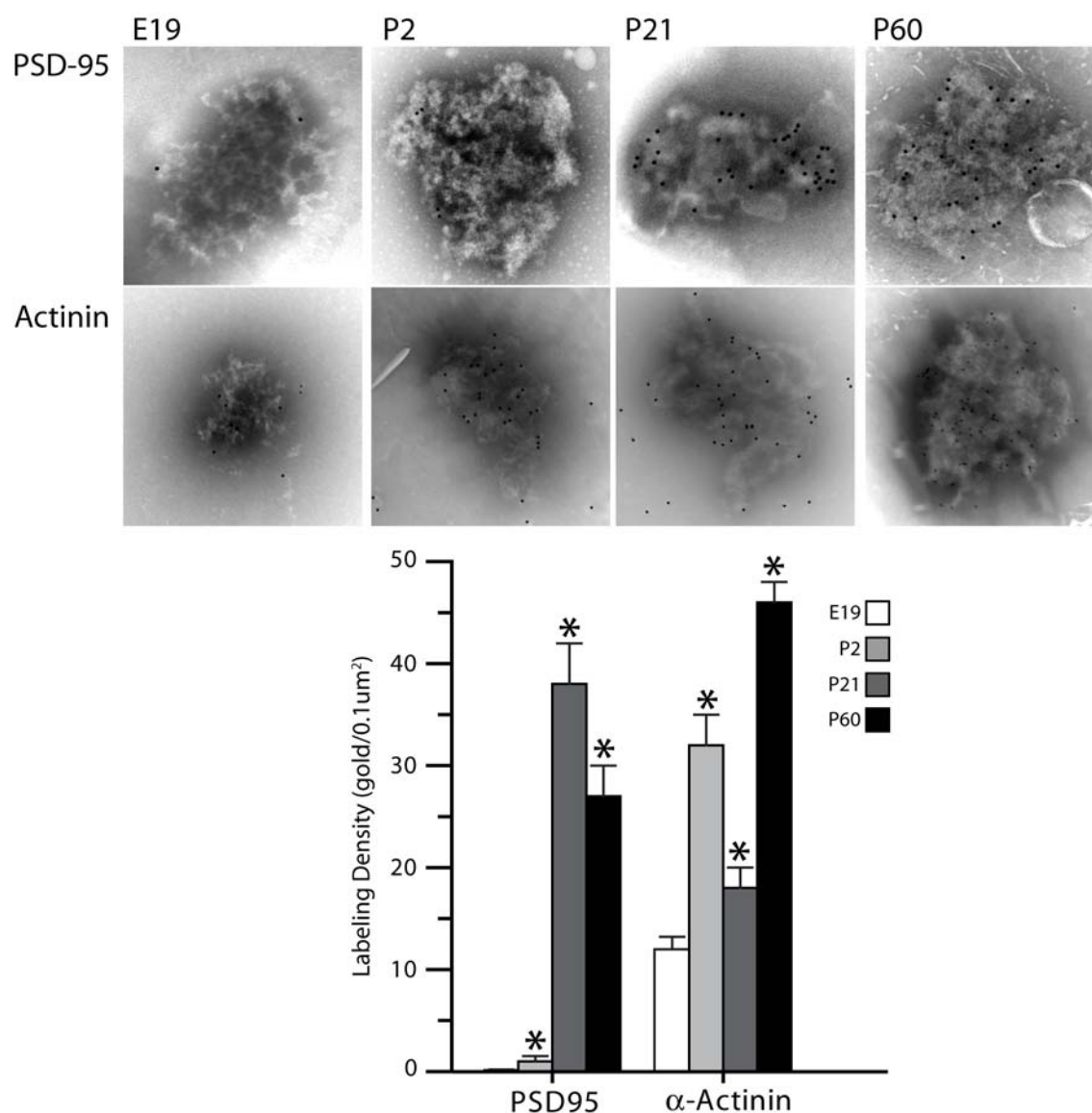


**Fig. 2.13** Immuno-gold labeling of PSD-95 and Actinin at E19, P2, P21 and P60.

Electron micrographs of representative PSDs isolated from E19, P2, P21 and P60 immuno-gold labeled for PSD-95 and  $\alpha$ -actinin. Average labeling density for each antibody at each developmental time point is shown in the graph. Asterisks indicate a significant change from the previous time point at a p value < 0.05.

no labeling above background was averaged into the group with a labeling density of zero. However, if only the PSDs that showed labeling are used to calculate a mean labeling density the values increase only slightly to 0.4 gold/ $0.1\mu\text{m}^2$  at E19 and 2.5 gold/ $0.1\mu\text{m}^2$  at P2, which is still strikingly low. While this result was not entirely unexpected (Petrulia et al (2005) showed there was little PSD-95 present in brain homogenates by Western blot at P2) it was still surprising to see such minimal staining in E19 and P2 PSDs. With its reputation as a major PSD scaffolding molecule one might expect it to be more intimately involved in early stages of the organelle's development. While PSD-95 showed very little labeling in PSDs isolated at E19 and P2, it is important to note that PSD-95 is one member of a larger family of related proteins, such as chapsyn 110, SAP-102 or SAP-97. Presumably one or more of these other family members likely play an analogous scaffolding role at earlier developmental time points (Petrulia et al., 2005) as PSD-95 does in adult PSDs.

By P21, labeling for PSD-95 increased to 38.5 gold/ $0.1\mu\text{m}^2$ , the highest mean density for PSD-95 across all four time points, which decreased to 27.5 gold/ $0.1\mu\text{m}^2$  at P60. In this case, each change in density from one time point to the next was shown to be significant ( $P < 0.05$ ). Of all PSDs analyzed across both P21 and P60 only one did not show labeling above background, suggesting that by P21 nearly all PSDs have incorporated PSD-95 as a stable scaffolding component. It is worth noting that the labeling density we observed in adult PSDs is consistent with that reported earlier using a similar labeling protocol (Petersen et al., 2003). Interestingly, the actin binding protein  $\alpha$ -actinin was one of the most abundant molecules probed (in terms of labeling density), especially in the two early time points (E19 and P2, Fig. 2.13). Its labeling density at E19 was one of the highest analyzed (second only to CaM) at 12.1 gold/ $0.1\mu\text{m}^2$  and by P2 it had more than doubled to 32.1 gold/ $0.1\mu\text{m}^2$ . These high levels early in development suggest that  $\alpha$ -actinin could play a role in building the core lattice of the PSD and likely forms an important point of contact for the actin cytoskeleton. As one would expect

from a core PSD molecule, all but one PSD across all four time points labeled positively for  $\alpha$ -actinin (table 2.2). Labeling density for  $\alpha$ -actinin at P21 and P60 was 17.8 and 45.8 gold/ $0.1\mu\text{m}^2$ , respectively. It is not clear whether the decrease at P21 is due to real developmental changes in PSD composition or simply variation from one preparation to the next. Regardless, it is still clear that  $\alpha$ -actinin is one of the most densely labeled molecules examined in this study across all time points, supporting its role as an integral structural component of the PSD. Consistent with this conclusion, the labeling density of  $\alpha$ -actinin at P60 was the highest labeling density seen for any molecule examine at any of these developmental time points.

### *Glutamate Receptors*

Three different glutamate receptor subunits were probed in this study; two subunits of the NMDA-type receptor (NR1 and NR2b) and one from the AMPA-type receptor (GluR1). Fig. 2.14 shows representative examples of PSDs labeled at each time point as well as a graph of the average labeling densities for each antibody. The NMDA receptor subunit NR1 (NR1 is the subunit required to form a functional ion channel) was present at a labeling density of 5.3 gold/ $0.1\mu\text{m}^2$  at E19 and 4.4 gold/ $0.1\mu\text{m}^2$  at P2. Although there is a slight decrease it is not significant, suggesting that there is little change in NR1 composition from the late embryonic stage (E19) through the early postnatal stage (P2). In the P21 PSDs NR1 labeling increased five-fold from that of P2 to 22.3 gold/ $0.1\mu\text{m}^2$  and then dropped back down to 8.7 gold/ $0.1\mu\text{m}^2$  at P60. It is not clear why there is a spike in the abundance of NR1 during adolescence (P21), but the same pattern was seen in the labeling density for another NMDA receptor subunit NR2b, suggesting that the two receptor components could be up-regulated in concert at this stage of development. In fact, NR2b labeling densities are similar to NR1 across all four time points with a labeling density of 7.9, 8.5, 24.3 and 12 gold/ $0.1\mu\text{m}^2$  at E19, P2, P21 and P60, respectively.

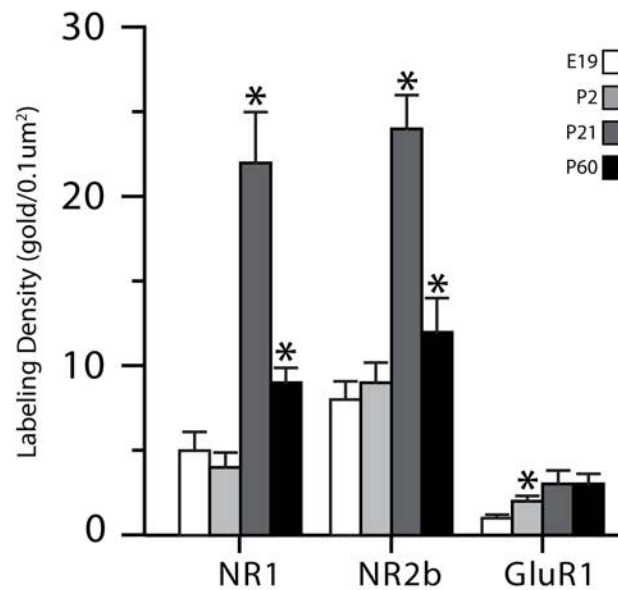
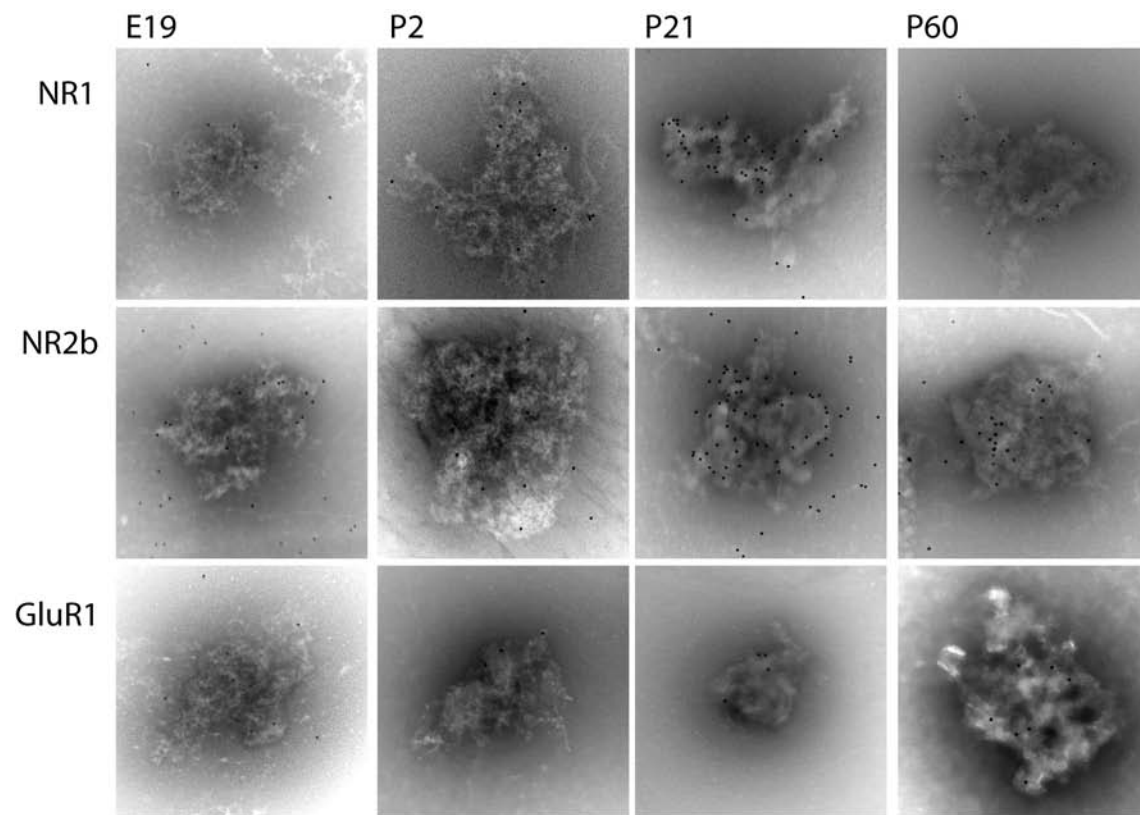


**Fig. 2.14** Immuno-gold labeling of NR1, NR2b and GluR1 at E19, P2, P21 and P60.

Electron micrographs of representative PSDs isolated from E19, P2, P21 and P60 immuno-gold labeled for NR1, NR2b and GluR1. Average labeling density for each antibody at each developmental time point is shown in the graph. Asterisks indicate a significant change from the previous time point at a p value < 0.05.

The AMPA receptor was the least abundant molecule probed in this study with early labeling for its subunit GluR1 as low as 1.0 gold/ $0.1\mu\text{m}^2$  at E19 and only 1.5 gold/ $0.1\mu\text{m}^2$  at P2. This number only doubled by P21 to 2.7 gold/ $0.1\mu\text{m}^2$  and 3.1 gold/ $0.1\mu\text{m}^2$  at P60. These low levels are intriguing as the AMPA receptor generates the bulk of the ion influx at most excitatory synapses, and will be discussed in more detail later. This low immuno-gold labeling is also consistent with the low relative abundance of this molecule revealed by Western blot analysis (Fig. 1.5). Despite the low density, the majority of PSDs at all time points exhibited labeling above background for GluR1 (see table 2.2).

### *Signaling Proteins*

CaMKII is one of the most well studied molecular components of the PSD. The data in Fig. 2.15 show that both  $\alpha$ - and  $\beta$ CaMKII were present in PSDs isolated early (E19 and P2) and later (P21 and P60) in development. Labeling for both isoforms of the kinase approximately tripled from E19 (3.1 gold/ $0.1\mu\text{m}^2$  for  $\alpha$ CaMKII and 2.1 gold/ $0.1\mu\text{m}^2$  for  $\beta$ CaMKII) to P2 (7.8 gold/ $0.1\mu\text{m}^2$  for  $\alpha$ CaMKII and 9.0 gold/ $0.1\mu\text{m}^2$  for  $\beta$ CaMKII), which was followed by a three- and four-fold increase, respectively, by P21 (28 gold/ $0.1\mu\text{m}^2$  for  $\alpha$ CaMKII and 35 gold/ $0.1\mu\text{m}^2$  for  $\beta$ CaMKII). The density of both isoforms of CaMKII did not show a significant change from P21 to P60, suggesting that by P21 labeling for CaMKII had become asymptotic. While the majority of PSDs showed labeling for both isoforms of CaMKII across all time points (96% for  $\alpha$ CaMKII and 94% for  $\beta$ CaMKII), a small number of them contained a lower amount (seven PSDs from both E19 and P2 showed  $< 1$  gold/ $0.1\mu\text{m}^2$  and four from P21 and P60 showed  $< 10$  gold/ $0.1\mu\text{m}^2$ ). Unlike  $\alpha$ CaMKII, no previous work has quantified the  $\beta$  isoform of CaMKII within individual PSDs. The high levels of  $\beta$ CaMKII were somewhat unanticipated as  $\alpha$ CaMKII is typically thought of as the PSD-bound isoform. Although the labeling density of CaMKII early in development is similar to that of the NMDA receptor subunits NR1 and



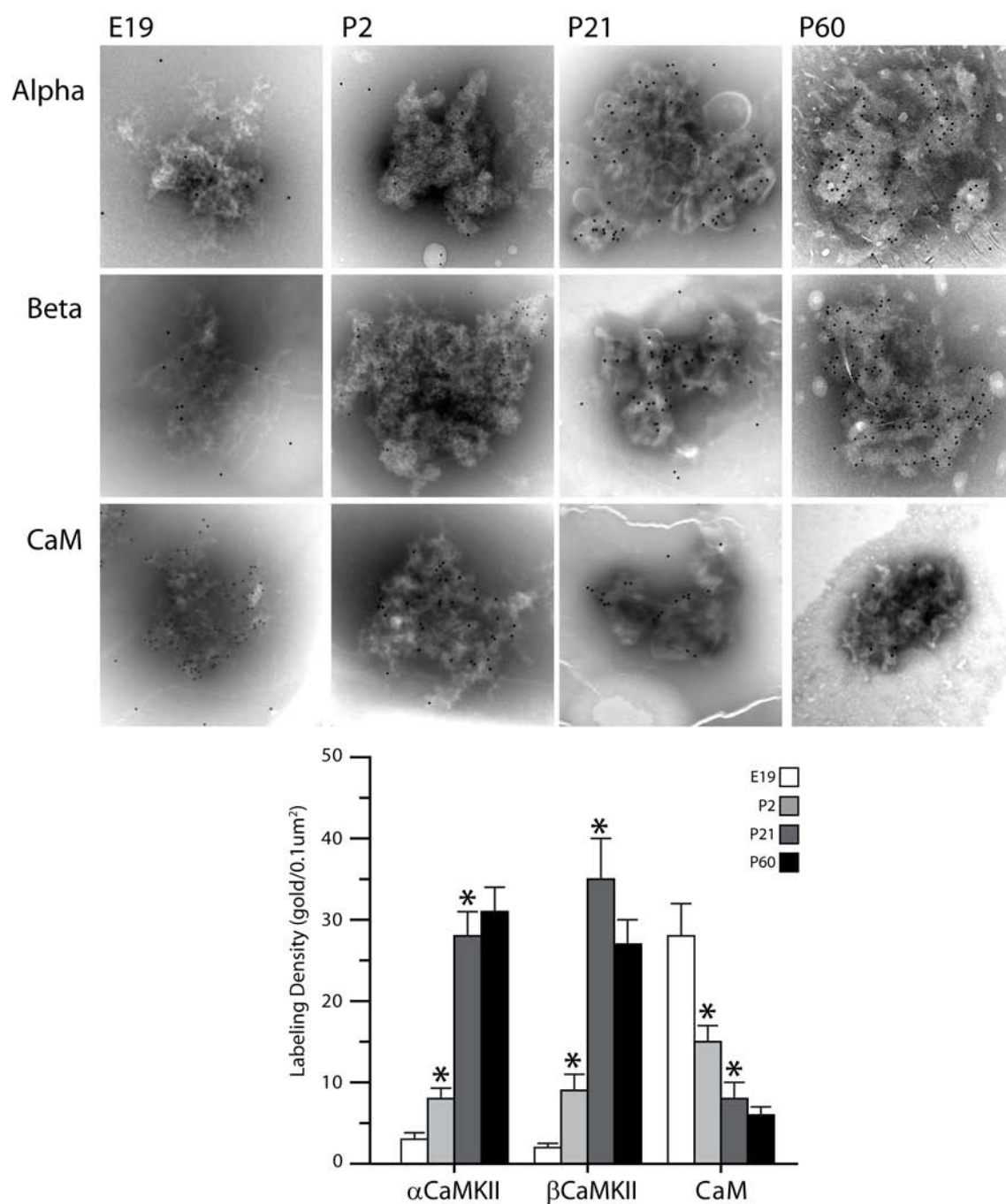


**Fig. 2.15** Immuno-gold labeling of  $\alpha$ CaMKII,  $\beta$ CaMKII and CaM at E19, P2, P21 and P60.

Electron micrographs of representative PSDs isolated from E19, P2, P21 and P60 immuno-gold labeled for  $\alpha$ CaMKII,  $\beta$ CaMKII and CaM. Average labeling density for each antibody at each developmental time point is shown in the graph. Asterisks indicate a significant change from the previous time point at a p value < 0.05.

NR2b, by P21 it is more comparable to that of the scaffolding molecules PSD-95 and  $\alpha$ -actinin. This high level of CaMKII suggests it not only plays an enzymatic role, but also functions as a structural component within the PSD.

CaM is a small protein that senses changes in intracellular calcium and transduces this signal to downstream molecules such as CaMKII. Interestingly, CaM was the only molecule in this study that followed an inverse trend and showed its highest PSD labeling at E19 (28.1 gold/ $0.1\mu\text{m}^2$ ) with a significant downward progression out to P21 (8.0 gold/ $0.1\mu\text{m}^2$ ), as the decrease in labeling density from P21 to P60 was not statistically significant (Fig. 2.15). This decline in labeling through development suggests that the increase seen in the other molecules is not a general rule for all proteins in the PSD and also suggests a greater demand for signaling through CaM during early stages of PSD development.

As mentioned above, for each experiment a negative control was run where no primary antibody was used during the labeling protocol. This was done to show that labeling was specific to the addition of primary antibody, and to establish a background labeling density that could be subtracted from the experimental condition. Fig 2.16 shows representative PSDs from each of the developmental time points with secondary antibodies derived from both mouse and rabbit IgG molecules. It is clear from the images of control PSDs that background labeling was always minimal. Across all experiments the background labeling density was consistently low and ranged from 0.7 – 7.0 gold particles/ $0.1\mu\text{m}^2$ .

### **Spatial Analysis of Immuno-Gold Labeling**

One of the major advantages of immune-gold labeling is that it provides spatial information concerning the distribution of the target molecule. With this in mind, Ripley's K function (RKF) analysis was performed to test whether the distribution of gold labeling was random or clustered. The first step to this analysis was to extract the XY coordinates corresponding to the center of each gold ball and calculate the convex hull surrounding each

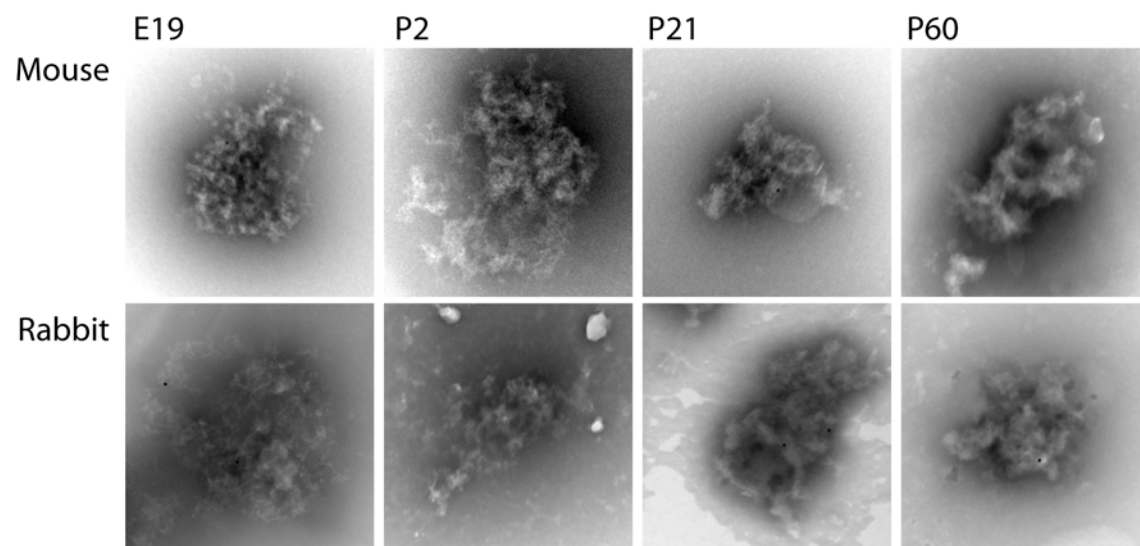


**Fig. 2.16** *Immuno-gold labeling controls.*

Immuno-gold labeling controls for PSDs isolated at E19, P2, P21 and P60. PSDs were exposed to the gold-conjugated secondary antibody, but not a primary antibody. Labeling densities for each control was subtracted as background from those labeled with primary antibody. In this study, GluR1 was the only antibody raised in rabbit, all others were monoclonal antibodies produced in mice.

data set for use as a boundary (Fig. 2.17). The convex hull is a polygon whose vertices are defined by the outer most points of the data set. It is not a perfect representation of the PSD boundary, but it has been used previously for the same purpose (Petersen et al., 2003). Despite potential differences between the convex hull and the actual PSD boundary, it does represent the area labeled by immuno-gold markers and is free of subjectivity. Next, the points falling on the interior of the convex hull are compared simulated randomness by randomly placing particles at the same density placed within the convex hull (Fig. 2.18). Since labeling on PSDs actually occurs in three dimensions, we wanted to capture this in our simulation by adding a third dimension (60 nm thickness) to the convex hull before randomly placing gold within the volume (details of the simulation process can be found in the materials and methods as well as the appendix). The XY coordinates of the randomly distributed gold particles were then extracted as with the experimental data and the simulation process was repeated for 100 trials to provide a basis for analysis of non-random distribution.

RKF analysis works by calculating the average number of points that fall within increasing radii extending from the center of each point in the set. If the gold particles are clustered, more will fall within a smaller radius when compared to the random distributions. In this case, the gold labeling was considered to be clustered if the RKF plot fell outside of the minimum or maximum envelopes defined by the 100 trials of simulated random distributions (Fig. 2.19). RKF plot is always a sigmoidal curve, because we are dealing with point pattern distributions within a finite space (convex hull). Eventually the radius of measurement becomes large enough to capture all of the gold balls and the number within increasing radii becomes asymptotic.

Among the eight different molecules probed in this study, at all four developmental time points, RKF analysis showed significant clustering in the majority of PSDs analyzed. Table 2.3 summarizes the number of PSDs analyzed in each group and those that showed a significant

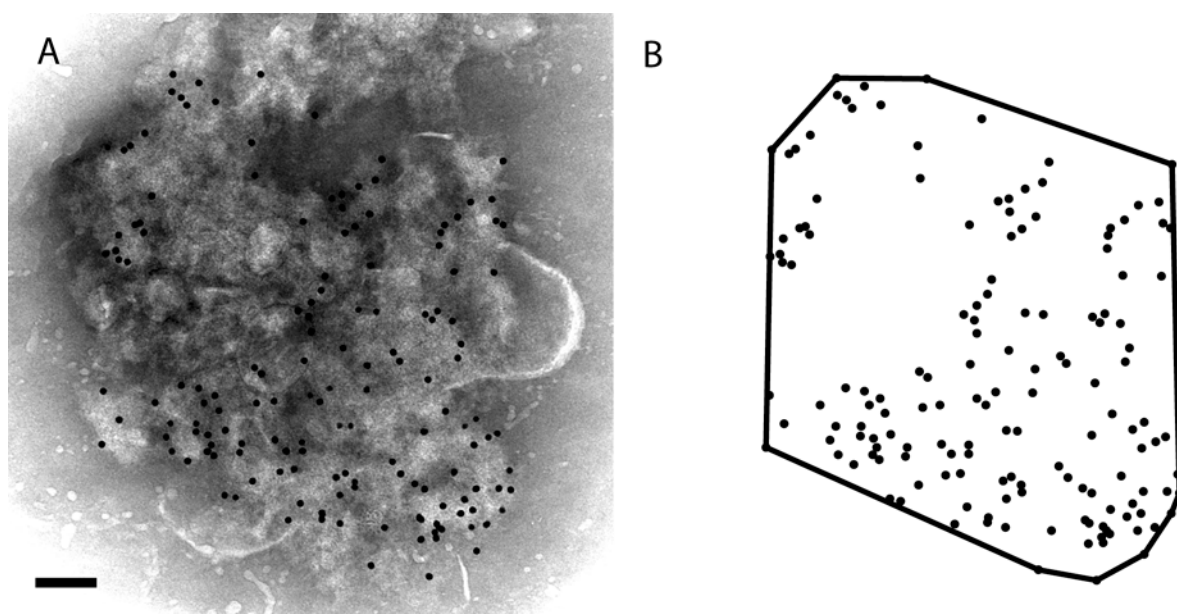


**Fig. 2.17** *The convex hull as a boundary for spatial analysis.*

(A) Electron micrograph of a P60 PSD immuno-gold labeled for PSD-95. (B) To analyze spatial distribution of the gold particles in A, the XY coordinates for each gold marker is extracted (black dots) and they are bounded by the convex hull of that data set (black line surrounding points). Scale bar represents 100 nm.

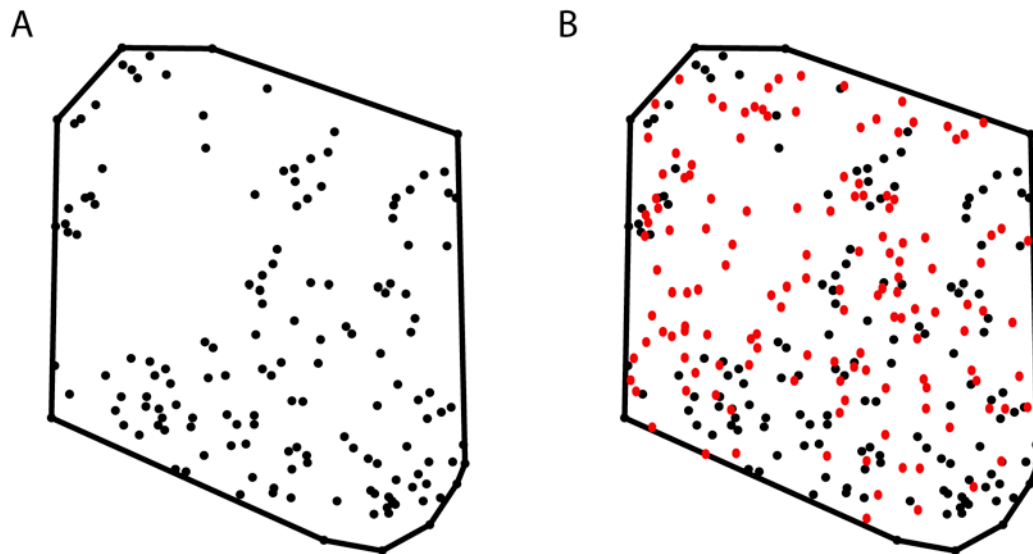


**Fig. 2.18** *The convex hull as a boundary for spatial analysis.*

(A) Convex hull and experimental data set as seen in Fig. 2.17. (B) For comparison, the same number of points that fall within the interior of the convex hull is randomly distributed by Monte Carlo simulation within the boundary (red dots). One hundred iterations of randomly distributed particles are generated and spatial analysis is then performed on the experimental and simulated data points.

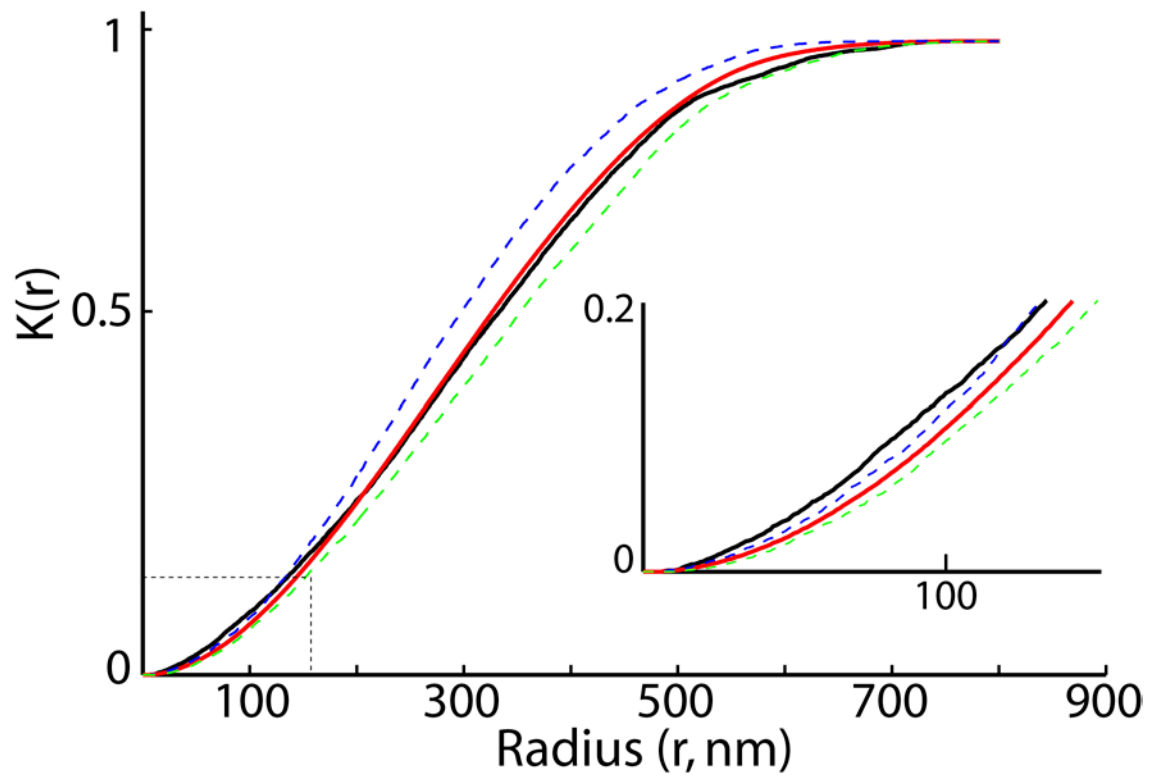


**Fig. 2.19** RKF plot showing clustering.

The Ripley's K-function (RKF) plot of the experimental data (black solid line) is compared to the simulated complete spatial randomness (red solid line). The blue and green dashed lines represent the maximum and minimum envelopes, respectively, defined by the 100 iterations of simulated random distributions. The inset is a blow-up of the early portion of the plot, bounded by the black dashed line, where it is clear that the experimental plot (black) is outside of the maximum envelope of the simulated random data (blue dashed line).

	<b>E19</b>	<b>P2</b>	<b>P20</b>	<b>P60</b>
<b><math>\alpha</math>-Actinin</b>	6 of 7	12 of 15	8 of 10	15 of 16
<b><math>\alpha</math>CaMKII</b>	1 of 4	10 of 12	14 of 16	14 of 17
<b><math>\beta</math>CaMKII</b>	1 of 1	10 of 11	14 of 15	12 of 15
<b>CaM</b>	8 of 10	10 of 14	NA	5 of 6
<b>GluR1</b>	NA	2 of 3	NA	4 of 7
<b>NR1</b>	2 of 4	9 of 15	5 of 8	13 of 16
<b>NR2b</b>	3 of 6	11 of 16	2 of 11	14 of 16
<b>PSD95</b>	NA	6 of 6	12 of 13	15 of 16

Table 2.3 *Number of individual PSDs that showed clustering by RKF analysis for each antibody and developmental time point.*



deviation from random. If a PSD did not have a minimum of 10 gold balls that fell within the convex hull we chose to remove it from the analysis, because the small number of data points led to RKF plots with large fluctuations. Because of this criterion, some PSDs at E19 and P2 could not be analyzed since labeling densities were generally lower early in development. CaM is an exception to this as labeling was high at E19 and was minimal by P60. It is recognized there are a variety of ways for point-pattern distributions to be non-random (this is discussed further in the appendix). However, this is the first time that this type of spatial analysis has been done using labeling for such a panel of antibodies, and across multiple developmental time points and we can conclude that the distribution of this subset of PSD proteins is non-random. This suggests that the PSD is assembled systematically with molecules distributed in an organized manner. While this may be a seemingly obvious conclusion, as most people believe the PSD is a well organized assembly of protein machinery, this is some of the first quantitative evidence to support such a hypothesis.

### **Chapter 3: Structure of Cryo-preserved PSDs during development**

Electron microscopy has long been an invaluable tool in biological research and neuroscience is no exception. As mentioned in the introduction, the exact nature of the synapse was under constant debate until the resolving power of the EM was established for use on biological specimens. One of the early limitations inherent in examination of specimens in the EM is that samples must be dehydrated before they can be placed in the high vacuum of the microscope's column. This is obviously problematic for biological specimens that reside normally in a water-based medium and the functional structure of most biological molecules evolved to be so in an aqueous environment. Thus, the examination of biological material in a hydrated state is impossible using classical sample preparation methods. It turns out that if one can cool water fast enough (~5 ms) it will freeze before the water molecules have time to crystallize, and a solid amorphous state of water known as vitreous ice can be achieved (Dubochet et al., 1988). The advantage gained by doing so is that anything captured in vitreous ice is preserved in a frozen-hydrated state. This alone overcomes two major hurdles. From the biology side, the specimen is now preserved in a hydrated state, like a snap-shot of the specimen in its aqueous environment, while from the EM side, the water is in a solid state so that it can now be placed in the vacuum of the microscope and resist evaporation. The only trick now is keeping the specimen frozen (approximately -190°C), but the development of cryo-EM specimen holders has resolved this issue. The advent of cryo-preservation techniques for use in electron microscopy has revolutionized the use of EM for the study of biological specimens and it provides several major advantages over traditional sample preparation methods. One advantage is the lack of any chemical fixation or heavy metal stains that may alter or obscure the true structure of the specimen. The lack of stain means that contrast in the image is generated by the differential density between the specimen itself and the water

surrounding it. Because of this, the images represent the actual disposition of matter (i.e., proteins, lipids, nucleic acids, etc.) in the specimen. It was alluded to above, but the frozen-hydrated state of cryo-preserved specimens represents a structure as close to native as possible using electron microscopy. This is because all of the water-specimen interactions that play a role in structural stability are presumably still intact.

To date, observation of cryo-preserved PSDs has been very limited. They have not been the focus of any published study, but have been seen peripherally in a couple papers using cryo-preserved synaptosomes to study the arrangement of cleft protein and virus entry (Lucic et al., 2005; Maurer et al., 2008). Cryo-preserved PSDs are also seen briefly in two papers investigating synaptic architecture of cryo-preserved cultured neurons (Fernandez-Busnadiego et al., 2010; Lucic et al., 2007). In all cases the PSDs seen are viewed only from the side. They are not the focus of the studies and are merely used as a morphological landmark. Because of the advantages provided by cryo-EM, we chose to investigate the structure of cryo-preserved isolated PSDs using electron tomography. The relatively thin dimensions of isolated PSDs (60-100 nm) makes them ideal for cryo-preservation, because one must capture them in a sheet of vitreous ice that is thin enough for the electron beam to easily penetrate (100-500 nm). Because the sheet of ice is thin the majority of PSDs are preserved in an *en face* orientation, allowing for investigation of the entire structure at once. Because the isolated PSD preparations are most well characterized in adult rats it seemed like a good place to start, and following the description of adult isolated PSDs they will be compared to those isolated at E19, P2 and P21.

### **PSDs isolated from adult rats are characterized by layers of distinct protein.**

One of the distinct advantages of electron tomography is the ability to generate cross-sections of the final reconstruction. This is a powerful tool because a single electron micrograph contains all three-dimensional information collapsed into a two-dimensional projection. Because of this, interpretation can often be misleading. In fact, the name

postsynaptic density itself may be misleading. It is certainly more densely packed with protein than other areas of the synapse, but its density is likely exaggerated by the collapsing of overlapping proteins into a single two-dimensional image. By generating tomograms of cryo-preserved PSDs distinct layers of protein were distinguishable in the final reconstructions. It is important to point out that PSDs are highly heterogeneous from one structure to another and these layers are not always perfectly delineated. Figure 3.1 shows three cryo-preserved PSDs isolated at P60 that illustrate the two major layer types seen routinely. The top panels in Fig. 3.1A-C are projections through the full tomographic reconstruction. Because the *en face* view of cryo-preserved PSDs is entirely novel a thorough description of the morphological features evidence in these reconstructions is warranted. Most often PSDs are associated with the edge of the carbon support of the holey carbon film as seen in Fig. 3.1A and B. It is rare to find isolated PSDs that are not in contact with the edge of the carbon or perhaps another PSD that is in contact with the carbon. Of the 25 tomograms collected at this developmental time point, the PSD illustrated in Fig. 3.1C is the best example of such a case. This obviously reflects an attraction between the PSD and the carbon substrate. It is important to note that in cryo-micrographs the specimen will appear dark in the image, while the inverse is true in the negatively stained material presented in chapter 2. This is because the contrast in cryo-preserved specimens is generated by the differential density between the sample itself and the surrounding water, while in negatively stained specimens the sample is actually less dense than the surrounding stain.

The PSD in panel A has the most well defined edges, in that it is roughly circular. This is not the case with all PSDs, however, and the edges are often less well defined, resulting in non-circular shapes such as that seen in panels B and C. There are often smaller protein complexes that can also be seen suspended in the ice. Two such complexes are marked by asterisks in Fig. 3.1A. The complex on the right side of the micrograph is likely too small (~100 nm) to be a

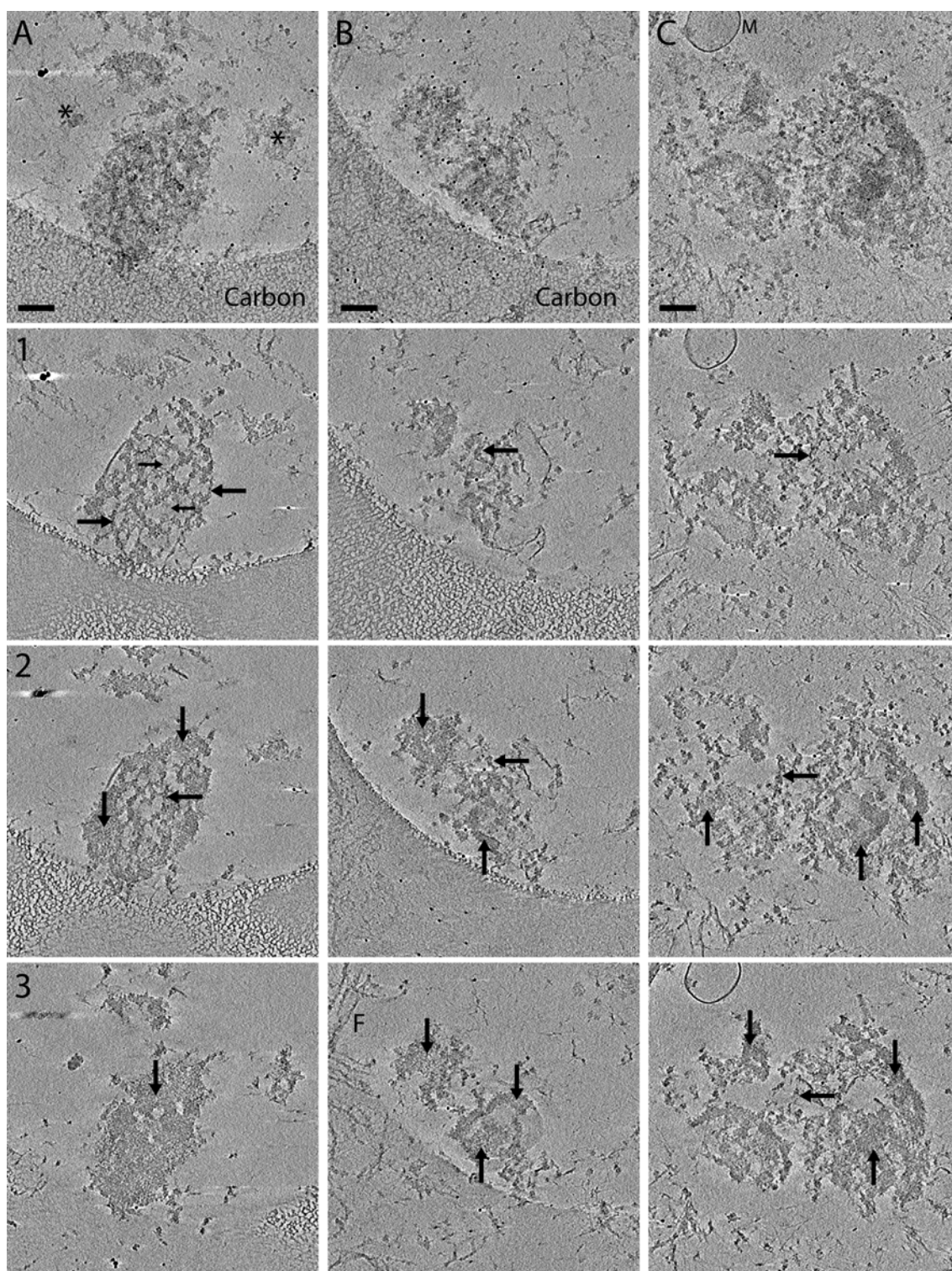


**Fig. 3.1** *Cryo-preserved PSDs isolated at P60.*

(A-C) Representative examples of cryo-preserved PSDs isolated at P60. Lower panels (1-3) are successive 20 nm digital cross-sections through the reconstructed tomographic volume. Scale Bar represents 100 nm.

PSD, but it could be a piece of a PSD that has broken off of a larger complex. A small piece of membrane is visible in panel C and is marked by an “M”. While it is not attached directly to the PSD in this example, similar membranes are often seen still attached to the organelle (examples of such membranes can be seen in Fig. 3.8 and 3.9). A filamentous contaminant can be seen in the top left corner of panel B. This type of filament is relatively common and is seen regularly in negatively stained PSDs as well, such as in Fig. 1.2. While some contaminants do exist the majority of structures are PSDs and appear similar to the three shown in Fig. 3.1. Variations in PSD structure will be explored in the following sections.

Below each PSD shown in the top panels of Fig. 3.1A-C there are three 20 nm tomographic cross-sections cut through the corresponding PSD above it. The cross-sections were cut parallel to the XY axes and each successive image represents a section as you move down along the Z-axis of the reconstructed volume. For the sake of demonstrating similarities shared by all three PSDs as well as variations evident in each individual they will be compared at each cross-section generated. The first cross-section (labeled as 1 in Fig. 3.1) most clearly illustrates the mesh-like lattice that is usually most easily visible on one of the two faces of the PSD. The mesh is made of protein with various morphologies, and the details are more closely examined in Fig. 3.2, but the large horizontal arrows in the cross sections of Fig. 3.1 point out some of the thin protein components that run laterally through the mesh. While both filamentous and globular proteins appear to make up the mesh it is characterized by the appearance of large holes (small horizontal arrows in cross-section 1 of Figs. 3.1A-C) filled with vitrified water. From here on this type of protein arrangement will be referred to as PSD-mesh. It is clear from the first cross-section of all three PSDs that this PSD-mesh is present and that it accounts for the majority of the protein at this face of the PSD.

In the second cross-section the interface between the loosely packed PSD-mesh and the denser material of the next layer (vertical arrows) is visible. In panel A (cross-section two) a

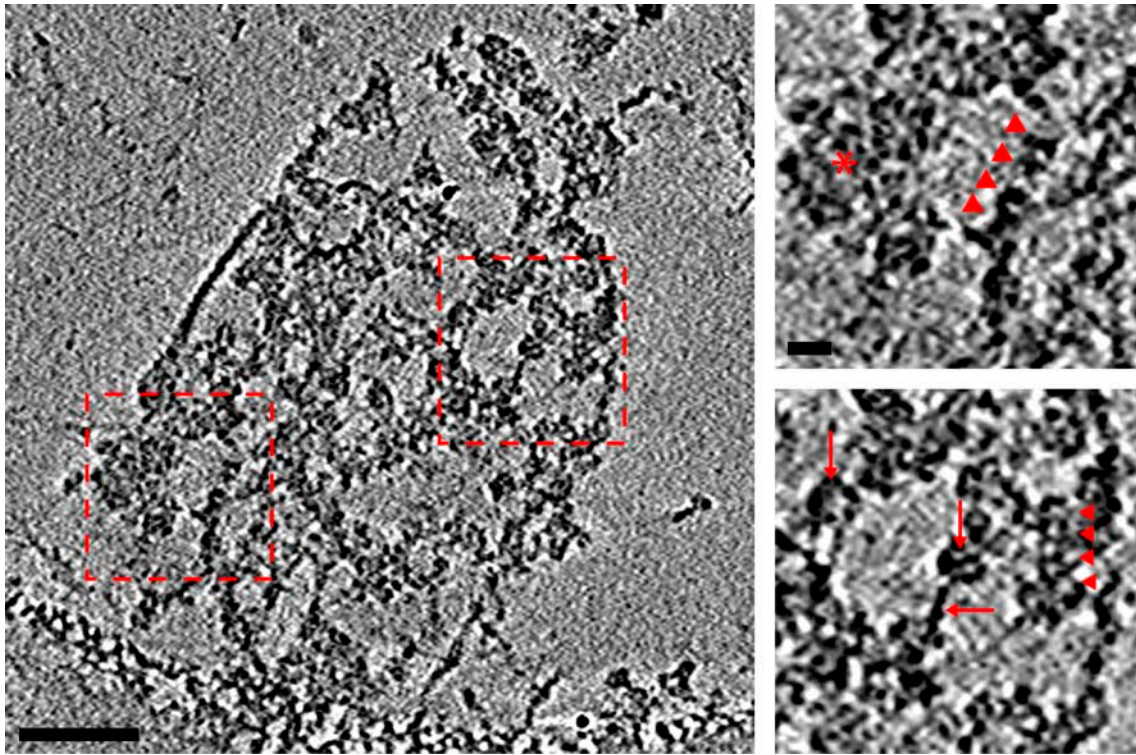


**Fig. 3.2** *PSD-mesh observed in cryo-preserved P60 PSD.*

The left panel is a larger image of the first cross-section shown in Fig X panel A (scale bar is 100 nm). The red dashed box on the left corresponds to the blow-up in the top-right panel and the dashed-box on the right corresponds to the blow-up in the bottom-right panel (scale bar is 20 nm).

ring of densely packed protein has become visible around the outer edge of the PSD and the PSD-mesh is still visible toward the center of the organelle (horizontal arrow). The distribution of densely packed protein in panels B and C (cross-section two) is different from the ring surrounding the outside of the PSD in A and can be seen as more randomly distributed through the structure of the PSDs in B and C (vertical arrows). Some of the dense protein is seen as globular patches and other portions appears as dense bands (or ropes) of protein. The far-right vertical arrow in panel C points to a small ring produced by one of these bands of protein. These ring structures are seen often and will be discussed in greater detail in the following section.

In the third cross-section from each PSD the majority of the PSD-mesh is gone and the dense-layer, as it will be called from here on, is the predominant morphological feature. In Panel A (cross-section three) the entire PSD consists of a layer of densely packed of protein. Despite a few small holes penetrating this layer there is a consistent sheet of granular protein. This complete layer across the entire extent of the PSD is not typical, however, in the cryo-preserved PSDs reconstructed in this study. Most PSDs display a more patchy distribution of both dense globular regions as well bands of protein like those seen in cross-section three of panels B and C (vertical arrows). The horizontal arrow in the final cross-section of panel C points to portions of the PSD-mesh that extends all the way up into the open regions of the dense layer. The letter “F” in the third cross-section of panel B is labeling the filamentous contaminant mentioned above, because it is more noticeable in the cross-section of the tomographic reconstruction.

While the PSD-mesh and the dense layer are most easily visualized at opposite faces of the PSD, the two morphologies are not always exclusive to one face or the other. The PSD in panel A shows a pretty clear delineation between the two layers, but both PSDs in panels B and C show portions of dense material at the face that is predominantly mesh. The PSD in panel C



clearly shows mesh structure at the face containing mostly dense material. Because of this, it is difficult to completely separate the two layers in every PSD, however, there is certainly a bias for one or the other toward either face of the complex. A more detailed description of these two layers is presented below.

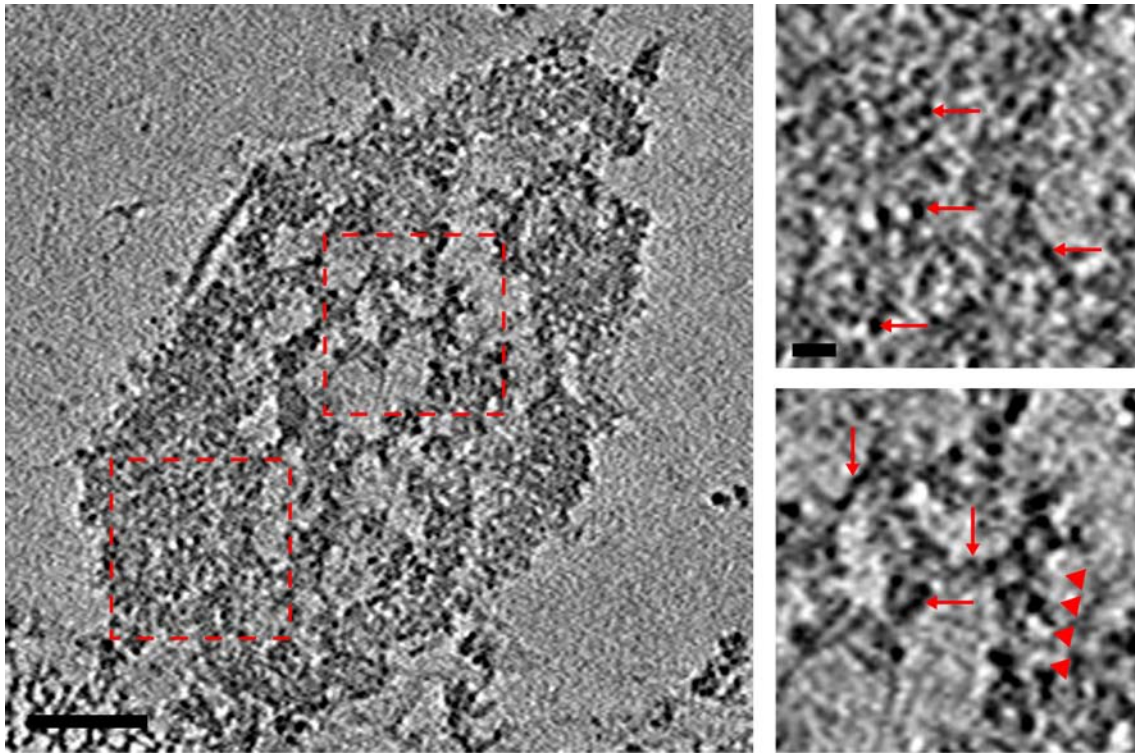
**The PSD-mesh and dense layer are variable in nature and contain a complex mixture of protein components/morphologies**

Upon closer inspection the mesh and dense layer of the PSD provide a wealth of structural data. For instance, the PSD-mesh is not simply a lattice of thin filamentous proteins, but rather a complex mixture of globular proteins and filaments connected in a variety of ways. Fig. 3.2 shows a closer view of the first cross-section of the PSD in Fig. 3.1A. The mesh-like structure is immediately apparent. There are large holes in the mesh and there are filaments and strand-like arrangements of protein running laterally through the cross-section. The regions bound by red dashed boxes are blown up in the panels to the right and illustrate the complexity of the protein arrangement in the PSD-mesh. The red dashed box on the left corresponds to the top-right panel. The asterisk indicates a region of densely packed particles that are connected to dense layer that is more clearly seen in the next cross-section. The four arrowheads point to globular proteins that are strung together to form a strand-like band of protein running laterally through the PSD-mesh. While the individual components are visible in the blow-up, the strand-like appearance is more apparent in the lower magnification view in the left panel. The red dashed box on the right corresponds to the lower-right panel. Vertical arrows point to globular proteins that are often seen in the PSD-mesh. The one on the left appears to be composed of smaller subunits (at least five) and the one to the right has two holes (or portions of lower density) in the middle. It is connected to another portion of the mesh via a horizontal filament, which is indicated by the horizontal arrow. The four arrowheads indicate what appears to be a

chain of ring like densities strung together. It is not clear what these are, but these small ring shaped proteins are seen commonly.

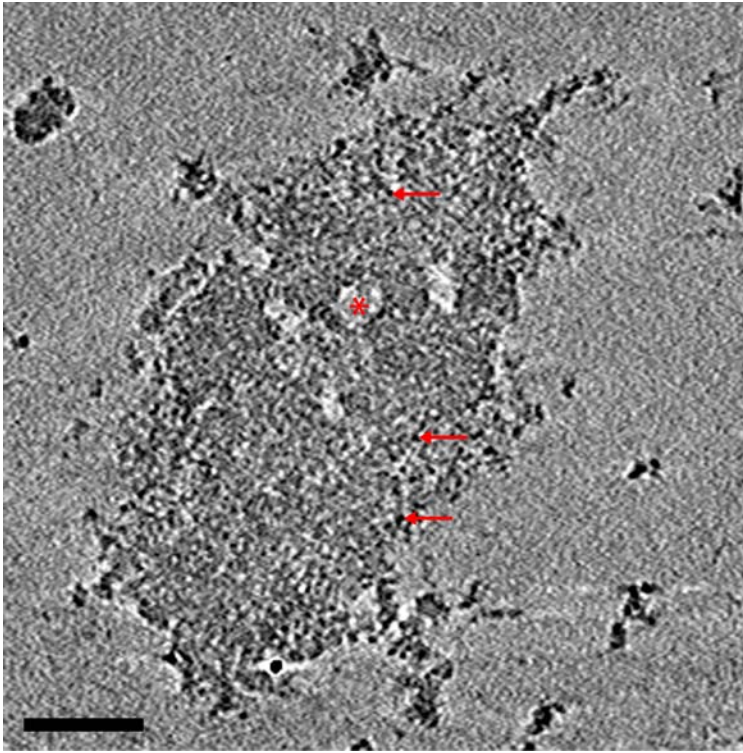
Fig. 3.3 shows a closer view of the second cross-section of the PSD in Fig. 3.1. In this section the dense layer of PSD protein is clearly visible around the perimeter of the PSDs and the PSD-mesh is still visible toward the center. As in Fig. 3.2 the red dashed box to the left corresponds to the blow-up in the top-right panel and the dashed box to the right corresponds to the blow-up in the lower-right panel. The top-right panel is a blow-up of the dense region that is partially seen in the first cross-section (see Fig. 3.2). Arrows point to the small granular particles that make up the majority of the dense layer. The lower-right panel depicts the middle portion of the cross-section that still contains PSD-mesh material. Similar strands of protein (arrowheads), as well as globular (horizontal arrow) and filamentous (vertical arrows) protein can be seen as in Fig. 3.2.

Fig. 3.4 shows a closer view of the third cross-section of the PSD in Fig. 3.1. No regions are blown up, because nothing more is revealed than in Fig. 3.3. It is a large, continuous layer of small granular proteins (some of which are highlighted by red arrows). A few small holes can be seen in the dense layer and one is marked by an asterisk. This dense layer, however, is not so continuous in most PSDs (as mentioned above). More often it is broken apart into island-like patches of density that are distributed across the PSD-mesh. Fig. 3.5 is a blow-up of the third cross-section of the PSD in Fig. 3.1 panel C. It is clear that the same densely packed protein exists, but it is not continuous across the entire PSD and exists in a more modular distribution. Vertical arrows in Fig. 3.5 indicate the separate regions of densely packed protein distributed through the dense layer. Portions of the PSD-mesh that link these regions together can also be seen in this cross-section and they are labeled by horizontal arrows. Arrowheads track along and point to thinner bands of dense protein that are often seen. They appear to be composed of the same material as the larger patches.



**Fig. 3.3** *Mid-level cross-section observed in cryo-preserved P60 PSD.*

The left panel is a larger image of the second cross-section shown in Fig X panel A (scale bar is 100 nm). The red dashed box on the left corresponds to the blow-up in the top-right panel and the dashed-box on the right corresponds to the blow-up in the bottom-right panel (scale bar is 20 nm).



**Fig. 3.4** *Continuous dense layer observed in cryo-preserved P60 PSD.*

Larger image of the third cross-section shown in Fig X panel A (scale bar is 100 nm). Arrows point to granular particles and the asterisk indicates a hole in the dense layer.

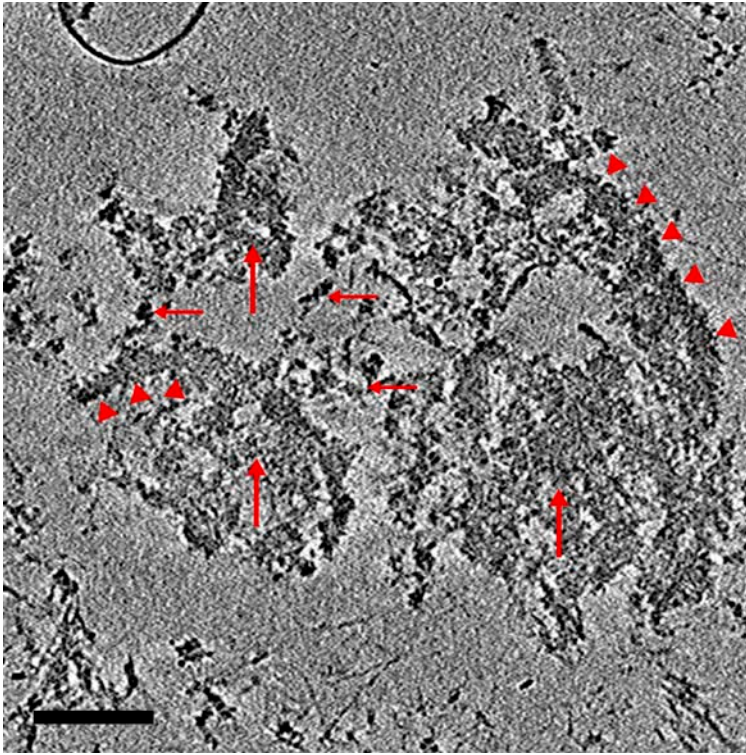


**Fig. 3.5** *Non-continuous dense layer observed in cryo-preserved P60 PSD.*

Larger image of the third cross-section shown in Fig X panel C (scale bar is 100 nm). Vertical arrows point to island-like patches of dense protein. Horizontal arrows point to portion of the PSD-mesh connecting patches of dense protein. Arrowheads track along dense bands of protein.

So far we have seen that the dense layer of the PSD can range from being a nearly continuous sheet of protein to being broken up into smaller modules of densely packed protein. Those modules are often seen as large (50-300 nm), relatively amorphous clusters of density or they can take on a more linear band-like morphology. These bands, however, will often form into distinct rings of dense protein ranging in size from 50-150 nm in diameter. These rings were seen in negative stain by P21 and they persisted through p60 (Figs X and X), suggesting they form mostly during the later stages of development and are, perhaps, the sign for a more mature PSD. Fig 3.6 shows both a full projection through a reconstructed cryo-preserved PSD as well as a cross-section through the dense layer. It is clear in the full projection that the patches of dense protein seen scattered around are actually connected via the PSD-mesh (horizontal arrows). The vertical arrow in both the full projection and the cross-section point to the ring of dense protein which is part of this PSD's dense layer. Fig 3.7 shows a montage of protein rings found throughout the 25 tomograms collected. In the 20 nm cross-sections shown, the majority of them (A-C and E-G) appear as if they are floating independently in the middle of the ice, but like seen before in Fig. 3.6, portions of the dense layer of the PSD are often separated in space, but connected via the PSD-mesh. The rings in panels D and H can be seen embedded amidst surrounding protein. The proteins rings in this montage illustrate the range of size that can be seen in the PSDs as well as a couple variations. For example, the rings shown in panels F and G both have connecting material that can be seen within the ring, and panel H shows a crescent shaped ring, illustrating the variation that can exist in the roundness of the ring. It is worth noting that these rings do not always sit parallel to the plane of the PSD. Sometimes the dense bands of protein that make up the perimeter of the rings traverse up or down through the PSD, causing the ring they form to sit orthogonal to the plane of the PSD. As seen in the negatively stained tomograms (Fig. 2.8) these protein rings are not always proper rings like a donut. Some of them are actually more spherical and only appear as rings when a



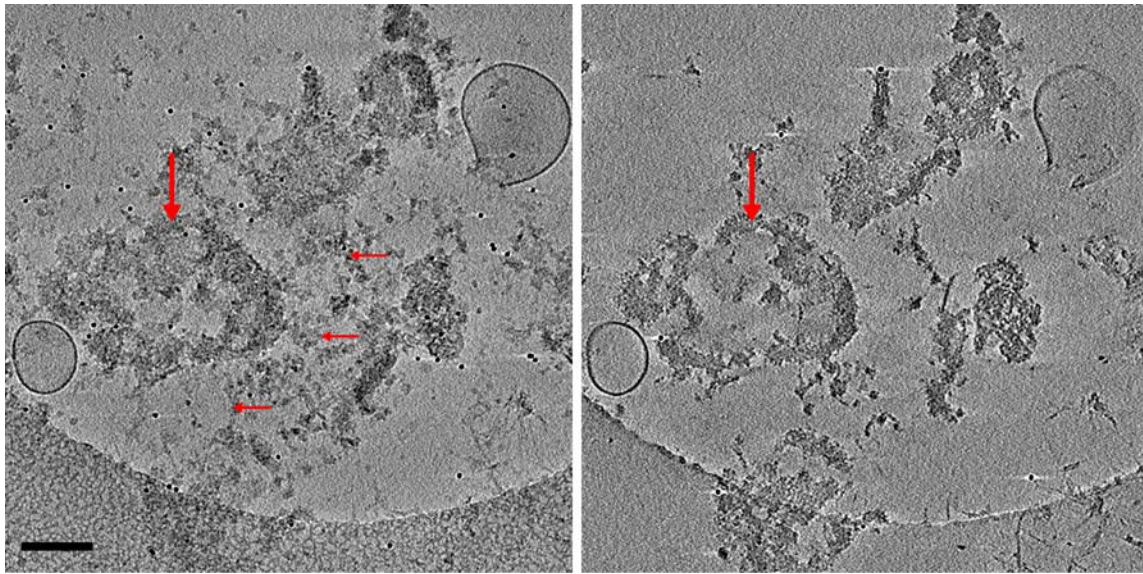


**Fig. 3.6** *Illustration of protein rings in the dense layer of P60 PSDs.*

The left panel is a full projection of the tomographic reconstruction, and the right panel is a 20 nm cross-section through the dense layer of the PSD. The vertical arrow indicates a protein ring that is present and the horizontal arrows indicate portions of the PSD-mesh that are not visible in the cross-section. Scale bar is 100 nm.

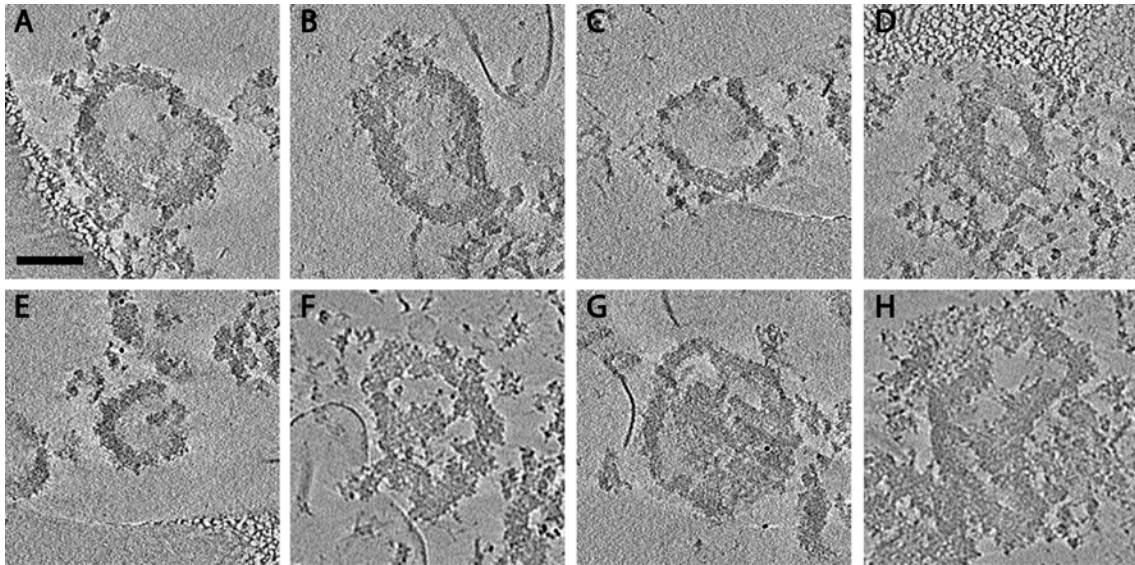


**Fig. 3.7** *Montage of protein rings of various size and shape.*

A-H represent protein rings found in the dense layer of various PSD reconstructions. Some of them appear to be isolated (A-C and E-G), because of the cross-sectioning. Others are seen in contact with other portions of the PSD such as the mesh (D and H).

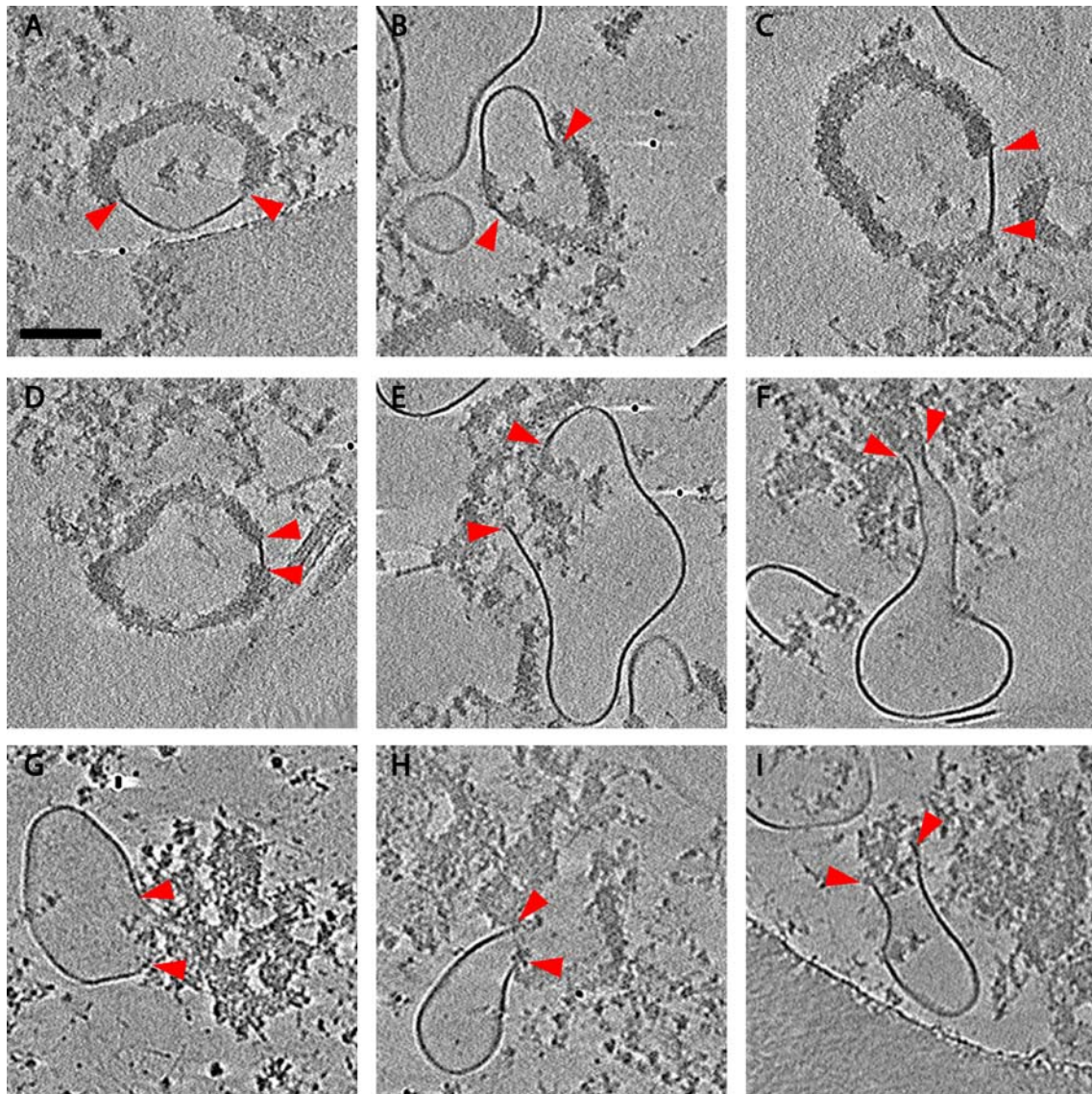


cross-section is taken through the middle. Sometimes they are more like a half-sphere, or bowl that is open on one end so as you slice down through them they close off on one end.

### **Detergent resistant membrane remains attached to isolated PSDs**

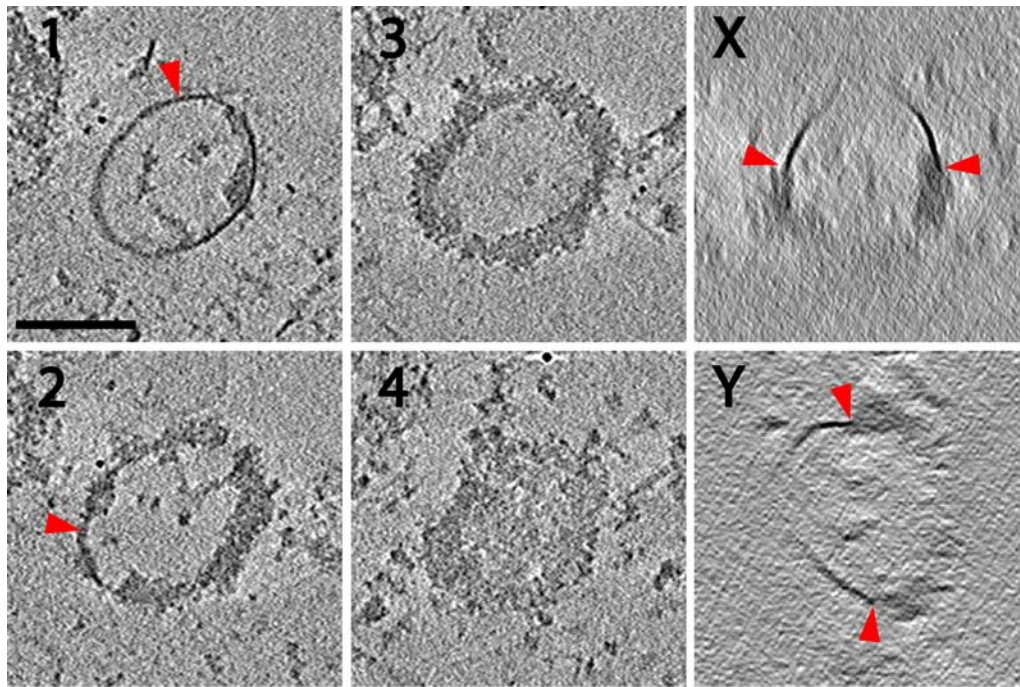
Despite the fact that PSDs have gone through two separate detergent extractions (with 0.5% Triton X-100) during the isolation process, membrane fragments still remain in the subcellular fraction. Most of this membrane is attached to PSDs. The membrane is often embedded within the PSD, apparently attached at the edges to protein density, but it also can be seen sticking out from the PSDs in balloon-like crescents. These crescents are not spherical vesicles and it is clear that they are not continuous all the way around, because the edges of the membrane are in direct contact with the protein of the PSD. Figure 3.8 shows a montage of cross-sections through pieces of PSD that have membrane embedded in them or attached as membrane crescents. Panels A-D show protein rings like those commonly seen, but they are broken at points with membrane spanning these broken regions. Panels E-I show membrane crescents in a variety of morphologies that are in contact with PSD protein. While they generally appear in contact with the more densely packed protein of the PSD, they can, on occasion, be attached to the PSD-mesh like in panel E. The red arrows in Fig. 3.8 indicate the points of attachment for each end of the membranes. In all cases the membranes appear smooth, suggesting that there are not proteins embedded in it.

Fig. 3.9 shows a close-up of a protein ring that has membrane attached to it continuously around the perimeter. This particular protein ring was found in PSDs isolated at P21 instead of P60, but at this developmental time point protein rings and membranes appear with equal regularity (as is discussed below). Panels 1-4 show successive 20 nm cross-sections through the tomographic reconstruction. The red arrowhead in panel 1 points to the continuous ring of membrane, and again in panel 2, where portions of the protein ring are becoming visible in the cross-section. By panel 3 the membrane is no longer visible, but the protein ring very apparent.



**Fig. 3.8** *Montage of PSD components with membrane still attached.*

A-D show protein rings that are still affiliated with membrane that was not solubilized during the isolation process. E-I represent patches of PSD material that are still in contact with crescent shaped portions of membrane. Arrowheads indicate the two contact points of the membrane with the protein. Scale bar is 100 nm.



**Fig. 3.9** *Protein ring with membrane attached continuously around the perimeter.*

1-4 shows successive cross-sections through a protein ring that has a dome of membrane attached all the way around its perimeter. The red arrowheads in 1 and 2 indicate membrane. Panel 4 illustrates how the protein ring is closed off on one end. X and Y represent cross-sections cut perpendicular to the X and Y axes through the protein ring depicted in 1-4. Arrowheads indicate the two contact points of the membrane with the protein. Scale bar is 100 nm.

It was mentioned above that sometimes these rings are actually more bowl shaped, which is the case with this one. This is most apparent in panel 4, where the final section shows that the protein from the perimeter of the ring actually closes as you cut sections further down in the structure. Panels X and Y show cross-sections cutting through the protein ring and membrane perpendicular to the X and Y axes, respectively. From these side views it is clear that a dome of membrane is connected to the upper portion of the protein ring. The red arrowheads indicate the points of attachment between the membrane and the protein. The top of the membrane dome appears to be discontinuous, but this is due to the missing wedge of information that is inherent to the tomographic reconstruction.

### **PSDs isolated at P21 share the same morphological features of those isolated at P60**

There is no obvious difference in the morphology of cryo-preserved PSDs isolated at P21, when compared to those isolated at P60. This was not unexpected based on the silver staining of protein profiles (Fig 2.1) and the tomography of negatively stained PSDs, because there were no obvious differences found there either. They consist of a similar PSD-mesh and a comparable dense layer of protein. Fig. 3.10 shows three PSD isolated at P21. The layout is the same as Fig 3.1 with the four top panels (A-D) representing full projections through the reconstructed volume, and the panels beneath each of them (1-3) representing a 20 nm digital cross-section cut perpendicular to the Z axis. Each cross-section is taken in succession traversing downward through the Z axis. The slices were chosen to illustrate the similar layering to the PSDs isolated at P60. In all of the slices, horizontal arrows point to portions of the PSD-mesh and vertical arrows point to regions of the dense layer. All three PSDs have a crescent of membrane still attached, and they are marked by the letter “M”. Protein rings like those in P60 are also present at P21, and one can be seen in the PSDs in Fig. 3.10 A and B.

Fig. 3.11-3.13 show close-up views of the three cross-sections shown for the PSD in panel C of Fig. 3.10. It is obvious from a closer inspection that there are no major differences in the



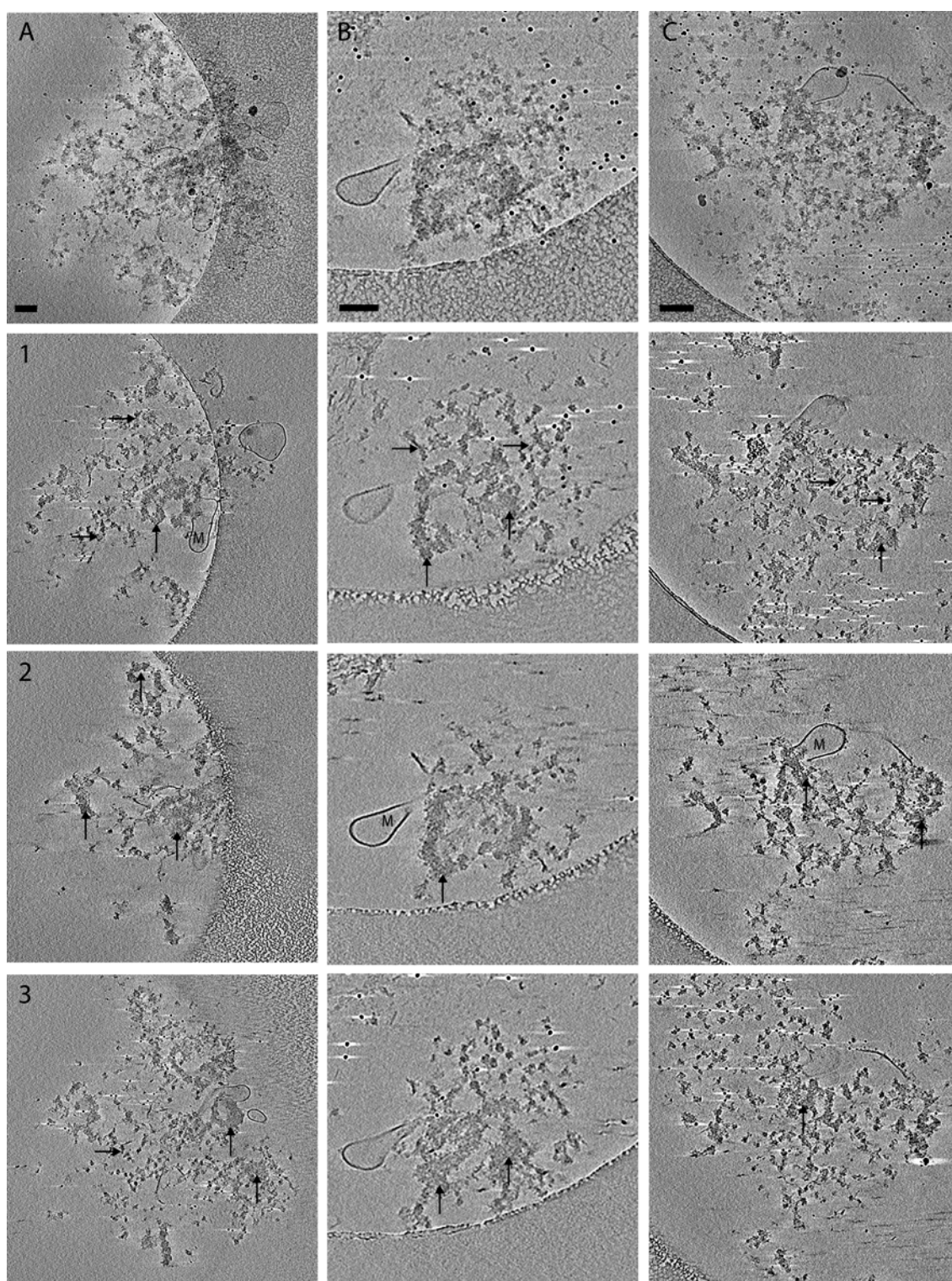


**Fig. 3.10** *Cryo-preserved PSDs isolated at P21.*

(A-C) Representative examples of cryo-preserved PSDs isolated at P21. Lower panels (1-3) are successive 20 nm digital cross-sections through the reconstructed tomographic volume.

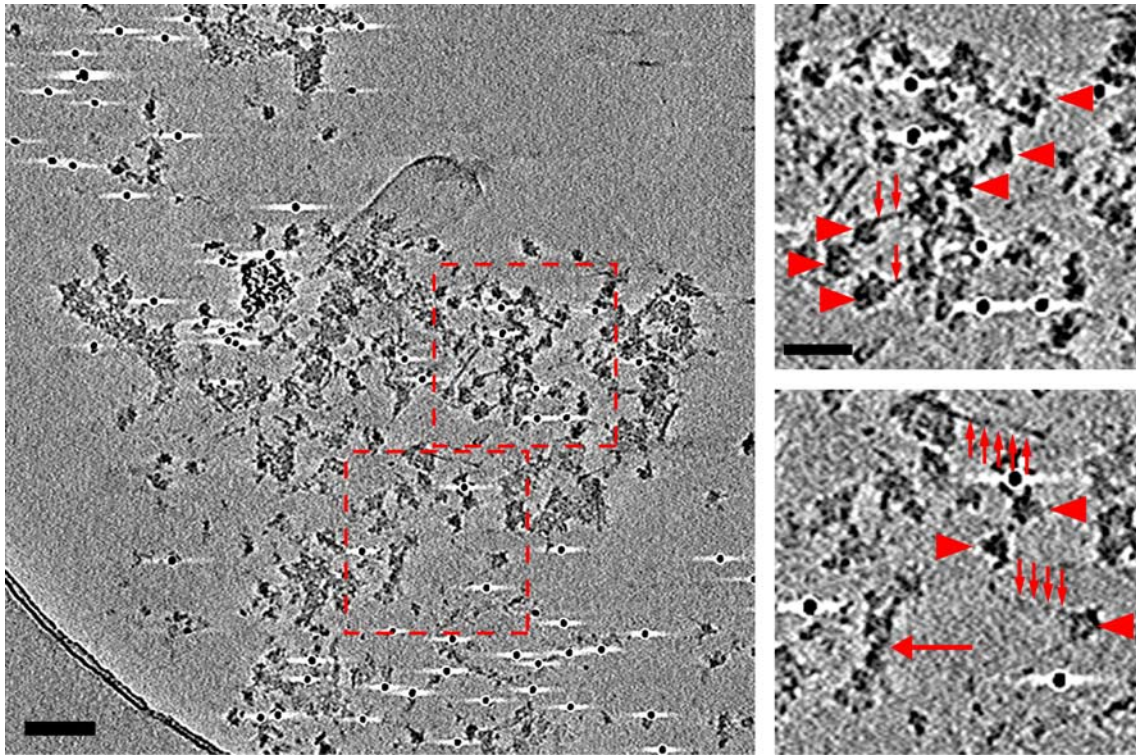


**Fig. 3.11** *PSD-mesh observed in cryo-preserved P21 PSD.*

The left panel is a larger image of the first cross-section shown in Fig 3.10 panel C (scale bar is 100 nm). The red dashed box on the left corresponds to the blow-up in the top-right panel and the dashed-box on the right corresponds to the blow-up in the bottom-right panel (scale bar is 50 nm).

fine morphology of PSDs isolated at P21 and P60. The inset on the top right of Fig. 3.11 corresponds to the upper red dashed box in the left panel, and in it can be seen globular proteins (red arrowheads) connected via thin lateral filaments (red arrows). This is similar to what is seen in the PSD-mesh of PSDs isolated at P60 (Fig 3.2). In this particular cross-section multiple globular proteins can be seen linked together in a row, suggesting that they are held in an organized lateral distribution. The inset in the lower right panel represents the section bounded by the red dashed box in the lower portion of the left panel. This section shows an area with sparsely distributed globular proteins (red arrowheads) and a small portion of the typical PSD-mesh protein strands (horizontal arrow). While the globular proteins appear to be floating freely they are actually connected by very fine filaments, which are indicated by the small vertical arrows. These thin filaments are difficult to see and are often not visible in the cross-sections. They are more clearly visible, however, in the aligned tilt-series as you scroll back and forth through the images.

Fig. 3.12 shows a blow-up of the second cross-section in panel C of Fig. 3.11. It is a mid-level slice that cuts through the portions of densely packed protein like that seen in P60 PSDs. The upper-right panel corresponds to the section of the left panel bound by the red dashed box and the lower-right inset corresponds to the other box. The upper-right panel shows a portion of the dense layer indicated by the vertical arrow and connected to this portion is a detergent resistant membrane. The arrowheads indicate the two points of contact between the membrane and the PSD. These portions of membrane seemed just as abundant at P21 as they were at P60.

Fig. 3.13 shows a blow-up of the third cross-section in panel C of Fig. 3.11. It shows a slice of the PSD just past the layer of dense protein shown in Fig. 3.12. The PSD-mesh and some dense protein are still visible (large horizontal and vertical arrows, respectively) as well as a layer of globular protein extending off the top-left portion of the PSD. A portion of this layer of protein is bounded by the top red dashed box in the left panel, which is blown-up in the



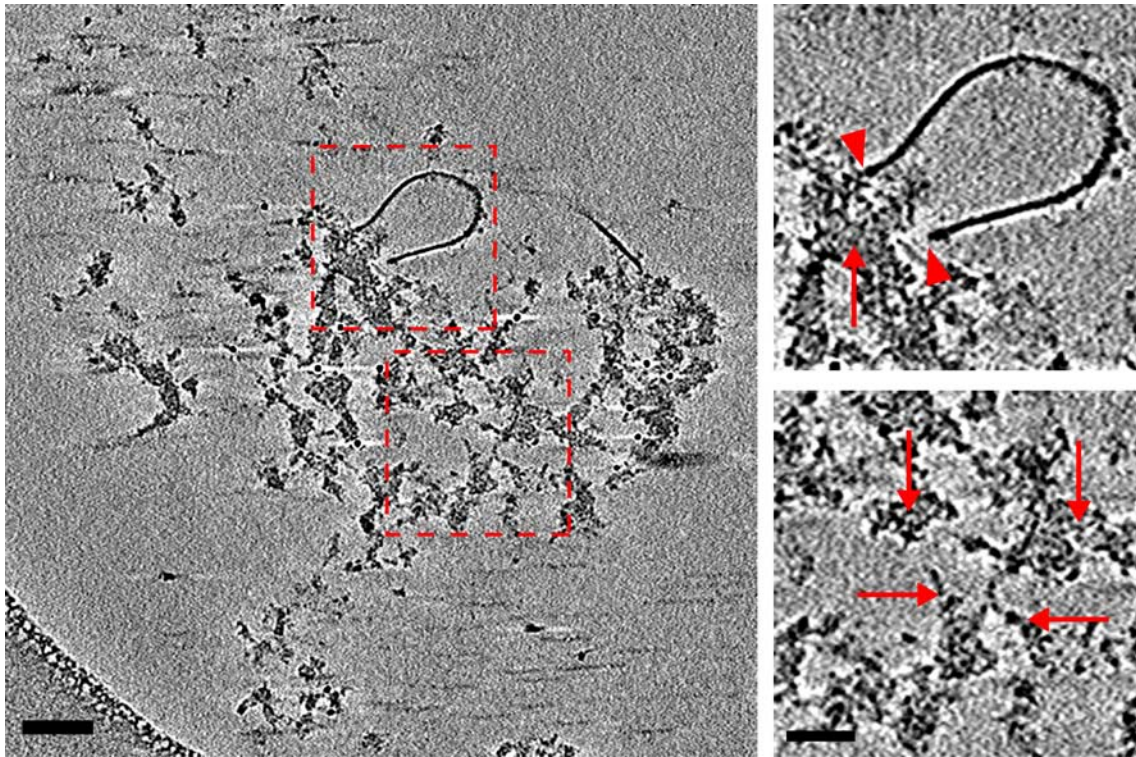


**Fig. 3.12** *Dense protein observed in cryo-preserved P21 PSD.*

The left panel is a larger image of the second cross-section shown in Fig 3.10 panel C (scale bar is 100 nm). The red dashed box on the left corresponds to the blow-up in the top-right panel and the dashed-box on the right corresponds to the blow-up in the bottom-right panel (scale bar is 50 nm).



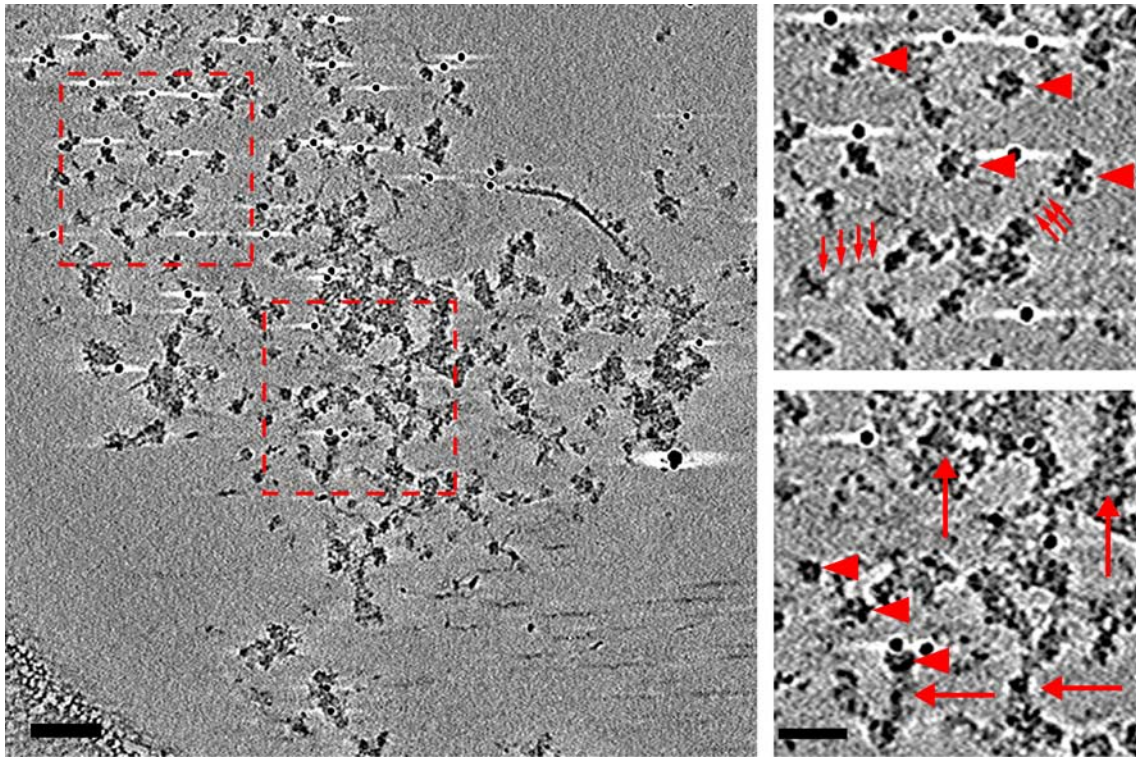


**Fig. 3.13** *Granular network of isolated PSD.*

The left panel is a larger image of the third cross-section shown in Fig 3.10 panel C (scale bar is 100 nm). The red dashed box on the left corresponds to the blow-up in the top-right panel and the dashed-box on the right corresponds to the blow-up in the bottom-right panel (scale bar is 50 nm).

top-right panel of the figure. This network of proteins is relatively thin (~30 nm) and the globular components (arrowheads) are spaced semi-regularly 20-50 nm apart and are linked by thin filaments (small arrows) like those seen in Fig. 3.11. The globular components are ~20 nm across. As mentioned above, these filaments are not always visible in the tomogram. While these globular components are often seen in a thin sheet, they are also seen distributed through the PSD at varying sections along the Z-axis. As seen here, this network of proteins sometimes extends out away from the main portion of the PSD. Nothing of this nature was clearly seen in the negatively stained PSDs. This could be due to the fact that Nanovan is a low contrast stain and such a thin structure is not easily seen, or perhaps the stain disrupts this network of proteins. The lower-right panel corresponds to the portion of the left panel bound by the lower red dashed box. In this blow-up, both dense (vertical arrows) and PSD-mesh (horizontal arrows) are clearly present. There are also a few globular proteins that resemble those seen in the upper panel that can be seen embedded in the protein of the main portion of the PSD. This suggests, again, that these globular proteins are not merely part of a network of proteins that extends out from the edges of the PSD, but can actually be embedded within the PSD itself as components of the organelle. Based solely on morphology it is not clear what these proteins are at this point.

### **PSDs isolated at P2 and E19 are composed almost entirely of PSD-mesh**

Like data from negatively stained PSDs suggested, PSDs isolated at P2 showed obvious morphological differences when compared to PSDs from P21 and P60. In cryo-preserved PSDs the fine morphology of the protein components is better preserved and more direct comparisons can be made since they are free of staining artifacts. What is immediately clear is that the PSDs at this developmental time point are composed almost entirely of proteins that appear similar to the PSD-mesh seen at P60 and P21. Fig. 3.14 is laid out like those above to show the overall morphology of three representative PSDs isolated at P2. Panels A-C show the full projection

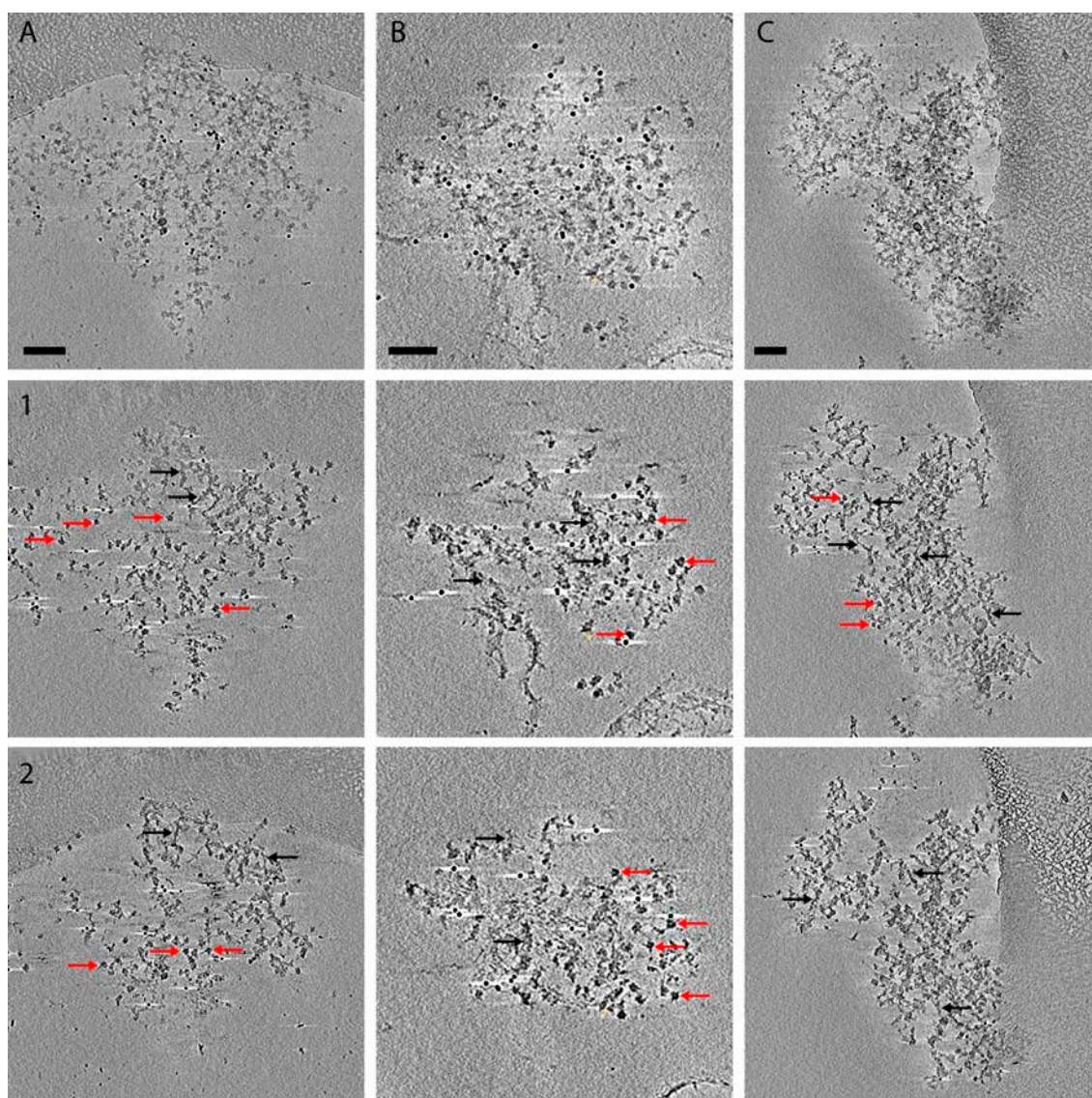


**Fig. 3.14** *Cryo-preserved PSDs isolated at P2.*

(A-C) Representative examples of cryo-preserved PSDs isolated at P2. Lower panels (1-3) are successive 20 nm digital cross-sections through the reconstructed tomographic volume.

images of the three PSDs and the panels below each of them (1-2) show 20 nm cross-sections through the PSD above it. In the cross-sections horizontal arrows point to sections of the PSD-mesh and red arrowheads point to globular proteins that resemble those described in the P21 PSDs. One thing that stands out is that no detergent-resistant membrane was found attached to PSDs at this time point, suggesting that attachment of membrane to the PSD either correlates with the formation of the PSD's dense layer or with changes in membrane composition that do not occur until later in development.

Fig. 3.15 shows a closer view of the two cross-sections shown beneath the PSD in panel A of Fig. 3.14. As in figures above, the two small panels to the right of each of the larger panels (A and B) correspond with that particular cross-section. In both cases (A and B) the upper-right panel corresponds to the portion of the left panel bound by the upper red dashed box and the lower right panel to the lower red dashed box. The sections that are shown in the right panels are chosen to illustrate that the P2 PSDs are composed of both the typical PSD-mesh material (horizontal arrows) as well as the globular proteins (arrowheads) described in the P21 PSDs.

Despite being more irregular with less clearly defined boundaries, PSDs isolated at E19 showed the same fine morphological features as those isolated at P2. The PSDs were composed of a mixture of mesh-like strands of protein and the same globular proteins (at least morphologically) seen at the previously described developmental time points. Fig. 3.16 shows three cryo-preserved PSDs isolated at E19. Just as before, the full projection images are shown in the top panels (1-C) and a cross-section through the same PSD is shown in the panel below. Strands of protein that make up the PSD-mesh are indicated by the black arrows and globular proteins are indicated by the red arrows. As described earlier, the network of globular proteins often appeared to extend outward from the PSD, making it difficult to know where the edge of the PSD really was. Even though this extended network of proteins was seen on occasion in all the previous time points, it was more prevalent at E19. The PSDs in panels A and B are good



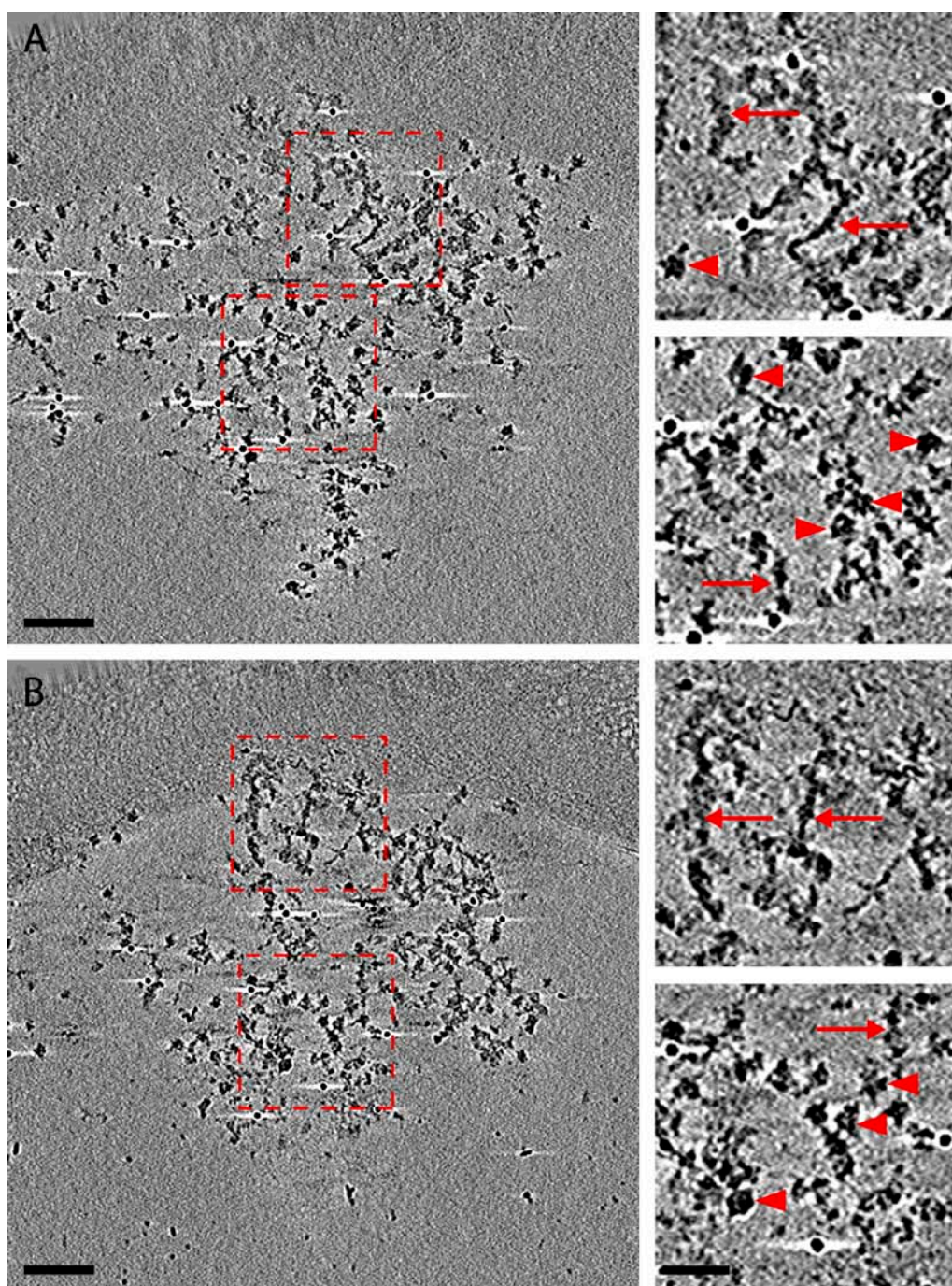


**Fig. 3.15** *Fine morphology of PSD isolated at P2.*

Panels A and B are larger images of cross-sections 1 and 2 (respectively) under panel A of Fig. 3.13 (scale bar is 100 nm). The red dashed boxes in A and B correspond to the areas shown in the two images on the left of each panel. In both cases the upper dashed box corresponds to the blow-up in the upper panel and the lower dashed-box corresponds to the blow-up in the lower panel (scale bar is 50 nm).

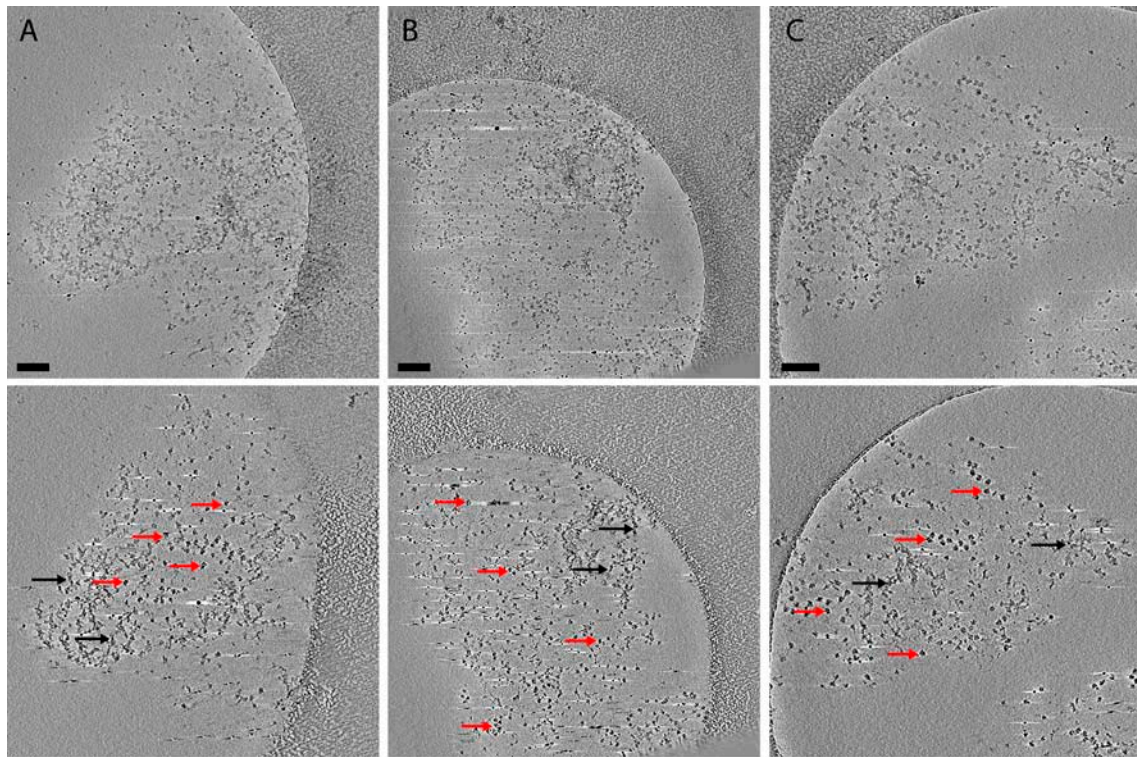


**Fig. 3.16** *Cryo-preserved PSDs isolated at E19.*

(A-C) Representative examples of cryo-preserved PSDs isolated at E19. Lower panels are 20 nm digital cross-sections through the reconstructed tomographic volume.

examples of PSDs with an extensive network of these globular proteins, and Fig. 3.17 provides a closer look at the PSD in panel A of Fig. 3.15. In the larger panel to the left you can see that the portion of the PSD that is mostly composed of PSD-mesh makes up the lower left hand portion of the complex. As you move up and to the right the mesh gives way to a more diffuse granular network of globular proteins such as that shown previously. The upper-right panel is a blow-up of the red dashed box enclosing the area to the left of the large panel, containing the portion of the PSD that is mostly mesh (horizontal arrows). The red arrowhead points to a globular protein that is within the mesh portion. The lower-right panel is a blow-up of the box enclosing the area to the right of the large panel, showing mostly diffuse globular proteins. As in the panel above, the red arrowhead point to globular components. The small red arrows indicate a thin filament bridging the gap between two proteins. While the overall morphology of PSDs isolated at P2 is very similar to those isolated at E19, PSDs from the E19 group seem a little more loosely formed. The edges are not as well defined and the PSD-mesh is not as extensive, however, from visual inspection alone they appear to be made of the same components. This is also suggested by the comparison of silver staining across both time points (Fig. 2.1).



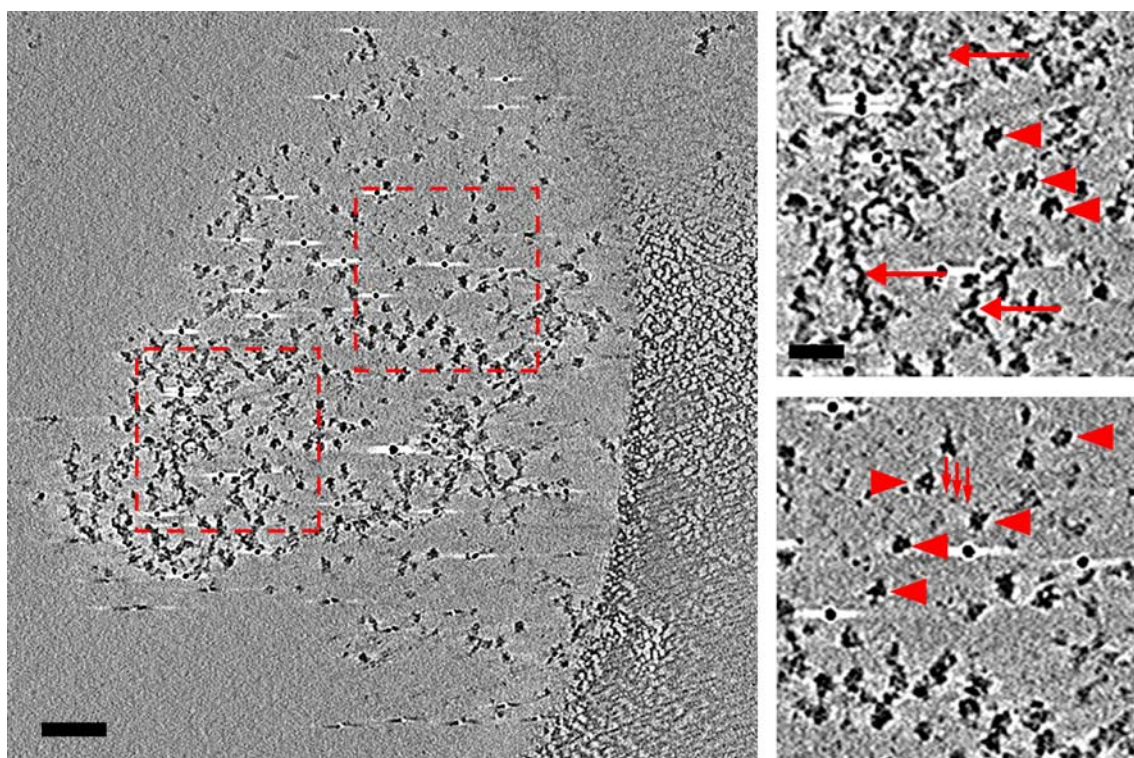


**Fig. 3.17** *Fine morphology of a PSD isolated at E19.*

The left panel is a larger image of the cross-section shown in Fig 3.15 below panel A (scale bar is 100 nm). The red dashed box on the left corresponds to the blow-up in the top-right panel and the dashed-box on the right corresponds to the blow-up in the bottom-right panel (scale bar is 50 nm).



## Discussion

### Why isolate PSDs?

The postsynaptic density is one of the largest and most complex protein assemblies in the mammalian nervous system. Even with no knowledge of its protein composition early neuro-anatomists were drawn to it simply because of its cellular location, where it sits directly subjacent to the postsynaptic membrane at the point of contact between neurons. It is through these contacts that information flows from one neuron to the next and ultimately through networks of cells that are wired together during brain development. Since their discovery the protein composition and function of PSDs have been rigorously studied using a large variety of methodologies and preparations. The isolation method we chose is a modified version of the original protocol developed by Phil Siekevitz's lab (Cohen et al., 1977). The choice was based on the fact that PSDs isolated using Triton X-100 maintains the most protein components when compared to other detergents such as sodium lauryl sarcosinate (Matus and Taff-Jones, 1978). The protocol generates subcellular fractions that enrich in postsynaptic elements such as PSD-95 and glutamate receptors while presynaptic components like SV2 are minimized (Fig. 1.4). Visualization by electron microscopy reveals structures in our preparations that are morphologically similar to PSDs described *in vivo* (Cohen and Siekevitz, 1978; Gray, 1959a; b; Palay and Palade, 1955) as well as PSDs isolated by various groups who have used similar fractions in previous publications (Blomberg et al., 1977; Cohen et al., 1977; Matus and Taff-Jones, 1978; Petersen et al., 2003).

The obvious argument against studying PSDs that have been isolated from brain is that they are no longer in their native cellular environment and it is not known exactly how the isolation process could change them. This is not a trivial concern, and it is not easy to dissuade critics of such an approach. While the overall shape and size of isolated PSDs corresponds nicely with what is seen *in vivo* and the small amount of biochemical evidence available

(Petrálie et al., 2005) suggests they are similar in composition, it is still a question that warrants much more investigation. Unfortunately, it is not a simple question to address for several reasons. One, classical methods for studying PSDs by EM requires that they be cut into thin sections, making it difficult to get a sense of the entire organelle's structure and composition. On top of this, the sectioning process itself can introduce artifacts, and these classical techniques generally require the fixation and dehydration of samples before sectioning takes place. Two, labeling proteins in PSDs that are still inside of the cell is very difficult, because penetrating the membrane of the cell and the tissue itself with antibodies is not a trivial task. This is why tissue must be cut into thin sections to expose antigens to the surface. And finally, the PSD is composed of hundreds of different protein species, making tracking changes in all of them through the isolation process a nearly impossible task. Genetic labeling of proteins with fluorescent probes has been exceptionally helpful in studying the synaptic localization of proteins inside of cells, but the resolving power of light microscopy makes it difficult to determine if a protein is actually part of the PSD or simply localized to the synapse. Because of all these limitations, isolating PSDs provides several distinct advantages. The largest advantage is arguably one of accessibility, because the PSD has been removed from the tightly confined environment of the synapse. Because of this the PSDs become conducive to immuno-labeling methods with the removal of boundaries that make penetration of labeling reagents difficult. In addition to the added accessibility, isolating PSDs allows the study of intact PSDs from an *en face* view. Being able to image the entire PSD lying down flat means that immuno-gold labeling can be used to study the distribution of molecules through the whole organelle, unlike thin sections that only show labeling of a small portion of the PSD. In general, despite the possibility of artifacts produced by isolation, extraction of PSDs provides the ability to more easily observe whole PSDs using current cell imaging technology.

In addition to morphological evidence that isolated PSDs are similar to those seen *in vivo*, there are a number of publications that have documented the various types of enzyme activity still present in the fraction. This provides functional proof that the protein complexes seen are not simply aggregates of denatured proteins, but actually maintain the activity of their enzymatic components. In our own lab, we have performed phosphorylation reactions with PSDs to show that radioactively labeled phosphate is incorporated in a  $\text{Ca}^{2+}$ /CaM-dependent manner (data not shown). Others have also documented the presence of kinase activity as well as ATPase and phosphodiesterase activity (Cotman et al, 1974, Carlin et al., 1981, Kelly et al, 1985).

### **Tomography of negatively stained PSDs**

To the best of my knowledge, these initial studies comparing the three-dimensional morphology of negatively stained PSDs by electron tomography are the first to systematically visualize PSDs isolated at specific time points throughout brain development. Dendritic spines have been well studied during development at the ultrastructural level using EM (Harris et al., 1992), and dynamics of synaptic formation and removal have been characterized both in culture and in living animals using a variety of fluorescent microscopy techniques (Dunaevsky et al., 1999; Majewska et al., 2006; Markus and Petit, 1987; Rakic et al., 1986; Zuo et al., 2005a). Taken together, a model has emerged where synapses are formed in abundance early in postnatal development and are then pruned to form the mature brain. The idea is that an excess of synaptic connections are first established and through a balance of genetic and experience based events, unused connectivity is slowly removed and synapses that are frequently used are strengthened. In order for synapses to strengthen, they undergo a combination of chemical and structural changes ranging from the modification of existing receptors and insertion of new ones (Barria and Malinow, 2005; Benke et al., 1998; Bredt and Nicoll, 2003; Collingridge, 2003; Malenka and Bear, 2004) to the remodeling of dendritic spines (Sorra and Harris, 1998).

While dendritic spines have been well studied, changes in the PSD have been not been documented. Because the PSD is such an integral component of synaptic function it is imperative to understand the structure of the PSD as well as its ability to change. PSDs are clearly present at synapses as early as P2 (Petrulia et al., 2005) and while they are less abundant during prenatal development they have been documented in thin sections of brain as early as E19 (Itarat and Jones, 1992). As mentioned above, isolating PSDs does remove them from the cellular context, but it also provides the opportunity to image the intact organelle from an *en face* view. In addition, this makes them amenable to electron tomographic analysis, thus permitting highly detailed 3D visualization of the entire complex. By using such an approach, distinct morphological characteristics were evident between PSDs isolated before birth (E19) and during early postnatal development (P2). By P21 the overall structure of the PSD seems to have stabilized and no distinguishable morphological features were evident between PSDs isolated at P21 and P60. The tomographic reconstructions suggest that early in development (E19) the majority of PSDs are characterized by a lattice-like matrix of protein. The idea of a postsynaptic lattice is not new, however. Previous studies have reported what appeared to be an underlying mesh within the PSD (Gulley and Reese, 1981; Landis et al., 1987; Matus and Taff-Jones, 1978; Petersen et al., 2003). In fact, Matus and Taff-Jones (1978) reported the appearance of mesh-like PSDs when they isolated them using an alternate detergent during extraction. They showed that PSDs isolated with deoxycholic acid were stripped of more protein and revealed an underlying lattice-like structure that they suggested represents the frame upon which the rest of the PSD was built (Matus and Taff-Jones, 1978). By two days post-natal the protein matrix is still visible but a little less prominent, presumably due to the PSD filling out via the recruitment of new protein components. Three weeks post-natal (P21), the lattice structure evident during early development becomes difficult to discern, and the appearance of structures such as dense rings of protein as well as large areas of densely packed

protein are typical. The same structural characteristics are seen in PSDs isolated at P60 suggesting that by P21 the majority of large structural changes have already occurred.

While the ultra-structure of isolated adult PSDs has been observed previously (DeGiorgis et al., 2006; Petersen et al., 2003), they are not directly comparable as they were prepared for EM analysis using platinum shadowing as opposed to negative stain used here. Nevertheless, similarities and differences were observed. Platinum shadowing, like that used by Petersen et al. (2003) highlights the features unique to each side because the platinum is only deposited on the exposed side of the PSD, while negative stain penetrates the PSD, which makes differences between each side of the PSD less apparent. Despite this major difference, they were still able to see fine filamentous proteins running through the PSD much like those described by our approach. They did not observe the protein rings which we see in adult PSDs and this is presumably due to the platinum's inability to penetrate the PSD. In this sense, negative stain appears to have an advantage over the platinum shadowing technique. One more similarity is that we both observed fragments of detergent-resistant membrane still attached to the isolated PSDs. With respect to the PSDs isolated earlier in development (E19, P2 and P21) there is no previously published work with which to compare our results.

### **Compositional changes during development observed by immuno-gold labeling**

In addition to the structural changes observed through development, immuno-gold labeling of PSDs revealed distinct compositional changes associated with each stage of development. While not an entirely novel finding, it was interesting to see that not all PSD components are present early on in development. Specifically, the scaffolding protein PSD-95. Petralia et al. (2005) showed that there was very little detectable PSD-95 in PSD fractions collected from rats two days postnatal, however, they made this conclusion via western blots of PSD fractions and thin sections of PSDs in fixed tissue. Quantification of PSD-95 in intact PSDs provides direct evidence for its near absence in early developmental stages of the

organelle, and suggests that it is not critically involved in the initial stages of PSD formation. If early PSDs do not contain this scaffolding molecule then it would not be a good molecular marker for synapses containing PSDs in early stages of development. In this case, postsynaptic densities in early stages of development may be missed by using antibodies against PSD-95. This also suggests that PSD-95 is not required for the initial clustering of NMDA receptors within postsynaptic densities, which supports previous findings (Migaud et al., 1998; Passafaro et al., 1999).

The high level of labeling for  $\alpha$ -actinin early in development, was interesting because it makes  $\alpha$ -actinin a likely candidate as one of the core components of the PSD. Because of its ability to cross-link cytoskeletal elements it is probably involved in establishing the protein lattice described above. The observation of high labeling levels for  $\alpha$ -actinin fits nicely with current data that shows  $\alpha$ -actinin can interact with both NMDA receptors and CaMKII (Leonard et al., 1999; Merrill et al., 2005; Robison et al., 2005b), which would allow it to act as a point of recruitment for these molecules within the PSD. There is a network of interactions that can occur between  $\alpha$ -actinin, NMDA receptors and CaMKII. CaMKII has distinct binding sites for both  $\alpha$ -actinin and the C-terminal tail of the NMDA receptor, and the NMDA receptor subunits NR1 and NR2b each have separate sites that bind  $\alpha$ -actinin and CaMKII. Through these multiple binding sites a ternary protein complex can be formed (Merrill et al., 2005; Robison et al., 2005b). When multiple interactions occur between molecules in a complex like this the stability of the complex is increased which would make sense seeing as how resistant the PSD is to disruption during isolation. Presumably extensive binding between proteins occurs throughout the entire PSD. One well recognized role for  $\alpha$ -actinin is its ability to bind to and cross-link actin filaments. Because of this,  $\alpha$ -actinin likely acts as an attachment point for actin filaments often seen projecting from the PSD into the cytoplasm of dendritic spines (Cohen and Siekevitz, 1978; Rostaing et al., 2006). It is also possible that the actin itself is

involved in the formation of the underlying PSD mesh, and this is why  $\alpha$ -actinin is present in the PSD even early in development. Of course, further immuno-labeling experiments for actin and other cytoskeletal components will be pursued in future studies.

The labeling density for NMDA receptor subunits NR1 and NR2b changed in concert across all four time points. Both peaked at P21 and then came back down by P60. The NR1 subunit is required for the assembly of a functioning NMDA receptor, and the NR2b subunit is important for synaptic plasticity early in development (Barria and Malinow, 2005; Sheng et al., 1994). The CaMKII binding domain in NR2b's C-terminal tail allows it to recruit CaMKII to the PSD (Gardoni et al., 1998; Shen and Meyer, 1999). This interaction is critical for long term potentiation and it is hypothesized that the switch from NR2b to NR2a (which has lower binding affinity for CaMKII) is a mechanism for regulating synaptic plasticity (Barria and Malinow, 2005). Even though our data show an increase in NR2b over time it does not rule out that the ratio of NR2b to NR2a may have still gone down and further experiments to assess this developmental switch in NMDA receptor subunits is required to speak to this issue directly.

Recent work has shown that GluR1 containing AMPA receptor complexes account for approximately 80% of receptors at CA1 synapses in the hippocampus (Lu et al., 2009), which makes the low levels of GluR1 at all time points a bit surprising. This low labeling in isolated PSDs suggests that perhaps a sub-population of the AMPA receptors at postsynaptic sites is not stably anchored within the framework of the PSD (and dissociates during the isolation process), which is consistent with theories about the rapid cycling of AMPA receptors at synapses (Ehlers, 2000; Lee et al., 2004; Malinow and Malenka, 2002).

The high level of  $\alpha$ CaMKII in PSDs at P60 was expected as several previous studies have quantified its abundance (Chen et al., 2005; Petersen et al., 2003), but the nearly equal labeling of  $\beta$ CaMKII was a surprise. Normally  $\alpha$ CaMKII is thought of as the PSD enriched isoform, but looking at the Western blots in Fig. 1.5 it would appear that, if anything, the  $\beta$  isoform is more

enriched relative to the amounts seen in homogenate and the synaptosomal fraction. In the brain, CaMKII is a dodecameric holoenzyme composed of mixtures of both  $\alpha$  and  $\beta$  subunits and so targeting of one or the other subunit would be expected to also carry its partner into the PSD. However, one major difference between the two isoforms is  $\beta$ CaMKII's ability to directly bind actin (Fink et al., 2003; Ohta et al., 1986; Sanabria et al., 2009; Shen et al., 1998). Because of this, perhaps  $\beta$ CaMKII is involved more in regulating the interface between the PSD and the actin cytoskeleton in the spine, while  $\alpha$ CaMKII regulates PSD structure through interactions with its many binding partners (e.g.,  $\alpha$ -actinin and NMDA receptors). Consistent with this observations is that  $\beta$ CaMKII is known to regulate spine growth (Fink et al., 2003; Lin and Redmond, 2008; Okamoto et al., 2007), a process that is highly dependent on alterations in the actin cytoskeleton. It is also interesting to note that by P21 and through P60 the labeling density for CaMKII is equivalent to that of the scaffolding molecules PSD-95 and  $\alpha$ -actinin, suggesting that it too is playing a structural role in the PSD. The unique structure of CaMKII (Kolodziej et al., 2000) suggests that it could be capable of binding multiple partners at the same time through its radial distribution of subunits, which makes it a likely candidate for organizing local signaling modules within the PSD. Through binding to the NMDA receptor it would position CaMKII near the incoming  $\text{Ca}^{2+}$  current through the receptor's ion channel, providing precise regulation of the kinase's activity and its interactions with various binding partners and enzymatic targets.

Except for CaM all of the other proteins studied increased in their abundance through development. This indicates that an increase in amount is not a rule for all proteins in the PSD. The most direct explanation for the increased abundance of CaM early in development is that synapses at this stage may depend more heavily on the  $\text{Ca}^{2+}$ /CaM-signaling pathways than synapses that have attained a mature state. One possibility is that as CaM-dependent proteins are recruited into the PSD and become integrated with their various binding partners, their



activity is no longer entirely dependent on CaM so CaM is no longer required in such abundance. Indeed, CaMKII activity has been shown to be regulated by binding to both the NMDA receptor subunit NR2b and  $\alpha$ -actinin, two PSD components thought to mediate recruitment of the kinase into the PSD (Robison et al., 2005a). Alternatively, it is possible that because CaM can increase or decrease the affinity of specific molecular interactions that it is involved in promoting certain binding events while inhibiting others during early stages of PSD assembly. Two well documented examples of this are seen in  $\text{Ca}^{2+}$ /CaM's ability to negatively regulate  $\beta$ CaMKII binding to actin (Ohta et al., 1986) as well as its ability to displace  $\alpha$ -actinin from the intracellular tail of NR1, thus promoting CaMKII binding to the NMDA receptor (Merrill et al., 2007). This is an interesting and exciting prospect as it involves CaM differentially regulating steps of PSD assembly in a development-dependent manner.

It is important to note that the use of immuno-gold labeling is not a pure quantitative method for determining the abundance of a protein within the PSD. Because of different labeling efficiencies between antibodies and the potential of buried epitopes in the confinements of the PSD, it is not possible to make definitive quantitative comparisons between proteins labeled by different antibodies. That being said, for each antibody in these studies, titrations were done to find a concentration that resulted in a near asymptotic average labeling density. This was done to maximize labeling of the available binding sites. It is also important to note that the labeling densities presented here are average labeling densities, meaning that individual PSDs in each group showed labeling densities that could be significantly higher. This suggests that the asymptotic average labeling densities are not reached simply because the antibodies ability to detect more signal has been saturated.

### **Spatial distribution of immuno-gold labeling**

Results from the RKF analysis of immuno-gold labeling indicates that all of the proteins studied show a non-random distribution within the PSD. Seeing that this held true across all

four time points of development, it seems logical to conclude that the PSD is assembled following a series of non-random processes. Because only single molecular species were labeled in these experiments it is not clear what non-random means specifically. I can conceive of multiple ways that proteins could be non-randomly distributed. Proteins could be regularly or randomly distributed within sub-regions of the PSD as described for CaMKII (Petersen et al., 2003) or they could be clustered together through shared protein-protein interactions. For example, several NMDA receptors could be clustered near one another through interactions with the same CaMKII holoenzyme. Non-randomness can also be achieved by a regular distribution in a lattice-like pattern. In this case the proteins are not clustered, but they are non-random. With the present form of the analysis I am not able to differentiate between various types of non-randomness, but simulated non-random distributions are being used to look for potential signatures in the RKF plot that may suggest a specific type of distribution (this is discussed further in the Appendix). As mentioned above, labeling was done only with single molecular species so co-localization of molecules could not be assessed in this study. However, quantifying spatial relationships between pairs or groups of molecules will be essential to understand the series of protein interactions that are used to assemble the PSD. To better address such spatial relationships and the modular organization of proteins in the PSD future studies will require multiple labeling of various combinations of proteins with different sized gold balls.

### **Cryo-tomography of isolated PSDs**

As of now, there is no description of cryo-preserved PSDs in the literature, so the work presented here is entirely novel and largely exploratory. The level of detail preserved in vitrified PSDs was remarkable compared to negatively stained and platinum shadowed PSDs (DeGiorgis et al., 2006; Petersen et al., 2003), which is due to the fact that contrast in cryo-preserved specimens is generated directly by the sample density instead of by the addition of a

chemical stain. Despite the major differences, there are enough recognizable features conserved between stained and cryo-preserved specimens to positively identify them in the vitrified state. Because P60 PSDs provided the most structurally rich organelle (based on stained data), and because they represent the most mature form of the PSD they were the first to be studied in the vitrified state. Major morphological features such as the dense protein rings and bands of protein were similar in both cryo and stain data. While the PSD-mesh was less apparent in the stained data it was visible in some areas and the general morphology of the mesh was conserved between the two preparation techniques. The fine detail of the PSD mesh components was strikingly pronounced in the cryo-preserved P60 PSDs and the presence of a large variety of components was observable. This increase in detail is a testament to the superior sample preservation and imaging capabilities under cryo conditions. It is clear from the cryo-preserved P60 PSDs that there are at least two macroscopic classifications of protein structure within the adult PSD. There is both a loosely packed meshwork of protein, which has been described here as the PSD-mesh and a portion of densely packed protein that generally lies toward one side of mesh, but can span the entire thickness of the PSD in places.

The same general features were present in P21 PSDs, but going back to P2 reveals that the majority of PSDs during early postnatal development are composed of only a PSD-mesh that is largely indistinguishable from that seen in later stages of development. At E19 PSDs are very lacey with portions that resemble the PSD-mesh as well as extensive networks of semi-regularly spaced globular proteins. This suggests that the PSD-mesh is an early component of the PSD and the layers of dense protein that are seen later in development are assembled through the recruitment of new protein into the existing framework established by the PSD-mesh. Without tracking the development of individual PSDs we cannot conclude with absolute certainty that the dense layer is built within a PSD-mesh built earlier in development. It is possible that synapses formed early in development with mesh-like PSDs are replaced by new

synapses with more mature PSDs. However, at least by morphological criteria, the mesh seen early in development appears identical to that seen later in development, and it seems unlikely that all PSDs formed early in development would be completely replaced by new ones containing the more densely packed components. Live-cell fluorescent microscopy experiments do support the notion of gradual recruitment of PSD components to the synapse during development (Bresler et al., 2004), which fits nicely with observations here that PSDs early in development are built of a mesh-like scaffold that is filled in over time.

It is not clear which molecules make up the PSD-mesh. From my immuno-gold labeling,  $\alpha$ -actinin is a potential candidate considering relatively high labeling early in development. It makes sense considering its ability to bind integral PSD components such as  $\alpha$ CaMKII and NMDA receptors (Merrill et al., 2005; Robison et al., 2005a; Robison et al., 2005b) as well as the cytoskeletal protein actin (Blanchard et al., 1989), which is often seen in direct contact with the PSD (Cohen and Siekevitz, 1978; Rostaing et al., 2006). There are small filaments seen in the cryo-preserved PSDs that resemble the rod-shaped structure and dimensions (35 nm) of the dimerized form of  $\alpha$ -actinin (Tang et al., 2001). However, these small filaments could also correspond to a number of proteins since there are many scaffolding proteins in the PSD such as the MAGUK family (PSD-95, PSD-93, SAP-102, chapsyn-110), shank and homer (Petralia et al., 2005). It is also likely that the PSD-mesh is, in part, made of cytoskeletal proteins such as actin and tubulin, as both of these proteins are well documented as components of PSD fractions (Dosemeci et al., 2007; Li et al., 2004; Peng et al., 2004; Walikonis et al., 2000; Yoshimura et al., 2004). However, there is no obvious actin or tubulin filaments in the PSDs observed here based on traditional morphological standards. It is possible that they do not form long filaments or microtubules like they do in the cytoplasm and only make short connections between various proteins within the PSD. So far, it is still not known what the core component of the PSD-mesh is, or if there is a single core component at all. The strands of protein seen in

the mesh don't appear to be made of a single repeating structure, but instead look like a complex mixture of filamentous and globular proteins. The 45 and 25 kDa bands seen by silver staining (Fig 2.1) would be a good place to start in terms of identifying core components.

CaMKII is a major component of the PSD. Without immuno-labeling CaMKII in cryo-preserved PSDs it is not possible to definitively identify holoenzymes within the complex. However, the detail provided by cryo-tomography already reveals PSD components that resemble CaMKII morphologically. The globular network of proteins shown in figs. 3.13 and 3.14 contain protein complexes of the right size (~20 nm across). Depending on the angle, they often show small protrusions from the core that resemble the radially distributed catalytic domains of the holoenzyme. As mentioned in the results, seemingly identical particles exist throughout the PSDs and not only within these globular networks. They are typically easier to see early in development, but they are visible at all time points. Perhaps this is because as development progresses, and the dense layer of the PSD is built, these complexes (assuming they are CaMKII) are integrated into the structure of the PSD and obscured via interactions with newly recruited protein components. This would be consistent with a structural role for CaMKII by which its multivalent binding sites function to organize multiple binding partners into local signaling modules within the PSD.

Besides the dense layer of protein observed in later development (P21 and P60), the most obvious difference between early and late developmental PSDs is the presence of detergent-insoluble membrane still attached to isolated PSDs. These patches of membrane most likely represent lipid rafts, which are typically resistant to solubilization by cold Triton X-100. Lipid rafts are portions of the plasma membrane that are enriched in cholesterol and sphingolipid composition. This differential composition generates a more ordered, less fluid, portion of membrane that can function as a membrane microdomain capable of clustering molecules at the cell surface. Dendritic raft fractions have been isolated from synaptic plasma membranes, and

they appear virtually identical to the membrane seen in our PSD fractions (Suzuki et al., 2001). In fact, when compared to PSD fractions derived from the same synaptic plasma membrane, many PSD components are shared across both fractions (Suzuki et al., 2008), suggesting that these rafts are involved with PSDs somehow. Interestingly, in the same study, rafts associated with CaMKII were shown to become resistant to disruption by methyl- $\beta$ -cyclodextrin (M $\beta$ CD), which normally removes cholesterol. This could explain why detergent-resistant membranes seen in contact with our PSDs were not solubilized by treatment with M $\beta$ CD (preliminary data not shown). Given the lipid raft's important role in regulating signal transduction at the cell surface, it makes sense that they might be associated with PSDs (one of the most complex signal transduction machines known). The abundance of AMPA receptors found in dendritic raft fractions (Suzuki et al., 2001), suggests that they may play a role in sequestering or recycling AMPA receptors at the postsynaptic site. Presumed lipid rafts have been described in isolated PSDs before (Petersen et al., 2003), and our observations suggest that its presence is developmentally regulated. In fact, it does appear to be most often associated with the dense layer of PSD protein typically seen only by P21. Although it is sometimes connected via the PSD-mesh, it is still likely regulated by proteins recruited later in development since it was never seen in contact with the PSD-mesh of E19 and P2 PSDs. Further experiments are needed to determine what makes these membranes detergent-resistant, but the presence of protein rafts would carry significant biological importance, seeing as how they play critical roles in regulating cell signaling pathways (Simons and Toomre, 2000). Because of this the composition of these detergent-resistant membranes will be the focus of future studies.

### **PSD Assembly**

It is impossible to speak directly about the assembly of PSDs using the data gathered for this thesis, because I have captured only snap-shots of PSDs isolated at different stages of development. To truly understand assembly it will be necessary to follow an individual synapse

throughout its lifetime, and at this point it is impossible to do this at the level of resolution needed to observe something as small as the PSD. That being said, I still believe the studies presented here do provide insight to PSD assembly, regardless of the exact mechanism of assembly. Some have proposed that the PSD is fashioned from pre-formed complexes that are trafficked to developing synapses (Prange and Murphy, 2001; Washbourne et al., 2002) and others believe it is built sequentially through the recruitment of individual PSD components over time (Bresler et al., 2001; Bresler et al., 2004; Friedman et al., 2000; Rao et al., 1998). While I tend to agree with the latter, I am not capable of saying definitively which hypothesis is correct. It is possible that both are correct, or that smaller signaling modules are built and then delivered pre-assembled. What does appear to be true, from my data, is that the components of the PSD-mesh that are seen early in development are still present later in development once the PSD has matured. Whether this PSD-mesh is the same mesh built earlier in development is not easy to know. Perhaps the more mesh-like PSDs seen early on are completely replaced later on by a more mature PSD, and maybe the components of the mature PSD are built into an existing mesh. Either way, the dense components of the late PSDs are obviously integrated within a PSD-mesh, lending strong support to the idea that the mesh is used as a scaffold for the assembly of later components. It is possible that the mesh is brought to the synapse pre-assembled and then the later components are recruited individually. This model could reconcile the differences that have been observed at the light level in the studies referenced above.

### **Summary and Future Direction**

The results of this study illustrate that the three-dimensional structure of PSDs isolated at different times during development exhibit distinct morphological and compositional characteristics. While this may not be surprising, this is the first time that PSDs isolated at various stages of development have been visualized and compared at the ultrastructural level. This means that while dendritic spines are undergoing structural changes in response to

development or synaptic activity, these changes are likely accompanied by alterations in the structure and function of the PSD. While no two PSDs are exactly alike there are general morphologies that are shared, and it appears that by P21 the majority of PSDs in rat forebrain are structurally mature by morphological criteria. The first observation of cryo preserved PSDs in tomographic reconstructions is reported here and provided insight into both the formation and fine detail of the PSD's morphology in a frozen-hydrated state. As expected with structural changes, there are also accompanying changes in protein composition as shown by immuno-gold labeling of individual PSD complexes. While it is often assumed that the PSD plays an organizational role at the synapse, this assumption is largely intuitive and there is only a limited amount of data to support it (Petersen et al., 2003; Valtschanoff and Weinberg, 2001). The eight different proteins analyzed in this study all show non-random distributions at each time point through out development, providing strong evidence for a systematic and organized assembly of the PSD. Admittedly, this is a small sampling of the over 100 protein components now thought to compose the PSD (Dosemeci et al., 2007; Dosemeci et al., 2006; Jordan et al., 2004; Li et al., 2004; Peng et al., 2004; Walikonis et al., 2000; Yoshimura et al., 2004) so there is still much work to be done to fully understand this organization and how exactly it supports synaptic function.

When this project started, the original goal was to understand the structural arrangement of molecules within the PSD. Initially this meant: where are the molecules located, how are they oriented within the complex and which molecules are they interacting with? This is obviously no small task considering that the PSD is composed of hundreds of proteins, and depending on its developmental stage and activation history, it could reside in any number of structural states. I knew back then (but it is painfully obvious now) that to answer these questions it will demand a variety of approaches and probably an entire lifetime. Nevertheless, I can't think of a more



important question in cellular neuroscience, and it is my hope to return to these questions one day with an arsenal of tools at the ready.

From the bottom-up, it is imperative that we know the structure of the individual components and how these structures change when interacting with various binding partners. Indeed, it was part of my original plan to do single particle reconstructions of CaMKII bound to other PSD components (i.e. NR2b, Densin-180 and  $\alpha$ -actinin to name a few). It is critical to see these interactions at a high resolution in order to understand the effect of their interactions on one another as well as geometric constraints that could govern their assembly into a larger complex. Perhaps CaMKII is altered in a way that would make it difficult to recognize when searching for it in whole PSDs? Knowing where other proteins bind to CaMKII and their orientation with respect to one another will provide critical insight to how the kinase is oriented within the PSD, which is completely unknown at this point.

From the top-down there is still much work to be done. To identify individual components within the PSD, I believe it is necessary to label them in a cryo-preserved state, and to do so as directly as possible. This would mean reducing the size of the gold label and conjugating it directly to primary antibodies or antibody fragments. The detail gained by cryo-preserving PSDs is stunning, and would allow tagged components to be visualized directly. At this point, the potential for obtaining higher resolution reconstructions of PSDs is very real. Decreasing the angular step during collection of the tilt-series is an obvious first step, followed by an increase in magnification and optimization of the defocus. These are simple steps that can be taken without the need for expensive upgrades to the microscope, such as the addition of an energy filter. With an energy filter, however, useful information could be gained at higher tilt angles (when the specimen becomes very thick). Even without these changes though, there is a wealth of information to be gained from simply collecting more tomograms. With the uniqueness of each PSD it is just as important to fully document the differences seen across

many PSDs as it is to document their similarities. Since no one has really characterized them in the cryo-preserved state, there is much room left for exploration.

Going beyond the structure alone is also important. I mentioned that I set out to study the arrangement of molecules in the PSD, but it was under the assumption that this arrangement served some logical purpose in terms of function. Most people believe that the PSD organizes signaling molecules so that intracellular signaling pathways are spatially confined to increase the efficiency and specificity with which they activated and regulated. Naturally, an understanding of the PSD's molecular architecture should be complimented with studies of its function, so as to make sense of the structure. Considering CaMKII's role in synaptic function and plasticity, it is a natural first candidate for such experiments. What is the purpose for CaMKII's recruitment to the PSD? We know that it's not purely structural as CaMKII is responsible for phosphorylating and regulating several key targets such as NMDA and AMPA receptors as well as itself in an autophosphorylation process that is essential for synaptic plasticity and learning (Giese et al., 1998). It has been hypothesized that the PSD functions as a biochemical boundary within the spine and that once CaMKII is recruited into its machinery, the kinase is regulated differentially compared to the cytosolic pool of CaMKII (Lisman and Zhabotinsky, 2001; Miller et al., 2005). Because of this, understanding how the PSD functions to regulate CaMKII is very important and should be the focus of future studies. In a bottom-up fashion, purified PSD components should be mixed together *in vitro*. If it is possible to reconstitute some PSD-like structure or even individual signaling modules, the door will open to study processes of PSD assembly and to more precisely probe the effect of assembly on the function of the individual components.

To understand how molecules in the PSD are arranged into local signaling modules is imperative to making sense of the structure/function relationship. With immuno-gold labeling protocols in place and spatial analysis methods worked out, it is important to pursue multi-

labeling experiments that will shed light on the spatial relationship between sets of proteins. These experiments will go beyond conclusions of simply random or non-random distribution, and begin to really define the potential interactions that are holding the PSD together. Information gained from this type of experiment could help lead experiments using purified PSD components described in the previous paragraph.

Of course to really understand the PSD means not only to know its structure and the functional purpose of its organization, but also how this structure and function can change. The PSD is dynamic and almost certainly at the heart of physiological plasticity (i.e. LTP and LTD). We know its protein composition changes greatly in an activity-dependent manner (Ehlers, 2003) so we will need to know how these changes effect the structure and function of the PSD if we are to understand the molecular mechanisms underlying plasticity at the synapse. This will not be an easy task, but the ability to isolate PSDs from hippocampal slices will allow us to study PSDs subjected to various pharmacological agents that increase or decrease activity. This also affords the opportunity to study the effect of kinase/phosphatase inhibitors on the structure of the PSD and the phosphorylation state of CaMKII. The possibilities are seemingly endless when you think of all the different components that make up the PSD. To have a full understanding of each components role and how it contributes to changes over time or in the face of synaptic activity is a major undertaking and will require many talented individuals using an array of different approaches. This is why it is important to define local signaling modules that exist within the PSD, because these would be much more manageable to focus on. The molecules studied in this thesis are a good starting point for such a set of experiments.

Finally, isolating PSDs has afforded me to study the organelle in an intact state, without fixing and slicing it using classical methodology. However, the question of how removing the PSD from the cell changes its properties will always be up for debate, and will remain unanswered until we actually know how it compares to the organelle *in vivo*. This was certainly

a consideration from the beginning and we have made strides in this direction using cryo-preservation of cultured neurons grown on EM grids. While finding synapses has proven to be difficult, this type of approach is critical to discovering the nature of the PSD's structure inside of the cell, where it is still in contact with the postsynaptic membrane and the cytosolic actin network.

## **Appendix: Spatial Analysis of Gold Label Distributions**

One of the most difficult questions to answer is “how is the PSD built” meaning how are the molecules arranged to build such a large protein complex? The sheer number of different proteins (more than 100) that come together to form the PSD, along with the hugely complex network of protein interactions, makes it very difficult to dissect the arrangement of molecules in the organelle. It is generally believed that there is a systematic organization to the distribution of molecules through the PSD. Otherwise, why would hundreds of different proteins be sequestered to such a small region of the cell? Arguably the molecules could be packed into a small volume merely to maximize the chance of proteins from various signaling pathways finding each other in a timely manner by limiting the diffusional distance between them. If this were true, and diffusing molecules were simply trapped within a defined region of the synapse, it would be difficult to imagine being able to isolate the PSD through subcellular fractionation. Presumably, the insolubility of the PSD by the detergent Triton X-100 is indicative of a protein complex that is held together via an extensive network of protein-protein interactions.

So how does one begin to answer the question of the PSD’s molecular architecture? No two PSDs are identical, because they come from synapses that are from various cell types and each synapse has a different activation history. As mentioned above, this uniqueness makes them unamenable to high-resolution (sub-nanometer) imaging techniques that take advantage of similarities by averaging multiple structures. Even if sub-nanometer structures of PSDs were achieved, it is not clear that individual components would be recognizable as they would likely be in complex with various binding partners that could either occlude or alter their normal structure. Because of this, it is imperative to employ some type of protein labeling method to identify the location of individual molecules within the PSD. Since immuno-gold labeling was

used to track changes in the protein composition of PSDs, the location of the gold balls could also be used to study the spatial distribution of molecules within the complex.

To do this there are several key hurdles to overcome. The first hurdle is that of boundaries, because the PSD is a relatively flat organelle that only covers a finite amount of space. Therefore, the edges of the PSD represent a boundary that limits the distribution of gold labeling, and this limitation can cause artifacts when using conventional spatial analysis methods that analyze a finite space but assume the distribution continues indefinitely. The most ideal method for defining the boundary would be to trace the exact outer edge of each individual PSD, but since the edges of each PSD can vary significantly in their composition (i.e., smooth and well defined, rough/jagged or filamentous) it is not only extremely time consuming but highly subjective at times. In order to avoid these disadvantages the method chosen was to calculate a convex hull that surrounds the distribution of gold balls on each PSD (Fig. 2.17). By definition a convex hull is a polygon that surrounds the entire distribution of points in a set with the fewest number of vertices possible, while the vertices are generated by the outer most points in the dataset. This method for defining the boundaries of the spatial distribution of gold balls was used by Petersen et al (2003) in their analysis of gold labeled PSDs.

Another hurdle to overcome is to determine if the distribution of gold attached to PSDs is random or not. In theory this is simple. If you have random sets of points, you can compare them to the distribution of gold balls to make this assessment. There are a variety of methods for analyzing the spatial distribution of points and for making this comparison (these methods will be discussed below), but first the random data must be generated. To do this, the boundary generated by the convex hull was used and a Monte Carlo simulation was used to randomly place points with the same density as the experimental distribution within the convex hull (Fig. 2.18). If the experimental distribution was compared to a single random distribution within the

same boundary it would likely appear non-random, even if it were random. Because of this, for each convex hull generated by each PSD, 100 trials of random distributions are generated and the data from all 100 random distributions are combined.

### **Pseudo three-dimensional simulation of random distributions**

In the case of the PSD, the actual distribution of the gold label is not only in two dimensions, as depicted in Fig. 2.17 and 2.18. It is true that the images collected by the microscope only provide information in two dimensions, but during the labeling process gold particles can reside anywhere in the X, Y and Z dimension of the PSD. Because of this discrepancy between the initial placement of gold particles during the labeling process versus the simulation of random points within the two-dimensional boundaries of the convex hull, we chose to use a pseudo-3D method for the simulation of randomly distributed gold.

To understand why the pseudo-3D simulation of gold particles was chosen it is helpful to know a little about image formation in the electron microscope. During transmission electron microscopy (TEM) electrons are transmitted through the sample and collected on the other side. Contrast in the image is generated by the differential scattering of electrons as they pass through portions of the sample that are of varying density. Because the electron beam passes directly through the sample, the image that is formed is really a two-dimensional projection of three-dimensional data. In other words, that data in the dimension parallel to the electron beam is collapsed. This means that two gold balls could appear to overlap if they are at different levels in the Z-dimension of the PSD. To account for any subtleties in the two-dimensional distribution generated by a projection through a three-dimensional distribution of gold, the initial random arrangement of simulated gold particles was done in three-dimensions. And then XY coordinates from a simulated two-dimensional projection were used. The three-dimensional volume used as a boundary for the simulated random particles was generated by extending the convex hull calculated for each dataset 60 nm along the Z-axis (which is the

average thickness of a PSD). The basic steps of the pseudo-3D simulation are illustrated in Fig. A.1.

While randomly distributing the simulated particles within the three-dimensional boundaries is relatively straightforward, there are a few constraints that must be taken into account. These are related to physical constraints placed on the actual labeling due to the size of the gold balls. In our immuno-gold labeling experiments we used a secondary antibody conjugated to a 12 nm gold particle. This means that the placement of the simulated particles had to obey the same principles of volume exclusion placed on the actual gold particles during labeling. Obviously the volume exclusion depends on the size of the gold particle and should be adjusted if a different sized gold particle is used. Fundamentally, if the XYZ coordinate used to assign the position of the gold ball represents the center of the particle, then the simulated particles cannot be placed closer than two times the radius of the particle used (Fig. A.2A demonstrates this principle). This distance represents the minimal possible distance between the centers of two particles in three-dimensional space. In this case the two particles are physically touching one another.

On top of the constraint placed by volume exclusion there was an additional restriction on placement of simulated particles related to overlap in three-dimensions. If two particles are far enough apart in the Z-axis (greater than twice the radius) it is possible for them to overlap in the X or Y axis (Fig. A.2B-D). If they share the same XY coordinates then it will appear there is only one gold ball (Fig. A.2B) in the two-dimensional projection. Because of this a maximum amount of overlap in the X and Y dimension must be established, and we chose the radius of the gold ball (6 nm in our case, as shown in Fig. A.2D). Any overlap more than the radius of the gold balls and it becomes difficult to distinguish between one and two gold balls (Fig. A.2C). This is evident in the experimental data as well. Fig. A.2E depicts two gold balls



that are completely separated in the X and Y axes. The filled dark circles below each panel in Fig.

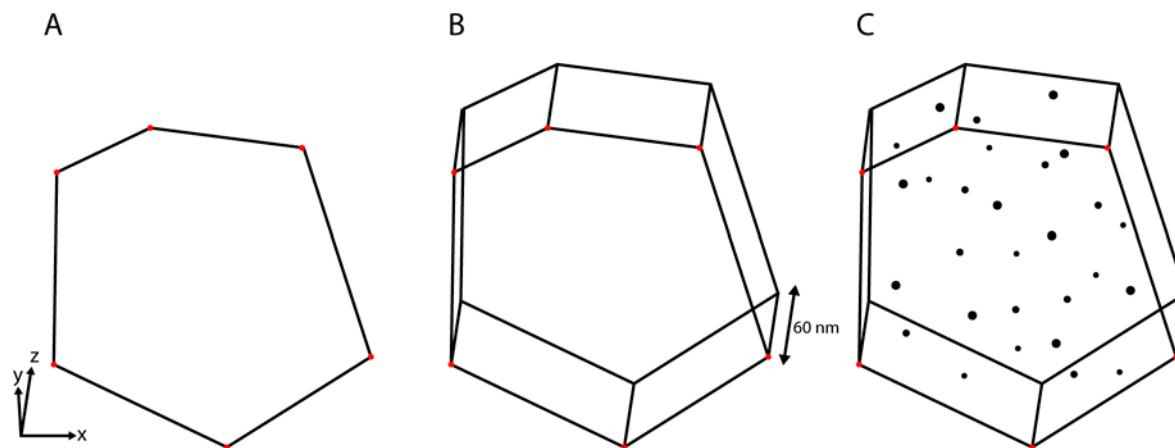


**Fig. A.1** *Illustration of the pseudo-3D simulation of randomly distributed gold particles.*

(A) Two-dimensional convex hull like those generated for datasets generated by immuno-gold labeling of isolated PSDs. (B) Three-dimensional version of the convex-hull in A with 60 nm of thickness added along the Z-axis. (C) Simulated gold particles randomly distributed through the volume in B illustrating the initial three-dimensional stage of the simulation process. The XY coordinates of the particles are then used as if they were from a two-dimensional projection of the data, similar to that generated by the electron microscope.

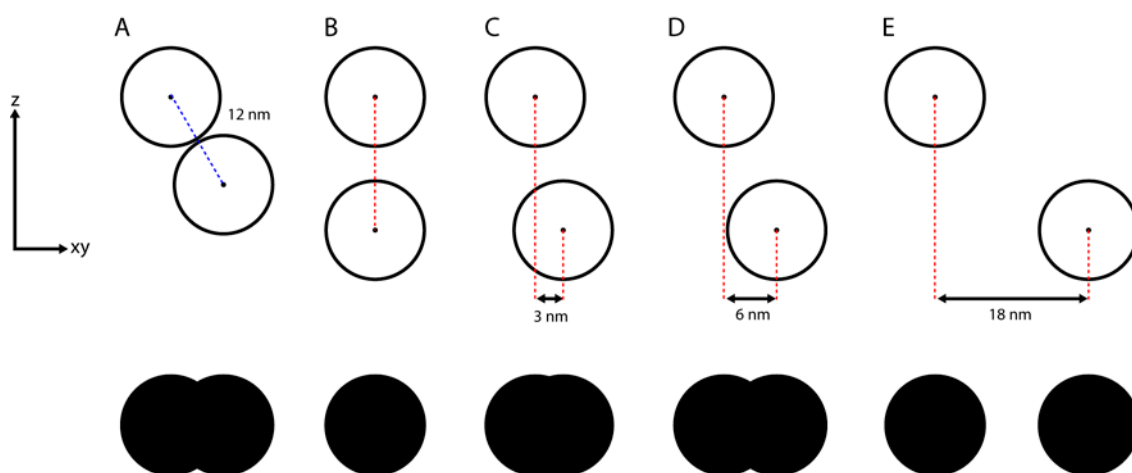


**Fig. A.2** *Principles of particle placement in the pseudo-3D simulations.*

(A) Depiction of the minimum distance in three-dimensions that can exist between the centers of two gold particles (12 nm). This distance is determined by the size of the gold particle due to volume exclusion. (B-D) Depiction of gold balls separated in along the Z-axis, but overlapping in the XY axis. The maximum amount of overlap during the random placement of particles in three-dimensions is shown in D. (E) Gold balls fully separated in all dimensions. Filled circles below each panel illustrate what the projection of the gold balls above would look like with the electron beam traveling down through the Z-axis.

A.2 illustrate what the projection of the gold balls depicted above them would look like with the electron beam traveling down through the Z-axis.

With these initial issues worked out and simulated random distributions for comparison to each PSD's gold dataset, it was possible to analyze and compare the experimental and random distributions. To study the distribution of gold balls linked to specific proteins within the PSD a variety of methods were explored, and the advantages of each method and the results are described below.

### **Nearest Neighbor Analysis**

The first method to be explored is known as nearest neighbor analysis. It was originally chosen, because it was previously used to analyze the distribution of gold labeled proteins within isolated PSDs. Because of this it seemed like a reasonable place to start.

Nearest neighbor analysis is conceptually straightforward. In fact, the name itself basically describes the approach. For each gold ball in the distribution, the distance between it and its nearest neighbor is measured. This means that there will be only one measured distance associated with each particle in the dataset. Once all of these measurements are in hand there are a few different ways to compare the data. One way is to bin the data and generate a histogram of nearest neighbor distances. In this way the histogram of the experimental distribution can be compared to the histogram generated by the nearest neighbor distances of the simulated randomly distributed particles. These two histograms can then be tested for statistically significant differences. While a variety of tests exist we chose to use a comparison via a minimum and maximum envelope function as well as the Kolmogorov-Smirnov test (a non-parametric test). To do this the minimum and maximum values from all of the random distributions are plotted along with the mean values, and function as the upper and lower boundaries that were achieved by the random data. If the plot of the experimental data falls outside of either envelope it is considered to be non-random.

Another metric for comparing the data is to determine the peak nearest neighbor distance of the plotted histogram, which is what Petersen et al (2003) did to examine PSD-95 and CaMKII. The peak distance represents the nearest neighbor distance that is most common in the data, and therefore the distance most likely to find another copy of the labeled protein. This distance could correspond to the distance between two identical epitopes in a protein that dimerizes such as PSD-95, or it could relate to the distance between subunits in a multimeric complex such as CaMKII (this would obviously require a label that is small enough to have multiple find to a single CaMKII holoenzyme). Another possible determinant of the peak nearest neighbor distance could be the length of a linker molecule tethering two labeled molecules together. It is important to keep in mind that the peak nearest neighbor distance does not have to be the same as the mean nearest neighbor distance. In fact, in the case of PSDs it was never the case that the nearest neighbor distances were normally distributed about the peak value. In general, nearest neighbor histograms showed a long tale, which meant that the mean nearest neighbor distance was larger than the peak distance.

While nearest neighbor analysis is useful for generating statistics about the distance between each particle and the next closest one, which can be useful in trying to understand pair-wise packing of molecules, it lacks the ability to analyze the global distribution of labeled proteins. This is inherent in the methods use of only the distance between each particle and the next nearest one. The principle of this limitation is illustrated in Fig. A.3, where three simple distributions are shown. If all three distributions are analyzed the same result would be generated despite their obvious differences. In all three distributions the nearest neighbor distances are the same for all pairs of particles (represented by the red brackets). However, the particles of the distribution in the left panel show a different orientation than the particles in the center panel, and while the particles in the right panel share the same orientation the pairs are more closely packed.

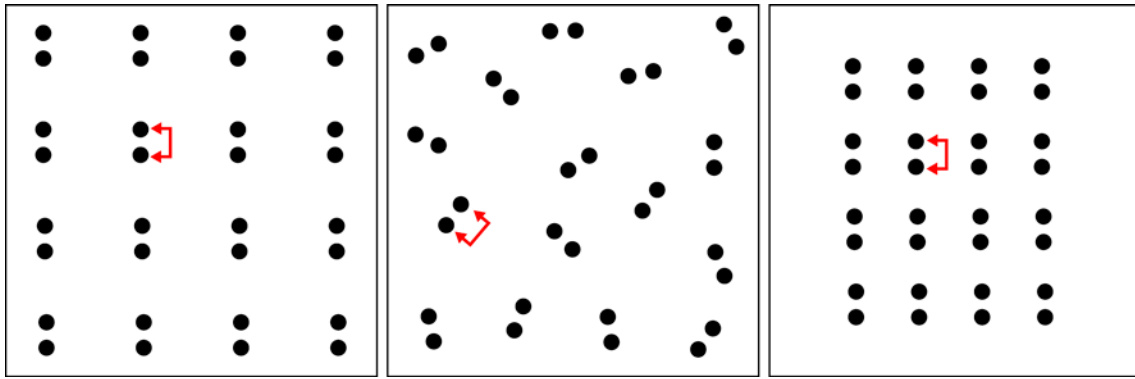


**Fig. A.3** *Nearest Neighbor Analysis can be Blind to the Global Distribution of Particles.*

Three distributions of the same number of particles that appear identical to nearest neighbor analysis. Because all three distributions share the same pair-wise nearest neighbor distance (red brackets) they cannot be distinguished by analysis. The middle panel shows pairs in different orientations with respect to the first panel, and the last panel shows pairs that are in the same orientation but with a closer packing distance.

Results from nearest neighbor analysis of PSDs is summarized in Table A.1 - A.3. As you can see nearly every distribution was shown to be non-random according to the nearest neighbor analysis.

### **Pair Correlation Function Analysis**

One way to incorporate more than just the nearest neighbor distance is to use pair correlation function (PCF) analysis. Instead of measuring only the distance between a particle and its nearest neighbor, pair correlation analysis measures the distance between every possible pair of particles in the entire dataset. The principle of PCF analysis is illustrated in Fig. A.4, and by extending the analysis beyond only the nearest neighbor distance, to that of all pair distances, the analysis is capable of detecting clustering in the particle sets.

The analysis starts by measuring the distance between the first gold ball and that of every other particle in the dataset (as illustrated in panel 2 of Fig. A.4). Next, you move to the following particle and measure the distance between it and all other particles except the first particle (panel 3 of Fig. A.4). This procedure is continued until the distance between all particles is measured. The principle lies in the fact that if the particles are clustered, there will be an abundance of shorter measured distances within the distribution and when a histogram is plotted it will be evident in the peak. Of course, this clustering is only detectable if there is data from a random distribution with which to compare it. Pair correlation histograms from simulated data can be seen in Fig. A.5, which demonstrates the tests ability to detect simulated clustering. For this test, simulated clustering of 121 gold particles was generated in a square of 480 nm per side. The diameter of gold particles is 12 nm. First, 11 particles were randomly distributed within the square. For the following 110, if the assigned location of a gold particle was not within 18 nm from any of the previously located particles, this new location was rejected and the process was repeated until all 110 gold particles were placed in the square. One can see the resulting clustering of black circles as a result of this methodology.

	<b>E19</b>	<b>P2</b>	<b>P20</b>	<b>P60</b>
$\alpha$ -Actinin	7 of 7	15 of 15	10 of 10	15 of 16
$\alpha$ CaMKII	4 of 4	12 of 12	16 of 16	13 of 17
$\beta$ CaMKII	1 of 1	9 of 11	15 of 15	14 of 15
CaM	10 of 10	14 of 14	N/A	6 of 6
GluR1	N/A	3 of 3	N/A	7 of 7
NR1	4 of 4	15 of 15	8 of 8	16 of 16
NR2b	6 of 6	16 of 16	11 of 11	11 of 11
PSD95	N/A	6 of 6	13 of 13	15 of 20

**Table A.1** *Nearest Neighbor test for non-randomness using the Kolmogorov-Smirnov test for significance ( $P < 0.05$ ).*

Mean (nm)				
	E19	P2	P20	P60
<b><math>\alpha</math>-Actinin</b>	42.6	29.8	43.2	25.9
<b><math>\alpha</math>CaMKII</b>	67.5	49.3	33	25.7
<b><math>\beta</math>CaMKII</b>	36.2	40	29	27.1
<b>CaM</b>	32	44.8	N/A	53.4
<b>GluR1</b>	N/A	95.1	N/A	76.7
<b>NR1</b>	47.8	55.6	39.4	44.3
<b>NR2b</b>	43	43.9	39.6	33.1
<b>PSD95</b>	N/A	59	27.7	27.5

**Table A.2** *Mean Nearest Neighbor distances (nm).*



Peak (nm)				
	E19	P2	P20	P60
<b><math>\alpha</math>-Actinin</b>	17	12	13	12
<b><math>\alpha</math>CaMKII</b>	45	10	22	19
<b><math>\beta</math>CaMKII</b>	15	22	21	28
<b>CaM</b>	15	18	N/A	36
<b>GluR1</b>	N/A	21	N/A	23
<b>NR1</b>	24	20	17	31
<b>NR2b</b>	16	12	34	19
<b>PSD95</b>	N/A	16	21	20

**Table A.3** *Peak Nearest Neighbor distances (nm).*

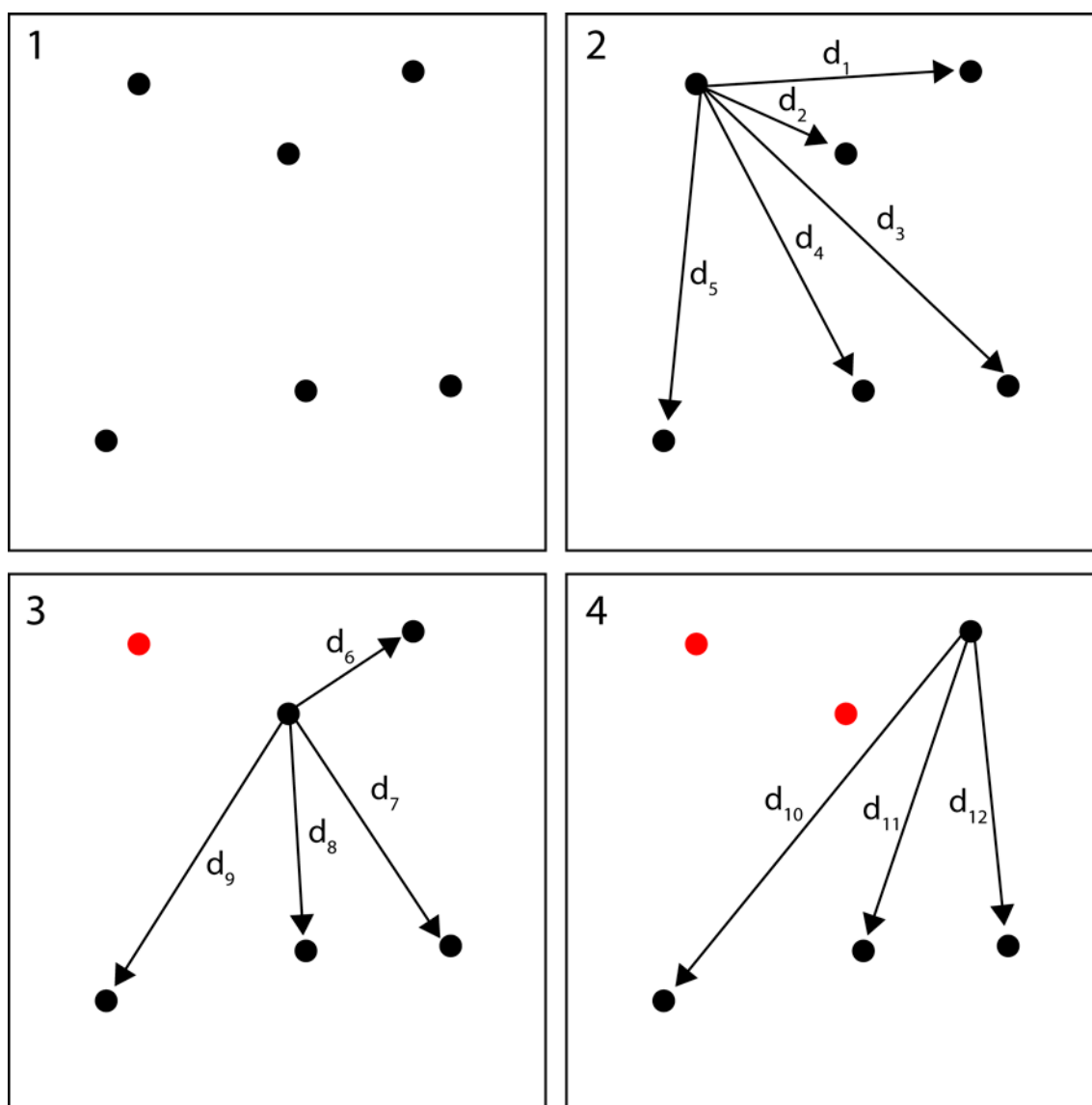


**Fig. A.4** *Principle of PCF Analysis*

Panel 1 shows a small distribution of points. First, the distance between the first point and every other point is measured (panel 2). Next, the distance between the next point and all other points, except for the first point (red point in panel 3), is measured. The process is continued as seen in panel 4 until the distance between every possible pair of points is measured.

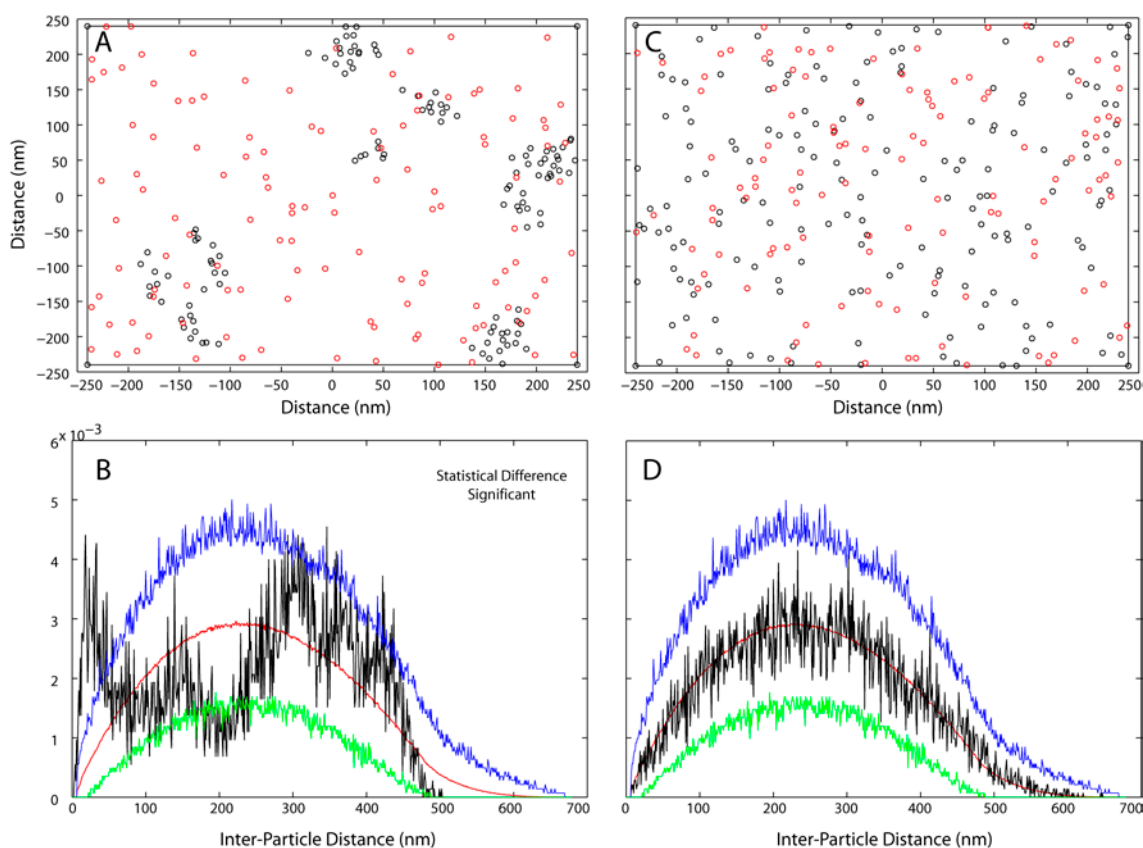


**Fig. A.5** Test for clustering by pair correlation function.

(A) Simulated clustering of 121 gold particles (black circles) in a square of 480 nm per side. 121 randomly places particles (red circles) are also displayed. (B) Plot of the inter-particle distance distribution (black line) of the clustered particle set. The red plot is of the random particle distribution and the blue and green lines represent the maximum and minimum envelopes of the random data, respectively. (C) In this plot both the black and red circles are randomly distributed. (D) Plot of the inter-particle distance distribution as in B. The histograms of randomly distributed red circles (the red line) is generated from 1000 iterations of simulated placement. This is why the line appears so smooth compared to the black line which only represents 121 black particles.

For comparison, a set of randomly distributed particles of the same number is shown (red circles). In panel B, the inter-particle distance distribution (black line) of the clustered particle set (black circles in panel A) was plotted against the inter-particle distance (X-axis, at 1 nm increment). The mean, upper, and lower envelope of the inter-particle distance distribution for 1000 sets of simulated gold particles are also shown (red, blue, and green, respectively). Clearly, the data (black line) does not lie between the upper (blue) and lower (green) envelope of the simulated random point pattern, indicating the rejection of the null hypothesis (of complete spatial randomness). As a control (panel C), we used one of the randomly distributed particle patterns (black circles in C) to test this method. As in panel A, the point distribution pattern is compared to that of the average of 1000 patterns of complete spatial randomness (red circles). We then calculated the inter-particle distance distribution (black line) for this randomly distributed point pattern (black circles in C) and plotted them against histogram generated by the randomly distributed particles (red circles in C). In this case, the distribution function does lie between the upper and lower envelope of the simulated random point pattern. Table A.4 summarized how many PSDs showed non-randomness using PCF analysis according to the Kolmogorov-Smirnov test at a P value of less than 0.05.

### **Ripley's K Function Analysis**

A third method for analyzing the distribution of the particles is known as Ripley's K-function (RKF) analysis. It is a well-established method for analyzing point-pattern distributions such as the gold labels attached to PSDs. Like pair correlation analysis it is well-suited for finding clustering. Ripley's K-function is mathematically related to the pair correlation function, but the method of analysis is different. Instead of measuring the distance between pairs of particles you start by choosing a particle and counting the number of surrounding particles that fall within a given radius of it. You then incrementally increase the size of the radius and calculate the number of particles that fall within each concentric radius.

	<b>E19</b>	<b>P2</b>	<b>P20</b>	<b>P60</b>
<b><math>\alpha</math>-Actinin</b>	7 of 7	15 of 15	10 of 10	16 of 16
<b><math>\alpha</math>CaMKII</b>	4 of 4	12 of 12	16 of 16	17 of 17
<b><math>\beta</math>CaMKII</b>	1 of 1	11 of 11	15 of 15	15 of 15
<b>CaM</b>	10 of 10	14 of 14	N/A	6 of 6
<b>GluR1</b>	N/A	3 of 3	N/A	7 of 7
<b>NR1</b>	4 of 4	15 of 15	8 of 8	16 of 16
<b>NR2b</b>	6 of 6	16 of 16	11 of 11	11 of 11
<b>PSD95</b>	N/A	6 of 6	13 of 13	20 of 20

**Table A.4** *PCF test for non-randomness using the Kolmogorov-Smirnov test for significance ( $P < 0.05$ ).*

You then repeat the process for each particle in the dataset and combine the data to generate a plot of the average particle density versus the radius. Because the PSD is an area with finite boundaries, the maximum radius size used for each individual PSD was defined by the maximum distance across the convex hull surrounding the dataset. As illustrated in Fig. A.6, if the particles are clustered then more surrounding particles will fall within the smaller radii, thus causing the plot of the density to rise faster than that of the randomly distributed data. Just as with nearest neighbor and pair correlation analysis we used a minimum and maximum envelope as a measure of statistical difference between the experimental and simulated random data.

Among the eight different molecules probed in this study, at all four developmental time points, RKF analysis showed significant clustering in the majority of PSDs analyzed. Table A.5 summarizes the number of PSDs analyzed in each group and those that showed a significant deviation from random according to the min/max envelope test. If a PSD did not have a minimum of 10 gold balls that fell within the convex hull we chose to remove it from the analysis, because the small number of data points led to RKF plots with large fluctuations. Because of this criterion, some PSDs at E19 and P2 could not be analyzed since labeling densities were generally lower early in development. CaM is an exception to this as labeling was high at E19 and was minimal by P60. It is important to point out that the number of simulations used to generate the random data was set to 100 in this analysis. When the stringency was raised by using 1000 trials the min/max envelopes increased and fewer PSDs were considered significantly different from random. At this point it is not clear how one should select the stringency of the test, but it is clear that it does have an effect on the results of the analysis. Because of the large number of PSDs analyzed and the fact that the most of them showed clustering by RKF analysis it, Fig. 2.19 shows only one RKF plot of the PSD in Fig. 2.17. Clustering is obvious because at the smaller radii the experimental plot falls well outside the

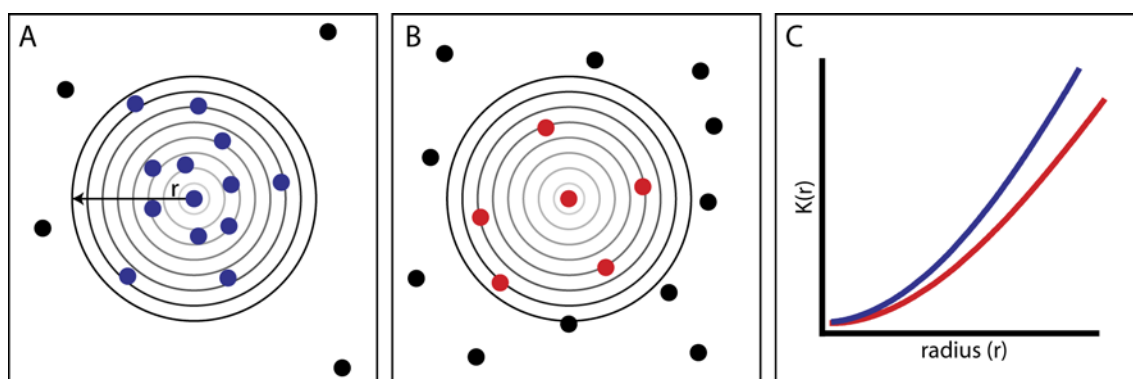


**Figure A.6** *Illustration of the principles of RKF analysis.*

RKF analysis is carried out by calculating the average number of gold markers that fall within increasing radii ( $r$ ) extending from the center of each gold marker in the set. If clustering exists within the data set more gold particles will fall within a smaller radius when compared to the simulated random distributions. In this illustration (A) represents a group of gold particles that are clustered and (B) represents the same number of gold particles randomly distributed. Gold balls that fall within the illustrated radii are blue in the clustered distribution and red in the random distribution. While the concentric radii extending from the central gold particle are the only ones illustrated, in reality, the calculation is performed for each point within the distribution and then compiled. Panel (C) illustrates how the clustered particles (blue) will generate an RKF plot that rises faster than the RKF plot for the randomly distributed particles (red), because more gold particles fall within the smaller radii.

	<b>E19</b>	<b>P2</b>	<b>P20</b>	<b>P60</b>
<b><math>\alpha</math>-Actinin</b>	6 of 7	12 of 15	8 of 10	15 of 16
<b><math>\alpha</math>CaMKII</b>	1 of 4	10 of 12	14 of 16	14 of 17
<b><math>\beta</math>CaMKII</b>	1 of 1	10 of 11	14 of 15	12 of 15
<b>CaM</b>	8 of 10	10 of 14	NA	5 of 6
<b>GluR1</b>	NA	2 of 3	NA	4 of 7
<b>NR1</b>	2 of 4	9 of 15	5 of 8	13 of 16
<b>NR2b</b>	3 of 6	11 of 16	2 of 11	14 of 16
<b>PSD95</b>	NA	6 of 6	12 of 13	15 of 16

**Table A.5** *Number of individual PSDs that showed clustering by RKF analysis.*



maximum envelope (this portion of the plot is blown up in the inset). While most plots showing non-randomness fell outside the maximum envelope, a few PSDs showed a plot that dropped below the minimum envelope. What this means in terms of the distribution is not entirely clear at this point. A more systematic analysis of the behavior of RKF plots under various simulated distribution conditions is needed to try and make complete sense of how these differences in the plots relates to the underlying distribution of the particles.

## References

- Ahmari SE, Buchanan J, Smith SJ. 2000. Assembly of presynaptic active zones from cytoplasmic transport packets. *Nat Neurosci* 3(5):445-451.
- Barria A, Malinow R. 2005. NMDA receptor subunit composition controls synaptic plasticity by regulating binding to CaMKII. *Neuron* 48(2):289-301.
- Benke TA, Luthi A, Isaac JT, Collingridge GL. 1998. Modulation of AMPA receptor unitary conductance by synaptic activity. *Nature* 393(6687):793-797.
- Bennett MK, Erondur NE, Kennedy MB. 1983. Purification and characterization of a calmodulin-dependent protein kinase that is highly concentrated in brain. *J Biol Chem* 258(20):12735-12744.
- Bhatt DH, Zhang S, Gan WB. 2009. Dendritic spine dynamics. *Annu Rev Physiol* 71:261-282.
- Blanchard A, Ohanian V, Critchley D. 1989. The structure and function of alpha-actinin. *J Muscle Res Cell Motil* 10(4):280-289.
- Blomberg F, Cohen RS, Siekevitz P. 1977. The structure of postsynaptic densities isolated from dog cerebral cortex. II. Characterization and arrangement of some of the major proteins within the structure. *J Cell Biol* 74(1):204-225.

Bredt DS, Nicoll RA. 2003. AMPA receptor trafficking at excitatory synapses. *Neuron* 40(2):361-379.

Bresler T, Ramati Y, Zamorano PL, Zhai R, Garner CC, Ziv NE. 2001. The dynamics of SAP90/PSD-95 recruitment to new synaptic junctions. *Mol Cell Neurosci* 18(2):149-167.

Bresler T, Shapira M, Boeckers T, Dresbach T, Futter M, Garner CC, Rosenblum K, Gundelfinger ED, Ziv NE. 2004. Postsynaptic density assembly is fundamentally different from presynaptic active zone assembly. *J Neurosci* 24(6):1507-1520.

Cajal R. 1899. *La Textura del Sistema Nervioso del Hombre y de los Vertebrados*. Madrid: Moya.

Carlin RK, Grab DJ, Siekevitz P. 1981. Function of a calmodulin in postsynaptic densities. III. Calmodulin-binding proteins of the postsynaptic density. *J Cell Biol* 89(3):449-455.

Chen X, Vinade L, Leapman RD, Petersen JD, Nakagawa T, Phillips TM, Sheng M, Reese TS. 2005. Mass of the postsynaptic density and enumeration of three key molecules. *Proc Natl Acad Sci U S A* 102(32):11551-11556.

Chen X, Winters C, Azzam R, Li X, Galbraith JA, Leapman RD, Reese TS. 2008. Organization of the core structure of the postsynaptic density. *Proc Natl Acad Sci U S A* 105(11):4453-4458.

Cheng D, Hoogenraad CC, Rush J, Ramm E, Schlager MA, Duong DM, Xu P, Wijayawardana SR, Hanfelt J, Nakagawa T, Sheng M, Peng J. 2006. Relative and absolute quantification of

postsynaptic density proteome isolated from rat forebrain and cerebellum. *Mol Cell Proteomics* 5(6):1158-1170.

Cohen RS, Blomberg F, Berzins K, Siekevitz P. 1977. The structure of postsynaptic densities isolated from dog cerebral cortex. I. Overall morphology and protein composition. *J Cell Biol* 74(1):181-203.

Cohen RS, Siekevitz P. 1978. Form of the postsynaptic density. A serial section study. *J Cell Biol* 78(1):36-46.

Collingridge GL. 2003. The induction of N-methyl-D-aspartate receptor-dependent long-term potentiation. *Philos Trans R Soc Lond B Biol Sci* 358(1432):635-641.

Cotman CW, Banker G, Churchill L, Taylor D. 1974. Isolation of postsynaptic densities from rat brain. *J Cell Biol* 63(2 Pt 1):441-455.

Cull-Candy S, Brickley S, Farrant M. 2001. NMDA receptor subunits: diversity, development and disease. *Curr Opin Neurobiol* 11(3):327-335.

DeGiorgis JA, Galbraith JA, Dosemeci A, Chen X, Reese TS. 2006. Distribution of the scaffolding proteins PSD-95, PSD-93, and SAP97 in isolated PSDs. *Brain Cell Biol* 35(4-6):239-250.

Derkach V, Barria A, Soderling TR. 1999.  $\text{Ca}^{2+}$ /calmodulin-kinase II enhances channel conductance of  $\alpha$ -amino-3-hydroxy-5-methyl-4-isoxazolepropionate type glutamate receptors. *Proc Natl Acad Sci U S A* 96(6):3269-3274.

Dosemeci A, Makusky AJ, Jankowska-Stephens E, Yang X, Slotta DJ, Markey SP. 2007. Composition of the synaptic PSD-95 complex. *Mol Cell Proteomics* 6(10):1749-1760.

Dosemeci A, Reese TS, Petersen J, Tao-Cheng JH. 2000. A novel particulate form of  $\text{Ca}^{2+}$ /calmodulin-dependent [correction of  $\text{Ca}^{2+}$ /CaMKII-dependent] protein kinase II in neurons. *J Neurosci* 20(9):3076-3084.

Dosemeci A, Tao-Cheng JH, Vinade L, Jaffe H. 2006. Preparation of postsynaptic density fraction from hippocampal slices and proteomic analysis. *Biochem Biophys Res Commun* 339(2):687-694.

Dosemeci A, Tao-Cheng JH, Vinade L, Winters CA, Pozzo-Miller L, Reese TS. 2001. Glutamate-induced transient modification of the postsynaptic density. *Proc Natl Acad Sci U S A* 98(18):10428-10432.

Dubochet J, Adrian M, Chang JJ, Homo JC, Lepault J, McDowell AW, Schultz P. 1988. Cryo-electron microscopy of vitrified specimens. *Q Rev Biophys* 21(2):129-228.

Dunaevsky A, Tashiro A, Majewska A, Mason C, Yuste R. 1999. Developmental regulation of spine motility in the mammalian central nervous system. *Proc Natl Acad Sci U S A* 96(23):13438-13443.

Ehlers MD. 2000. Reinsertion or degradation of AMPA receptors determined by activity-dependent endocytic sorting. *Neuron* 28(2):511-525.

Ehlers MD. 2003. Activity level controls postsynaptic composition and signaling via the ubiquitin-proteasome system. *Nat Neurosci* 6(3):231-242.

Engert F, Bonhoeffer T. 1999. Dendritic spine changes associated with hippocampal long-term synaptic plasticity. *Nature* 399(6731):66-70.

Fernandez-Busnadiego R, Zuber B, Maurer UE, Cyrklaff M, Baumeister W, Lucic V. 2010. Quantitative analysis of the native presynaptic cytomatrix by cryoelectron tomography. *J Cell Biol* 188(1):145-156.

Fink CC, Bayer KU, Myers JW, Ferrell JE, Jr., Schulman H, Meyer T. 2003. Selective regulation of neurite extension and synapse formation by the beta but not the alpha isoform of CaMKII. *Neuron* 39(2):283-297.

Fisher SA, Fischer TM, Carew TJ. 1997. Multiple overlapping processes underlying short-term synaptic enhancement. *Trends Neurosci* 20(4):170-177.

Foster M. 1897. *A Textbook of Physiology*. London: MacMillan.

Frankland PW, O'Brien C, Ohno M, Kirkwood A, Silva AJ. 2001. Alpha-CaMKII-dependent plasticity in the cortex is required for permanent memory. *Nature* 411(6835):309-313.

Friedman HV, Bresler T, Garner CC, Ziv NE. 2000. Assembly of new individual excitatory synapses: time course and temporal order of synaptic molecule recruitment. *Neuron* 27(1):57-69.

Gaertner TR, Kolodziej SJ, Wang D, Kobayashi R, Koomen JM, Stoops JK, Waxham MN. 2004. Comparative analyses of the three-dimensional structures and enzymatic properties of alpha, beta, gamma and delta isoforms of Ca<sup>2+</sup>-calmodulin-dependent protein kinase II. *J Biol Chem* 279(13):12484-12494.

Gardoni F, Caputi A, Cimino M, Pastorino L, Cattabeni F, Di Luca M. 1998. Calcium/calmodulin-dependent protein kinase II is associated with NR2A/B subunits of NMDA receptor in postsynaptic densities. *J Neurochem* 71(4):1733-1741.

Giese KP, Fedorov NB, Filipkowski RK, Silva AJ. 1998. Autophosphorylation at Thr286 of the alpha calcium-calmodulin kinase II in LTP and learning. *Science* 279(5352):870-873.

Glazewski S, Chen CM, Silva A, Fox K. 1996. Requirement for alpha-CaMKII in experience-dependent plasticity of the barrel cortex. *Science* 272(5260):421-423.

Glazewski S, Giese KP, Silva A, Fox K. 2000. The role of alpha-CaMKII autophosphorylation in neocortical experience-dependent plasticity. *Nat Neurosci* 3(9):911-918.

Gray EG. 1959a. Axo-somatic and axo-dendritic synapses of the cerebral cortex: an electron microscope study. *J Anat* 93:420-433.

Gray EG. 1959b. Electron microscopy of synaptic contacts on dendrite spines of the cerebral cortex. *Nature* 183(4675):1592-1593.

Grutzendler J, Kasthuri N, Gan WB. 2002. Long-term dendritic spine stability in the adult cortex. *Nature* 420(6917):812-816.

Gulley RL, Reese TS. 1981. Cytoskeletal organization at the postsynaptic complex. *J Cell Biol* 91(1):298-302.

Harris KM, Jensen FE, Tsao B. 1992. Three-dimensional structure of dendritic spines and synapses in rat hippocampus (CA1) at postnatal day 15 and adult ages: implications for the maturation of synaptic physiology and long-term potentiation. *J Neurosci* 12(7):2685-2705.

Hudmon A, Lebel E, Roy H, Sik A, Schulman H, Waxham MN, De Koninck P. 2005. A mechanism for  $\text{Ca}^{2+}$ /calmodulin-dependent protein kinase II clustering at synaptic and nonsynaptic sites based on self-association. *J Neurosci* 25(30):6971-6983.

Huttenlocher PR. 1979. Synaptic density in human frontal cortex - developmental changes and effects of aging. *Brain Res* 163(2):195-205.

Illian J, Penittinen A, Stoyan H, Stoyan D. 2008. Statistical Analysis and Modeling of Spatial Point Patterns. John Wiley & Sons L, editor. Chichester, West Sussex, England: The Atrium.



Itarat W, Jones DG. 1992. Perforated synapses are present during synaptogenesis in rat neocortex. *Synapse* 11(4):279-286.

Ito I, Hidaka H, Sugiyama H. 1991. Effects of KN-62, a specific inhibitor of calcium/calmodulin-dependent protein kinase II, on long-term potentiation in the rat hippocampus. *Neurosci Lett* 121(1-2):119-121.

Jordan BA, Fernholz BD, Boussac M, Xu C, Grigorean G, Ziff EB, Neubert TA. 2004. Identification and verification of novel rodent postsynaptic density proteins. *Mol Cell Proteomics* 3(9):857-871.

Kelly PT, Yip RK, Shields SM, Hay M. 1985. Calmodulin-dependent protein phosphorylation in synaptic junctions. *J Neurochem* 45(5):1620-1634.

Kennedy MB, Bennett MK, Erondy NE. 1983. Biochemical and immunochemical evidence that the "major postsynaptic density protein" is a subunit of a calmodulin-dependent protein kinase. *Proc Natl Acad Sci U S A* 80(23):7357-7361.

Kimura R, Silva AJ, Ohno M. 2008. Autophosphorylation of alphaCaMKII is differentially involved in new learning and unlearning mechanisms of memory extinction. *Learn Mem* 15(11):837-843.

Kolb SJ, Hudmon A, Ginsberg TR, Waxham MN. 1998. Identification of domains essential for the assembly of calcium/calmodulin-dependent protein kinase II holoenzymes. *J Biol Chem* 273(47):31555-31564.

Kolodziej SJ, Hudmon A, Waxham MN, Stoops JK. 2000. Three-dimensional reconstructions of calcium/calmodulin-dependent (CaM) kinase II $\alpha$  and truncated CaM kinase II $\alpha$  reveal a unique organization for its structural core and functional domains. *J Biol Chem* 275(19):14354-14359.

Kornau HC, Schenker LT, Kennedy MB, Seeburg PH. 1995. Domain interaction between NMDA receptor subunits and the postsynaptic density protein PSD-95. *Science* 269(5231):1737-1740.

Korobova F, Svitkina T. Molecular architecture of synaptic actin cytoskeleton in hippocampal neurons reveals a mechanism of dendritic spine morphogenesis. *Mol Biol Cell* 21(1):165-176.

Lamprecht R, LeDoux J. 2004. Structural plasticity and memory. *Nat Rev Neurosci* 5(1):45-54.

Landis DM, Weinstein LA, Reese TS. 1987. Substructure in the postsynaptic density of Purkinje cell dendritic spines revealed by rapid freezing and etching. *Synapse* 1(6):552-558.

Lee SH, Simonetta A, Sheng M. 2004. Subunit rules governing the sorting of internalized AMPA receptors in hippocampal neurons. *Neuron* 43(2):221-236.

Leonard AS, Lim IA, Hemsworth DE, Horne MC, Hell JW. 1999. Calcium/calmodulin-dependent protein kinase II is associated with the N-methyl-D-aspartate receptor. *Proc Natl Acad Sci U S A* 96(6):3239-3244.

- Li KW, Hornshaw MP, Van Der Schors RC, Watson R, Tate S, Casetta B, Jimenez CR, Gouwenberg Y, Gundelfinger ED, Smalla KH, Smit AB. 2004. Proteomics analysis of rat brain postsynaptic density. Implications of the diverse protein functional groups for the integration of synaptic physiology. *J Biol Chem* 279(2):987-1002.
- Lin YC, Redmond L. 2008. CaMKII $\beta$  binding to stable F-actin in vivo regulates F-actin filament stability. *Proc Natl Acad Sci U S A* 105(41):15791-15796.
- Lippman J, Dunaevsky A. 2005. Dendritic spine morphogenesis and plasticity. *J Neurobiol* 64(1):47-57.
- Lisman JE, Zhabotinsky AM. 2001. A model of synaptic memory: a CaMKII/PP1 switch that potentiates transmission by organizing an AMPA receptor anchoring assembly. *Neuron* 31(2):191-201.
- Lou LL, Schulman H. 1989. Distinct autophosphorylation sites sequentially produce autonomy and inhibition of the multifunctional Ca<sup>2+</sup>/calmodulin-dependent protein kinase. *J Neurosci* 9(6):2020-2032.
- Lu W, Shi Y, Jackson AC, Bjorgan K, During MJ, Sprengel R, Seeburg PH, Nicoll RA. 2009. Subunit composition of synaptic AMPA receptors revealed by a single-cell genetic approach. *Neuron* 62(2):254-268.

Lucic V, Kossel AH, Yang T, Bonhoeffer T, Baumeister W, Sartori A. 2007. Multiscale imaging of neurons grown in culture: from light microscopy to cryo-electron tomography. *J Struct Biol* 160(2):146-156.

Lucic V, Yang T, Schweikert G, Forster F, Baumeister W. 2005. Morphological characterization of molecular complexes present in the synaptic cleft. *Structure* 13(3):423-434.

Majewska AK, Newton JR, Sur M. 2006. Remodeling of synaptic structure in sensory cortical areas in vivo. *J Neurosci* 26(11):3021-3029.

Malenka RC, Bear MF. 2004. LTP and LTD: an embarrassment of riches. *Neuron* 44(1):5-21.

Malenka RC, Lancaster B, Zucker RS. 1992. Temporal limits on the rise in postsynaptic calcium required for the induction of long-term potentiation. *Neuron* 9(1):121-128.

Maletic-Savatic M, Malinow R, Svoboda K. 1999. Rapid dendritic morphogenesis in CA1 hippocampal dendrites induced by synaptic activity. *Science* 283(5409):1923-1927.

Malinow R, Malenka RC. 2002. AMPA receptor trafficking and synaptic plasticity. *Annu Rev Neurosci* 25:103-126.

Markus EJ, Petit TL. 1987. Neocortical synaptogenesis, aging, and behavior: lifespan development in the motor-sensory system of the rat. *Exp Neurol* 96(2):262-278.

- Matus AI, Taff-Jones DH. 1978. Morphology and molecular composition of isolated postsynaptic junctional structures. *Proc R Soc Lond B Biol Sci* 203(1151):135-151.
- Maurer UE, Sodeik B, Grunewald K. 2008. Native 3D intermediates of membrane fusion in herpes simplex virus 1 entry. *Proc Natl Acad Sci U S A* 105(30):10559-10564.
- Merrill MA, Chen Y, Strack S, Hell JW. 2005. Activity-driven postsynaptic translocation of CaMKII. *Trends Pharmacol Sci* 26(12):645-653.
- Merrill MA, Malik Z, Akyol Z, Bartos JA, Leonard AS, Hudmon A, Shea MA, Hell JW. 2007. Displacement of alpha-actinin from the NMDA receptor NR1 C0 domain By Ca<sup>2+</sup>/calmodulin promotes CaMKII binding. *Biochemistry* 46(29):8485-8497.
- Migaud M, Charlesworth P, Dempster M, Webster LC, Watabe AM, Makhinson M, He Y, Ramsay MF, Morris RG, Morrison JH, O'Dell TJ, Grant SG. 1998. Enhanced long-term potentiation and impaired learning in mice with mutant postsynaptic density-95 protein. *Nature* 396(6710):433-439.
- Miller P, Zhabotinsky AM, Lisman JE, Wang XJ. 2005. The stability of a stochastic CaMKII switch: dependence on the number of enzyme molecules and protein turnover. *PLoS Biol* 3(4):e107.
- Miller SG, Kennedy MB. 1985. Distinct forebrain and cerebellar isozymes of type II Ca<sup>2+</sup>/calmodulin-dependent protein kinase associate differently with the postsynaptic density fraction. *J Biol Chem* 260(15):9039-9046.

Miller SG, Patton BL, Kennedy MB. 1988. Sequences of autophosphorylation sites in neuronal type II CaM kinase that control Ca<sup>2+</sup>(+)-independent activity. *Neuron* 1(7):593-604.

Ohta Y, Nishida E, Sakai H. 1986. Type II Ca<sup>2+</sup>/calmodulin-dependent protein kinase binds to actin filaments in a calmodulin-sensitive manner. *FEBS Lett* 208(2):423-426.

Okamoto K, Narayanan R, Lee SH, Murata K, Hayashi Y. 2007. The role of CaMKII as an F-actin-bundling protein crucial for maintenance of dendritic spine structure. *Proc Natl Acad Sci U S A* 104(15):6418-6423.

Palay SL. 1956. Synapses in the central nervous system. *J Biophys Biochem Cytol* 2(4, Suppl):193-202.

Palay SL. 1958. The morphology of synapses in the central nervous system. *Exp Cell Res* 14(Suppl 5):275-293.

Palay SL, Palade GE. 1955. The fine structure of neurons. *J Biophys Biochem Cytol* 1(1):69-88.

Passafaro M, Sala C, Niethammer M, Sheng M. 1999. Microtubule binding by CRIP1 and its potential role in the synaptic clustering of PSD-95. *Nat Neurosci* 2(12):1063-1069.

- Peng J, Kim MJ, Cheng D, Duong DM, Gygi SP, Sheng M. 2004. Semiquantitative proteomic analysis of rat forebrain postsynaptic density fractions by mass spectrometry. *J Biol Chem* 279(20):21003-21011.
- Petersen JD, Chen X, Vinade L, Dosemeci A, Lisman JE, Reese TS. 2003. Distribution of postsynaptic density (PSD)-95 and Ca<sup>2+</sup>/calmodulin-dependent protein kinase II at the PSD. *J Neurosci* 23(35):11270-11278.
- Petralia RS, Sans N, Wang YX, Wenthold RJ. 2005. Ontogeny of postsynaptic density proteins at glutamatergic synapses. *Mol Cell Neurosci* 29(3):436-452.
- Prange O, Murphy TH. 2001. Modular transport of postsynaptic density-95 clusters and association with stable spine precursors during early development of cortical neurons. *J Neurosci* 21(23):9325-9333.
- Rakic P, Bourgeois JP, Eckenhoff MF, Zecevic N, Goldman-Rakic PS. 1986. Concurrent overproduction of synapses in diverse regions of the primate cerebral cortex. *Science* 232(4747):232-235.
- Rao A, Kim E, Sheng M, Craig AM. 1998. Heterogeneity in the molecular composition of excitatory postsynaptic sites during development of hippocampal neurons in culture. *J Neurosci* 18(4):1217-1229.
- Ripley B. 1977. Modeling Spatial Patterns. *Journal of the Royal Statistical Society Series B (Methodological)* 39(2):40.

Robison AJ, Bartlett RK, Bass MA, Colbran RJ. 2005a. Differential modulation of  $\text{Ca}^{2+}$ /calmodulin-dependent protein kinase II activity by regulated interactions with N-methyl-D-aspartate receptor NR2B subunits and alpha-actinin. *J Biol Chem* 280(47):39316-39323.

Robison AJ, Bass MA, Jiao Y, MacMillan LB, Carmody LC, Bartlett RK, Colbran RJ. 2005b. Multivalent interactions of calcium/calmodulin-dependent protein kinase II with the postsynaptic density proteins NR2B, densin-180, and alpha-actinin-2. *J Biol Chem* 280(42):35329-35336.

Roche KW, O'Brien RJ, Mammen AL, Bernhardt J, Huganir RL. 1996. Characterization of multiple phosphorylation sites on the AMPA receptor GluR1 subunit. *Neuron* 16(6):1179-1188.

Rostaing P, Real E, Siksou L, Lechaire JP, Boudier T, Boeckers TM, Gertler F, Gundelfinger ED, Triller A, Marty S. 2006. Analysis of synaptic ultrastructure without fixative using high-pressure freezing and tomography. *Eur J Neurosci* 24(12):3463-3474.

Sanabria H, Swulius MT, Kolodziej SJ, Liu J, Waxham MN. 2009.  $\beta$ CaMKII regulates actin assembly and structure. *J Biol Chem* 284(15):9770-9780.

Schworer CM, Colbran RJ, Keefer JR, Soderling TR. 1988.  $\text{Ca}^{2+}$ /calmodulin-dependent protein kinase II. Identification of a regulatory autophosphorylation site adjacent to the inhibitory and calmodulin-binding domains. *J Biol Chem* 263(27):13486-13489.



Sekino Y, Kojima N, Shirao T. 2007. Role of actin cytoskeleton in dendritic spine morphogenesis. *Neurochem Int* 51(2-4):92-104.

Shapira M, Zhai RG, Dresbach T, Bresler T, Torres VI, Gundelfinger ED, Ziv NE, Garner CC. 2003. Unitary assembly of presynaptic active zones from Piccolo-Bassoon transport vesicles. *Neuron* 38(2):237-252.

Shen K, Meyer T. 1999. Dynamic control of CaMKII translocation and localization in hippocampal neurons by NMDA receptor stimulation. *Science* 284(5411):162-166.

Shen K, Teruel MN, Subramanian K, Meyer T. 1998. CaMKIIbeta functions as an F-actin targeting module that localizes CaMKIIalpha/beta heterooligomers to dendritic spines. *Neuron* 21(3):593-606.

Sheng M, Cummings J, Roldan LA, Jan YN, Jan LY. 1994. Changing subunit composition of heteromeric NMDA receptors during development of rat cortex. *Nature* 368(6467):144-147.

Silva AJ, Paylor R, Wehner JM, Tonegawa S. 1992a. Impaired spatial learning in alpha-calcium-calmodulin kinase II mutant mice. *Science* 257(5067):206-211.

Silva AJ, Stevens CF, Tonegawa S, Wang Y. 1992b. Deficient hippocampal long-term potentiation in alpha-calcium-calmodulin kinase II mutant mice. *Science* 257(5067):201-206.

Simons K, Toomre D. 2000. Lipid rafts and signal transduction. *Nat Rev Mol Cell Biol* 1(1):31-39.

Sorra KE, Harris KM. 1998. Stability in synapse number and size at 2 hr after long-term potentiation in hippocampal area CA1. *J Neurosci* 18(2):658-671.

Sosinsky GE, Nicholson BJ. 2005. Structural organization of gap junction channels. *Biochim Biophys Acta* 1711(2):99-125.

Strack S, McNeill RB, Colbran RJ. 2000. Mechanism and regulation of calcium/calmodulin-dependent protein kinase II targeting to the NR2B subunit of the N-methyl-D-aspartate receptor. *J Biol Chem* 275(31):23798-23806.

Suzuki T, Du F, Tian QB, Zhang J, Endo S. 2008. Ca<sup>2+</sup>/calmodulin-dependent protein kinase II $\alpha$  clusters are associated with stable lipid rafts and their formation traps PSD-95. *J Neurochem* 104(3):596-610.

Suzuki T, Ito J, Takagi H, Saitoh F, Nawa H, Shimizu H. 2001. Biochemical evidence for localization of AMPA-type glutamate receptor subunits in the dendritic raft. *Brain Res Mol Brain Res* 89(1-2):20-28.

Suzuki T, Okumura-Noji K, Tanaka R, Tada T. 1994. Rapid translocation of cytosolic Ca<sup>2+</sup>/calmodulin-dependent protein kinase II into postsynaptic density after decapitation. *J Neurochem* 63(4):1529-1537.

Taha S, Hanover JL, Silva AJ, Stryker MP. 2002. Autophosphorylation of  $\alpha$ CaMKII is required for ocular dominance plasticity. *Neuron* 36(3):483-491.

Tang J, Taylor DW, Taylor KA. 2001. The three-dimensional structure of alpha-actinin obtained by cryoelectron microscopy suggests a model for Ca(2+)-dependent actin binding. *J Mol Biol* 310(4):845-858.

Tao-Cheng JH, Vinade L, Pozzo-Miller LD, Reese TS, Dosemeci A. 2002. Calcium/calmodulin-dependent protein kinase II clusters in adult rat hippocampal slices. *Neuroscience* 115(2):435-440.

Tao-Cheng JH, Vinade L, Winters CA, Reese TS, Dosemeci A. 2005. Inhibition of phosphatase activity facilitates the formation and maintenance of NMDA-induced calcium/calmodulin-dependent protein kinase II clusters in hippocampal neurons. *Neuroscience* 130(3):651-656.

Tatavarty V, Kim EJ, Rodionov V, Yu J. 2009. Investigating sub-spine actin dynamics in rat hippocampal neurons with super-resolution optical imaging. *PLoS One* 4(11):e7724.

Vallano ML. 1989. Separation of isozymic forms of type II calcium/calmodulin-dependent protein kinase using cation-exchange chromatography. *J Neurosci Methods* 30(1):1-9.

Valtschanoff JG, Weinberg RJ. 2001. Laminar organization of the NMDA receptor complex within the postsynaptic density. *J Neurosci* 21(4):1211-1217.

Walikonis RS, Jensen ON, Mann M, Provance DW, Jr., Mercer JA, Kennedy MB. 2000. Identification of proteins in the postsynaptic density fraction by mass spectrometry. *J Neurosci* 20(11):4069-4080.

Walikonis RS, Oguni A, Khorosheva EM, Jeng CJ, Asuncion FJ, Kennedy MB. 2001. Densin-180 forms a ternary complex with the (alpha)-subunit of Ca<sup>2+</sup>/calmodulin-dependent protein kinase II and (alpha)-actinin. *J Neurosci* 21(2):423-433.

Washbourne P, Bennett JE, McAllister AK. 2002. Rapid recruitment of NMDA receptor transport packets to nascent synapses. *Nat Neurosci* 5(8):751-759.

Wiesel TN. 1982. Postnatal development of the visual cortex and the influence of environment. *Nature* 299(5884):583-591.

Yamada I, Rogerson P. 2003. An empirical comparison of edge effect correction methods applied to K-function analysis. *Geographical Analysis* 35(2):12.

Yoshimura Y, Yamauchi Y, Shinkawa T, Taoka M, Donai H, Takahashi N, Isobe T, Yamauchi T. 2004. Molecular constituents of the postsynaptic density fraction revealed by proteomic analysis using multidimensional liquid chromatography-tandem mass spectrometry. *J Neurochem* 88(3):759-768.

Zuo Y, Lin A, Chang P, Gan WB. 2005a. Development of long-term dendritic spine stability in diverse regions of cerebral cortex. *Neuron* 46(2):181-189.

Zuo Y, Yang G, Kwon E, Gan WB. 2005b. Long-term sensory deprivation prevents dendritic spine loss in primary somatosensory cortex. *Nature* 436(7048):261-265.

## **Vita**

Matthew Thomas Swulius was born in San Antonio, Texas on April 10, 1980, the son of Thomas Michael Swulius and Kathleen Karen Swulius. He then spent the next eighteen years of his life living all over Texas from the prairies of the panhandle to the swamps of the southeast, where he completed high school at Hamshire-Fannett High School, Hamshire, Texas in 1998. He received his Bachelor of Science degree in Neuroscience from Baylor University in Waco, Texas in 2002, and immediately began work as a research technician in the Pathology Department of the Baylor College of Medicine for the next two years. It was here that his interests began to focus on the cellular and molecular level before finally entering the Ph.D. program at The University of Texas Health Science Center at Houston Graduate School of Biomedical Sciences in 2004.

Permanent Address:  
304 Bayou Drive  
Beaumont, Texas 77705